ABSTRACT

Title of Document:	CHARACTERIZATION OF POLYPYRROLE/GOLD BILAYERS FOR MICRO-VALVE DESIGN
	STEVEN C. FANNING MECHANICAL ENGINEERING MASTER OF SCIENCE 2005
Directed By:	DR. ELISABETH SMELA MECHANICAL ENGINEERING

Polypyrrole/gold bilayers are being developed as micro-actuators for several applications. The goal of this thesis was to use these bilayers in a micro-valve to control female urinary incontinence. Several substrate materials and designs were investigated, with noteworthy findings, including the development of a bulk micromachining method for titanium based on wet etching.

Despite past research on polypyrrole/gold bilayers, the relationships between design parameters and performance were unknown. Work completed in this thesis resulted in data showing how the layer thicknesses and hinge length influence actuator bending and force. Bilayer performance was also examined as a function of temperature and in urine. Bilayer curvature increased at body temperature in a standard electrolyte, but in urine PPy failed at those temperatures.

CHARACTERIZATION OF POLYPYRROLE/GOLD BILAYERS FOR MICRO-VALVE DESIGN

By

Steven C. Fanning

Thesis submitted to the Faculty of the Graduate School of the
University of Maryland, College Park, in partial fulfillment
of the requirements for the degree of
Master of Science
2005

Advisory Committee:
Associate Professor Elisabeth Smela, Chair
Associate Professor Donald DeVoe
Assistant Professor Srinivasa R. Raghavan

Dedication

I would like to dedicate this thesis to the people in my life who supported my pursuits. This undertaking could not have been accomplished without them behind me.

First, I would like to thank my family, in particular my mom and my dad, Susan and William Fanning, and my grandparents, Inge and Gerhard Hildebrandt. Their support was instrumental in allowing me to pursue my goals. Throughout my life they have encouraged me to never stop learning and seek out new challenges.

I would also like to thank my girlfriend, Allison Ries. Her support through my research as well as the thesis writing process was wonderful. Obtaining a Masters of Science degree requires a lot of time and dedication, and her understanding and encouragement was greatly appreciated.

Acknowledgements

I would also like to acknowledge several people who were instrumental in the completion of my thesis. First and foremost I would like to thank my advisor Dr. Elisabeth Smela. Her guidance in the field of conjugated polymers and engineering in general has been crucial. I would also like to thank Michael Furst for his help in many aspects of this project including sample fabrication and building of several testing apparatus. I'd like to acknowledge Marc Christophersen for bringing a fresh view and ideas to the lab resulting in heaps of great data. Several of my colleagues need to be mentioned for helping in all sorts of project related tasks and for allowing me to look forward to coming in to the lab each day: Yingkai Liu, Xuezheng Wang, Samuel Moseley, Remi Delille, Mario Urdaneta, and Marc Dandin. Nolan Ballew and Tom Loughran need to be thanked for their immense understanding of the machinery I needed to use on a daily basis, and for being all around good guys. General modeling was made possible by help from Dr. Benjamin Shapiro. Finally I would like to thank Infinite Biomedical Technologies for their financial support as well as Gary Barrett for his help.

Table of Contents

List of Tables

List of Figures

Chapter 1 Introduction

1.1 Project Motivation: Female Urinary Incontinence

There is a need for a reliable solution to the problem of female urinary incontinence that will allow patients to live better lives. Many women who suffer from this condition find themselves spending more and more time in their houses as their conditions worsen to avoid potential public embarrassment. A non-surgical alternative to help these women would be welcome. The problem of female urinary incontinence affects an astounding number of women, with approximately 85% of the 13 million adults afflicted in the United States being women [1]. This large number of cases results in approximately $26 billion of health care costs in the US per year [2].

Despite this condition affecting so many people, the causes are still not fully understood. The majority of female urinary incontinence cases fall under two main classifications: stress incontinence and urge incontinence. There are several differences between the two conditions that set them apart from each other. Stress incontinence is exhibited during physically stressful events, such as sneezing, coughing, or jumping. Internal stresses exceed what the urethra can hold back, leading to urine leakage. Urge incontinence, on the other hand, is caused by spontaneous bladder contractions or spasms, with less obvious causes. Stress incontinence occurs more typically in older women who have

gone through a vaginal childbirth, whereas urge incontinence occurs more generally in post-menopausal women .

Incontinence has historically been treated in several different ways. There are surgical, therapeutic, and pharmaceutical treatments. Since most women suffering from this condition are older, complications arising from surgery would undoubtedly be prevalent.

1.2 Proposed Device

A non-surgical solution that would not require medication would seem to be optimal. Creating this alternative began with selecting an actuation technology, polypyrrole/gold bilayers, and devising an initial method of implementing it. These types of actuators are strips that operate by expanding and contracting the polypyrrole (PPy). This creates an overall bending of the strip. A simple method of designing a PPy/Au bilayer actuator to a specific task was needed. Nothing of this nature existed within the literature. These types of actuators were simply not well enough understood to be considered fully characterized.

Infinite Biomedical Technologies (IBT) proposed the idea of a device that could be self-inserted for patient convenience. The device would regulate urine flow through the use of an array of microvalves.

A schematic of the microvalve developed by Smela's research group is shown in Figure 1. It was assembled from two components. The first component was the actuator,

fabricated on the surface of a substrate. A plug was formed at the end of the actuating hinge by etching the plug shape through the substrate. (Detailed fabrication processes for the actuator portion are presented in Chapter 2.) The second component was a valve seat, a substrate with a flow port and sealing gasket. (The fabrication sequence for this seat can be seen in section 2.6.) The seat was attached to the back of the actuator substrate (see section 2.7.2).

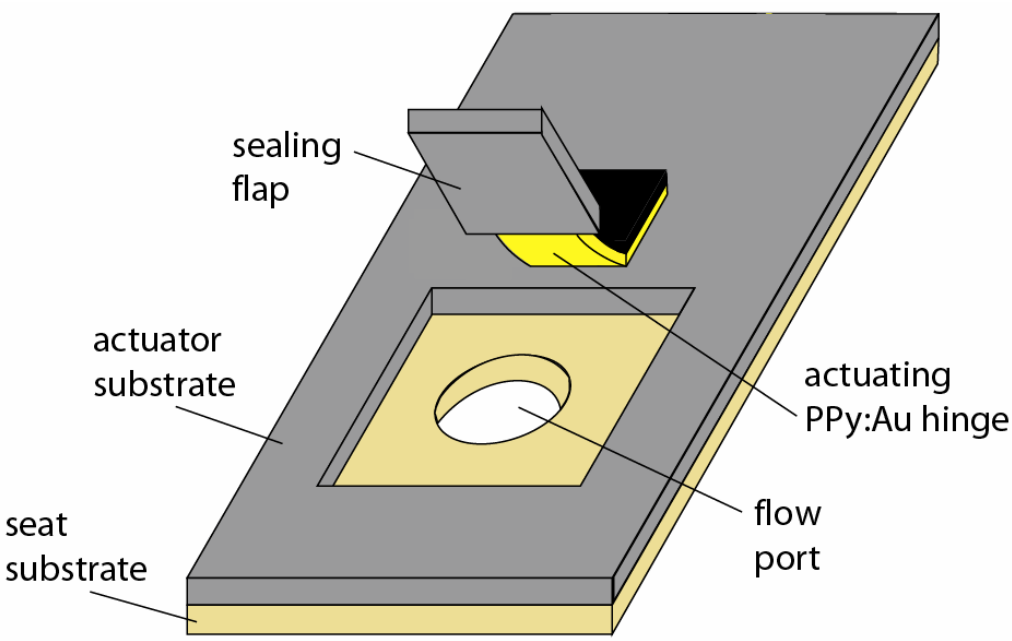

Figure 1. A schematic of an assembled microvalve consisting of an actuator substrate affixed to a seat substrate.

As a safety precaution, the device was designed to fail in the open position. When no voltage is applied, the actuator is bent away from the substrate and the valve flow hole is open. To close the device, a negative voltage is applied.

IBT planned that the device would be replaced monthly. A watch battery could readily supply the power consumed by the valve in one month assuming 10 cycles per day [3].

IBT proposed that the device would be activated using one of two methods. One concept would incorporate a pressure sensor. This method would require the patient to learn over time to apply pressure to the device using their abdominal muscles and bladder. Once the required pressure was achieved, the actuators in the incontinence control device would actuate, allowing urine flow to take place. The other concept would allow the user to activate the device externally, using a button for example.

1.3 PPy Background

PPy is a conjugated polymer. Conjugation is distinguished by alternating single and double bonds between carbon atoms along the polymer backbone. This conjugated structure results in semiconducting properties, such that the polymer readily conducts electricity in its oxidized (doped) state. The oxidized state of PPy(DBS) is very similar to doped silicon, which has charged particles within it, allowing it to conduct electricity.

In our lab, PPy is electrochemically deposited from an aqueous solution of 0.1 M pyrrole and 0.1 M NaDBS, where DBS stands for dodecylbenzene sulfonate. During growth within this NaDBS solution the polymer deposits in its oxidized form, which is also considered "doped", much like silicon can be doped. A positive voltage around +0.5 V vs. Ag/AgCl is typically used during electrochemical deposition of PPy(DBS). To maintain charge neutrality during this process, the large DBS^- anions are trapped within

the polymer chains. During cycling, after growth is completed, these DBS anions remain immobile within the polymer chains. Having these anions embedded within the polymer results in higher conductivity [4] and better mechanical properties [5,6] than PPy grown with the presence of small mobile anions, such as perchlorate. For charge balance to be maintained within the polymer during voltage application, the polymer can simply pull in or expel charged particles. If the surrounding liquid is an electrolyte solution, mass transport of cations and water takes place into and out of the polymer. This transport causes the PPy(DBS) to swell and contract in the reduced and oxidized states, respectively. In PPy(DBS) the fully oxidized state is typically at 0 V vs. Ag/AgCl or a slight positive potential. In this state the mass transport has moved cations and liquid out of the polymer, causing the polymer to shrink. The fully reduced state is typically at a negative potential of -1 V or slightly lower. In this state, cations and liquid are transported into the polymer causing the polymer to swell.

The polymer is electrochemically grown on thin gold layers to create bilayer actuators. As voltages are applied to the bilayer, the PPy expands and contracts in response to the voltages. Since the gold does not expand or contract as a result of the application of voltage, the bilayer bends. The use of a bilayer allows for larger displacements than a linear PPy actuator.

1.4 Other Microvalve Technologies

There are several types of technologies for making microvalves, but none of them met the needs of the urinary incontinence device. There are a few examples worth mentioning. First is a PDMS microvalve that requires no alignment steps. It is assembled from

several pieces of PDMS, with only one that is patterned. However, this device requires external pumps and motors to operate [7]. There are also check valves made from SU-8. Check valves allow flow in one direction and not the other, but since they do this in a purely passive manner [8] they could not be used to control urine flow. Finally, polymer gel microvalves have been demonstrated, but they actuate in response to pH changes or chemical stimuli [9], not electrical signals.

1.5 Actuation

PPy can be electrochemically oxidized (electrons removed from the polymer backbone) and reduced (electrons added back onto the backbone). In switching between the two states, ions from a surrounding electrolyte are drawn into or expelled from the polymer in order to maintain charger neutrality. Ion ingress causes the PPy to expand.

Oxidation and reduction (redox) reactions draw current. Therefore, a linear voltage sweep results in a current peak when the reaction potential is reached. Sweeps between two voltage endpoints are known as cyclic voltammograms (CV's). The redox limits used to cycle PPy in aqueous electrolytes are 0 V and -1 V vs. Ag/AgCl. Electrochemical potentials are always specified versus an equilibrium reaction, in this case silver to silver chloride, provided by a reference electrode.

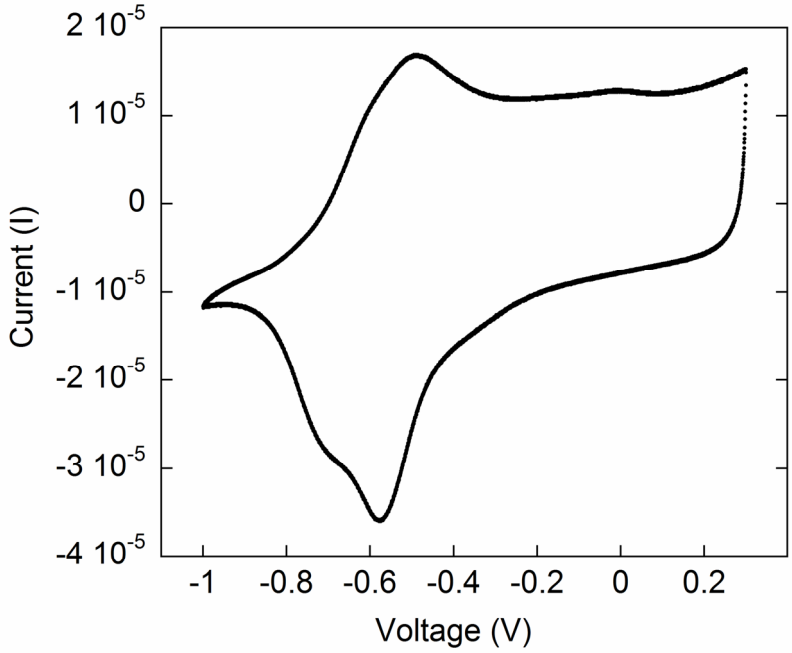

Figure 2. A normal cyclic voltammogram of PPy(DBS) run in 0.1 M NaDBS. The scan rate was 50 mV/sec.

Our group uses PPy(DBS) as the actuator material, where DBS is the dopant. The PPy is deposited in a solution containing DBS, which is a large ion that becomes trapped within the PPy chains during growth. This causes the material to exchange cations during electrochemical switching, so that it expands in the reduced state. When the PPy is grown on an electrode that does not expand or contract, such as gold, a bilayer is created that bends when the PPy swells or contracts.

1.6 Prior Work with PPy

The field investigating conjugated polymer actuators is relatively new, with literature on the subject starting in 1992. Much investigation has already been done, especially on the

conjugated polymer PPy. The polymer is far from fully characterized, however, especially when it comes to bilayer actuator performance.

1.6.1 Existing PPy Metrics

A lot of work has been conducted on PPy to gather various material properties. The Young's modulus of PPy doped with dodecylbenzenesulfonate, PPy(DBS), has been reported to be 0.45 GPa in the oxidized state and 0.20 GPa in the reduced state for films 10 μm thick [10]. The PPy in bilayer microactuators is typically only 1-2 μm thick, so properties could differ from the more 'bulk' vales of 10 μm. The Young's modulus of bulk Au is 83 GPa, but for thin gold films it has been shown to be as low as 53-55 GPa [11]. The strain in PPy(DBS) has been reported to be approximately 3% in the plane of the film.

1.6.2 Bilayers

As was mentioned, the PPy samples created for this project were typically considerably thinner than those tested in the literature. These values, however, were used as approximate values for initial design purposes. Bilayer actuator metrics, on the other hand, were unavailable in the literature. What needed to be created was an understanding of how design parameters affected the various performance capabilities of a PPy/Au actuator. The interactions between design variables and output parameters is discussed in more detail in Chapter 3.

Several groups had used PPy in bilayer actuators [12-14]. Au was used as the second layer for several reasons. First, gold is non-reactive, which is of importance both for the electrochemical reactions that take place in depositing and cycling the polymer, but also when placing devices within the human body. Bio-compatibility is not only concerned with how the device may be negatively impacted by the body, but more importantly how the device may negatively impact the body. Gold is also easy to deposit: sputtering, thermal evaporation, and e-beam may be used. The thickness can be tightly controlled using these deposition methods, which is important because the PPy to gold thickness ratio defines the actuator performance to a great degree. Gold requires an adhesion layer such as Cr or Ti to promote adhesion between the gold and most substrates. This allows a versatile fabrication method, called differential adhesion [15], to be used for sample release as a result of strategically placing Cr in some locations below the gold and not others. Since the gold requires the Cr to stick to the surface, the places with no Cr are easily peeled up during the bilayer's initial actuation.

In the literature it was also mentioned that PPy/Au bilayers could be operated within urine [16]. This was another pivotal reason for selecting this type of actuator to drive the urinary incontinence device.

1.6.3 Previous Work on Incontinence Microvalves

Previous work was conducted within Dr. Smela's group, primarily by Lance Hyo Oh, towards the goal of the urinary incontinence valve. A comprehensive summary of his work on this project can be seen in his masters thesis [3]. He reviewed the existing

actuation microtechnologies and decided that conjugated polymers were the best candidate for this purpose. An L-shaped micro-hinge device, Figure 3, was designed for characterization of the PPy/Au bilayers. The device was designed to have four arms, each with two sets of four different hinge lengths. He observed the devices edge-on to obtain the bending angles at the oxidation and reduction potentials of the PPy. Before an arm was observed for bending behavior, the previously observed arm was cut off so that it would not block visual observation.

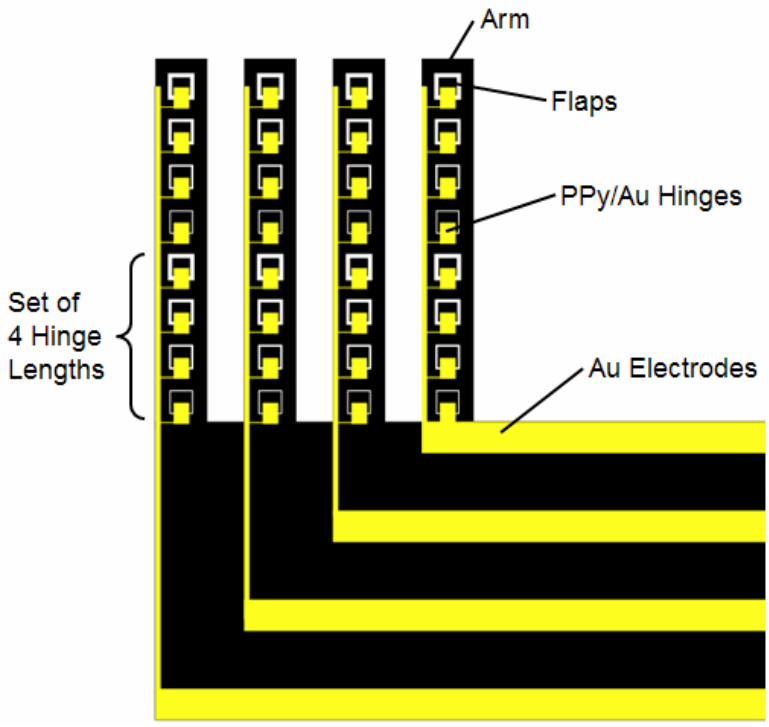

Figure 3. Original L-shaped design for bending angle studies with 32 flaps, 8 each of 4 different hinge lengths. Design created by Mr. Oh.

Work was also conducted by Mr. Oh on sample testing within a human urine control solution from Quantimetrix. These tests showed that operation indeed took place within urine. Further testing was conducted at several temperatures within the range found in

the human body. These showed that bending increased as the temperature increased. During 2005, however, we found that the human urine control has several items "spiked" in so that they can be used to detect abnormalities within urine samples. Therefore, these tests needed to be redone within a more natural urine solution.

Force testing of the L-shaped samples was also conducted by Mr. Oh. This was done by placing weights upon an individual flap and then actuating the flap. Weights were increased systematically until no more movement could be achieved by the actuator. This determined the blocked force the sample could produce.

Chapter 2 Development of Processing Methods

This chapter outlines the fabrication methods that were developed for producing valve-style samples and the results achieved with them. Three different substrate types are discussed, as well as the motivation for using them: Kapton, titanium, and silicon.

2.1 Kapton Substrate Microvalves

This project began as a continuation of previous work in which actuating flaps were fabricated from a Kapton substrate [3]. Kapton was used at the start of the project because it is transparent, so double-sided aligning could be done on the university's single-sided aligner. Changes had to be made to the fabrication process to make it more reliable. Most of these changes were refinements, as opposed to sweeping changes. The first of these modifications was to rework the masks to allow more accurate alignment. The plasma etching step was moved from an asher to a more controllable RIE system, with the recipe detailed below. The protective layers of aluminum were deposited by sputtering, as opposed to thermal evaporation, as it was found that the sputtered aluminum etched more uniformly. (Ultimately, the Kapton substrate was abandoned, as discussed later.)

2.1.1 Fabrication Sequence

1. A 50 μm thick Kapton-HN (DuPont) substrate (orange) was cleaned using acetone, methanol, and isopropanol.

2. The Kapton sheet was placed in a sputtering machine (AJA Intl. model ATC 1800) and run through a five-minute plasma clean to remove remaining surface contaminants. A layer of Cr was sputtered onto the top-side (pressure of $5x10^{-3}$ Torr, power of 200 W, deposition rate of 100 Å/min) as an adhesion layer for the gold to follow. A layer of Au (yellow) was sputtered onto the top-side (pressure of $5x10^{-3}$ Torr, power of 200 W, deposition rate of 500 Å/min). Thermal evaporation or e-beam evaporation could be used as an alternative to deposit the Au. The thickness of this gold layer would be determined by application requirements using the curvature data set forth in section 3.1.3 as well as the force data set forth in section 3.5.2

3. The gold layer was patterned using standard photolithography. This was done by spin-coating the Au surface with a layer of Shipley 1813 photoresist at 3000 rpm for 30 seconds on a spinner (Headway Research model # EC-102) and soft-baking for 2

minutes on a hot plate at 90 °C. The photoresist was exposed beneath a transparency mask (3000 dpi from a commercial printer such as RGM Graphics, Bethesda) for 13 seconds in a mask aligner (Karl Suss MJB3) to UV light of 405 nm with and a power density of 12 mW/cm^2. The resist was developed in undiluted CD-30 (Shipley) for 30 seconds to remove the exposed photoresist. The sample was placed in a commercial gold etch (Transene, TFA), which has an etch rate of approximately 28 Å/sec., to pattern the gold not covered by the photoresist. This was followed by a chromium etchant (Transene, 1020) which has an etch rate of approximately 40 Å/sec.

The sample needed to be rigorously cleaned at this point. Without this cleaning step, PPy growth occurred over the entire surface. We suspect that the chromium etchant left some residue on the Kapton surface that conducted electricity. Piranha etch cleaned these surfaces sufficiently. The piranha recipe was a 5:1:1 H_20:H_2SO_4:H_2O_2 for 5 minutes, which removes organic material. It should be noted that piranha etch also removes aluminum.

4. A layer of photoresist was spun on the top side and patterned to cover the electrical connection points. This prevents PPy growth in unwanted areas. When different spots need to have PPy grown on them, the photoresist on the needed electrical

connection was scraped off with tweezers.

PPy (black) was deposited electrochemically from a solution of 0.1 M pyrrole (Aldrich) and 0.1 M NaDBS (Aldrich) on the exposed gold on the front side. This was achieved by placing the sample in the solution and connecting it to the working electrode lead of a potentiostat (EcoChemie pgstat30). A three electrode configuration was used that included a counter electrode (typically a gold coated substrate that was larger than the sample or a piece of graphite) and an Ag/AgCl reference electrode (Bioanalytical Systems). The reference electrode was typically 1 cm from the working electrode, and the counter electrode was 5 cm from the working electrode and parallel to it. A voltage of approximately 0.49 V vs. Ag/AgCl was applied using the potentiostat until the desired thickness was obtained.

5. A layer of Al (gray) was sputtered onto the sample's bottom surface (pressure of $5x10^{-3}$ Torr, power of 200 W, deposition rate of 70 μm/min). The thickness of this aluminum layer must be at least 2000 Å to 3000 Å to provide an adequate RIE protection layer.

6. A layer of photoresist was applied to the back side and patterned to define where the Kapton will be patterned in a later step. A layer of photoresist was spun on the top-side of the sample to protect the PPy during the aluminum etch happening next.

7. The aluminum layer was patterned next. The sample was chemically wet etched using a commercial Al etchant (Transene, Type A), which had an etch rate of approximately 10 Å/sec.

   All the remaining photoresist is then exposed on both sides and removed using developer. Note that aluminum is removed immediately in photoresist stripper.

8. The sample was placed in a sputtering machine (AJA Intl. model ATC 1800) and NOT run through a plasma clean, as this would remove the PPy. A 2000 Å to 3000 Å layer of Al (gray) was sputtered onto the sample top side surface.

9. The sample was placed in an RIE (reactive ion etching) machine (Trion), bottom side up. The etch conditions within the system were a flow rate of 75 sccm O_2, a pressure of 250 mTorr and a RF power level of 250 W. The etch was conducted for approximately 1 hour and 15 minutes, as the etch rate for Kapton was similar to most polymers in an oxygen plasma. The samples should be set up with glass slides to hold down the edges of the sample and not allow the plasma beneath. (Initially a glass slide was placed beneath the entire sample as well, however this led to insufficient cooling of the sample and actuator damage.)

10. The aluminum layers were removed using a commercial aluminum etch (Transene, Type A). Removal typically took place in a few minutes. However, occasionally the aluminum on the side exposed to the plasma exhibited abnormal behavior and

required additional time within the aluminum etchant, up to 40 minutes. The typical etch rate was approximately 10 Å/sec.

2.1.2 Results

Once the Kapton substrate fabrication sequence was finalized, samples were fabricated for testing. Bending angle tests were performed to determine the relationships between bending and the geometrical parameters of PPy/Au bilayers. Samples were made based on an initial model that predicted that a 4:1 (PPy/Au) thickness ratio would produce maximal bending. Four microns was typical a PPy thickness, so one micron of gold was chosen to create these bilayers.

The Kapton substrate samples were designed such that in the oxidized position (0 V) the flap would be bent and "open", and in the reduced position (-1 V) the flap would be straight and closed. Once these devices were incorporated into a working valve, closed would be defined as flush with the substrate and open as having the flap bent away from the hole. Having the 0 V position bending away from the flow hole and allowing flow to pass through was designed as a fail-safe for the valves: if the power source were to fail, the valve would fail open. This would prevent dangerous conditions from occurring with a permanently sealed valve trapping urine within the body. The position of the oxidized and reduced states can be seen in Figure 4.

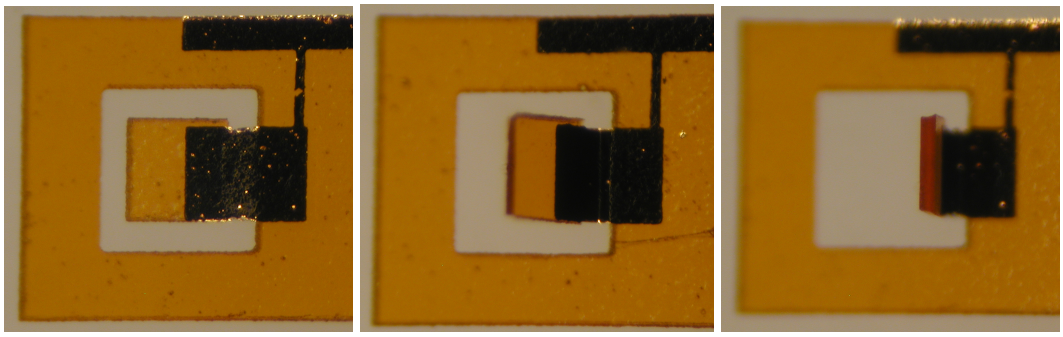

Figure 4. Photos showing an actuating Kapton substrate flap. The left shows the reduced position, the middle an intermediate position, and the right the oxidized position. The flap is approximately 400 µm x 400 µm square.

A bilayer of a given thickness ratio and total thickness has a particular radius of curvature. Therefore, by increasing the hinge length, the bending angle can be increased. This effect is illustrated in Figure 5. Notice that the radius of curvature remains the same in both cases. If bending angle were plotted against hinge length, one would expect a linear relationship.

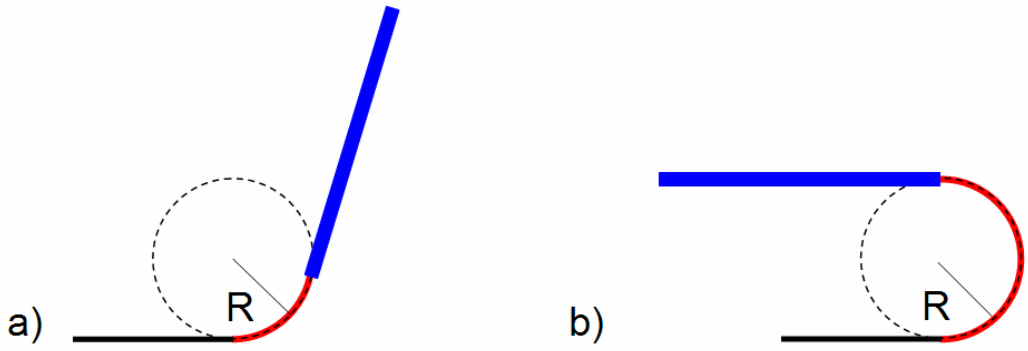

Figure 5. When bilayers with identical layer thicknesses have differing hinge lengths, the overall bending angle differs. (a) A short hinge and b (b) a longer hinge that produces a greater bending angle. Notice the radius of curvature remains the same, as that is determined by the layer thicknesses.

Once the Kapton substrate samples were fabricated, bending testing commenced. Actual hinge length was measured for every hinge by viewing the sample from the back side with a microscope. A microscope with a reticle was used, giving distances in microns. At known magnifications, the distances between the ticks were known. One set of data, gathered from four different locations on the same sample, is shown in Figure 6. Each color corresponds to one of the four arms, with each arm designed to have four hinge lengths. Bending angle data were only taken from samples with fairly crisp hinge edges and visually undamaged PPy that did not exhibit the drift effect described below. The first thing to notice is that the actual hinge lengths, measured after fabrication under a microscope, varied considerably from hinge to hinge. The second is that there was no clear relationship between bending angle and hinge length. Even from bilayers on the same sample, the data were highly scattered. Unfortunately, the bending angles were too inconsistent to determine any kind of relationship.

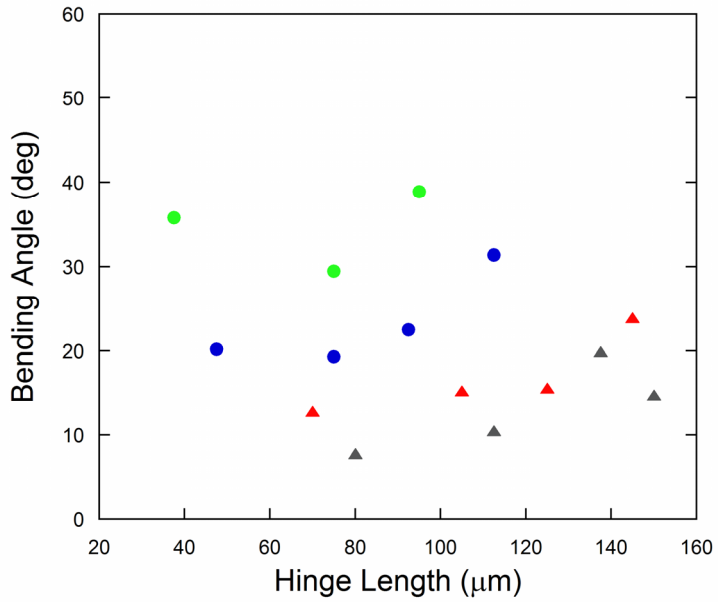

Figure 6. Graph showing the bending angle vs. hinge length for a Kapton substrate sample. Each color corresponds to one of the four rows. Each data point represents an individual flap. Hinge lengths were measured after fabrication. This sample had a thickness ratio of 4.8:1 (47,480 Å PPy:9,900 Å Au). A 200 Å layer of Cr remained beneath the Au, which initially acted as an adhesion promoter between the Kapton and the Au. There was also a 1,000 Å electroplated Au layer for adhesion promotion deposited on top of the flat e-beamed Au.

A drift effect was encountered in some samples after several tens of cycles. The positions of the bilayers in the oxidized and reduced states changed by tens of degrees from their initial positions, with the hinges bending less over time. This would ultimately culminate in the bilayer bending just barely enough to be witnessed using the microscope. An example of this drift can be seen in Figure 7, which shows a set of flaps in the reduced state at the start of cycling and after 200 cycles.

The drift was most likely caused by inconsistent adhesion between the Au and PPy. This inconstancy would result in different delamination rates from sample to sample.

Experiments were being conducted at the same time by Yingkai Liu in order to determine how to achieve good adhesion under extended cycling.

a)

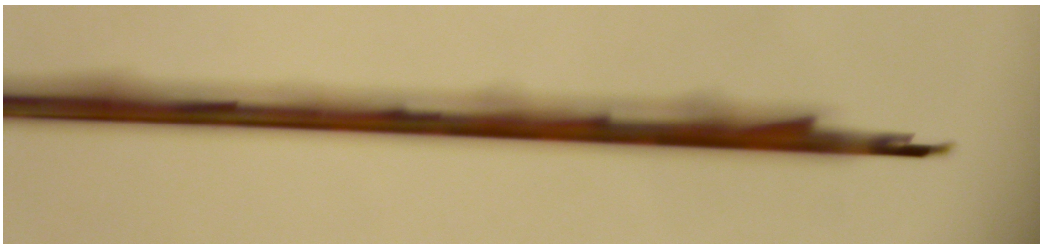

b)

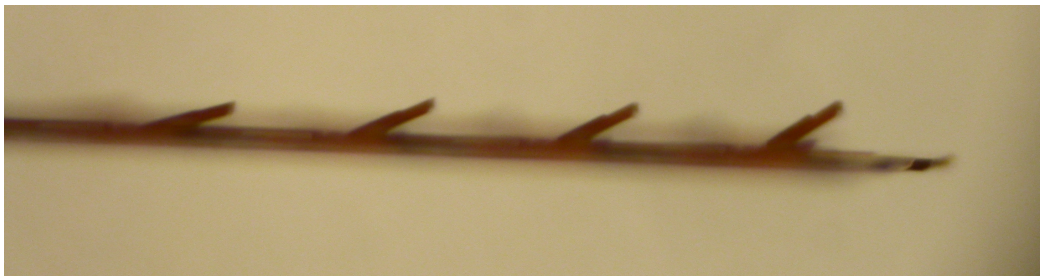

Figure 7. Photos showing a Kapton substrate sample in the a) initial reduced state and b) reduced state following 200 cycles. These types of photos were used to determine bending angle. This photo set was taken of bilayers cycled in 0.1 M NaDBS.

2.1.3 Need for Transition from Kapton

These types of devices proved problematic for several reasons. Firstly, the PPy was often damaged as a result of heat generated during the RIE process. This resulted in low device yields.

Secondly, the protective aluminum layer was also damaged in the RIE system. A physical change took place which darkened the aluminum exposed to the plasma. When the sample was placed in aluminum etchant, the side exposed to the plasma took up to 40 minutes to be removed. The side not exposed to the plasma, however, etched normally in

only a few minutes. Occasionally the PPy would not actuate, most likely because damaged aluminum remained on the PPy surface after etching.

The final, and most conclusive, reason for abandoning Kapton as the substrate for the eventual microvalve design was as a result of the manufacturer's policy. DuPont does not allow their products to be used by third parties for applications within the human body.

2.2 Ti Substrate Microvalves

The search for a new substrate material began with several requirements. The material needed to function within urine and be biocompatible so as not to adversely affect the body. The substrate also needed to be processable on a micro-scale. A final requirement was that it needed to be non-proprietary to avoid any further manufacturer issues with use in the body. A titanium sheet substrate met these criteria. Sheets 50 μm thick and 100 mm x 100 mm in area were purchased from Goodfellow Corporation and cut into four 50 X 50 mm squares with scissors.

2.2.1 Bulk Titanium Substrate Etch

The first challenge was to determine a way to reliably pattern the bulk titanium substrate. Etching needed to be compatible with the other MEMS processing steps. The literature contained etch methods for thin films of titanium [17,18]. Bulk isotropic etching had been shown for a titanium alloy [19], as had surface patterning of bulk titanium using

electrochemistry [20]. A dry anisotropic method had also been investigated [21], but equipment required to conduct that etch was unavailable at UMD.

Moving from thin film wet etching to bulk etching was difficult due to the HF in the etchant. The masking material that had been used was predominantly photoresist, which stands up to HF for only limited amounts of time. Since no published work described a method for wet etching a bulk Ti substrate, methodical experiments were conducted to find one. Table 1 details the evolution of the titanium substrate etching.

Table 1. The evolution of the titanium substrate etching recipes.

Solution	Reason for use	Resist	Etch Rate	Result
49.2% HF (straight from bottle)	HF known to etch Ti	1813 (SB)	25 μm/min	complete disintegration
5:1 (H_2O:HF)	slow etch rate	1813 (SB)	7 μm/min	470 μm lateral etch
5:1 (H_2O:HF)	keep resist intact longer	1813 (HB)	7 μm/min	260 μm lateral etch (Figure 8a)
10:1 (H_2O:HF)	slow etch rate & decrease lateral etch	1813 (SB)	4.5 μm/min	200 μm lateral etch
30:1 (H_2O:HF)	slow etch rate & decrease lateral etch	1813 (SB)	1.5 μm/min	110 μm lateral etch
30:1:1 (H_2O:HF:H_2O_2)	Ti thin film recipe uses H_2O_2 [17]	1813 (SB)	.66 μm/min	120 μm lateral etch
15:1:1 (H_2O:HF:H_2O_2)	decrease lateral etch rate	1813 (SB)	2.5 μm/min	90 μm lateral etch
15:1:1 (H_2O:HF:H_2O_2)	keep resist intact longer	SPR220-7	2 μm/min	-75 μm lateral etch -all Ti thinned
BOE	less PPy ‘‘dehydration’’	SPR220-7	-	resist peels up
15:1 (BOE:HF)	combat peel up	SPR220-7	-	resist peels up @ 10 min
15:1:1.5 (BOE:HF:H_2O_2)	combat peel-up	SPR220-7	-	resist peels up @ 7 min
15:1:0.5:0.7 (H2O:BOE:HF:H_2O_2)	combat peel-up & keep resist in tact longer	SPR220-7	2.3 μm/min	-resist still present -remove bubbles for cleanest etch -Figure 8b

SB = soft bake @ 90 °C for 2 min HB = hard bake @ 110 °C for 30 min BOE = 7:1 buffered oxide etch
H_2O_2 = 30% hydrogen peroxide HF = 49.2% hydrofluoric acid

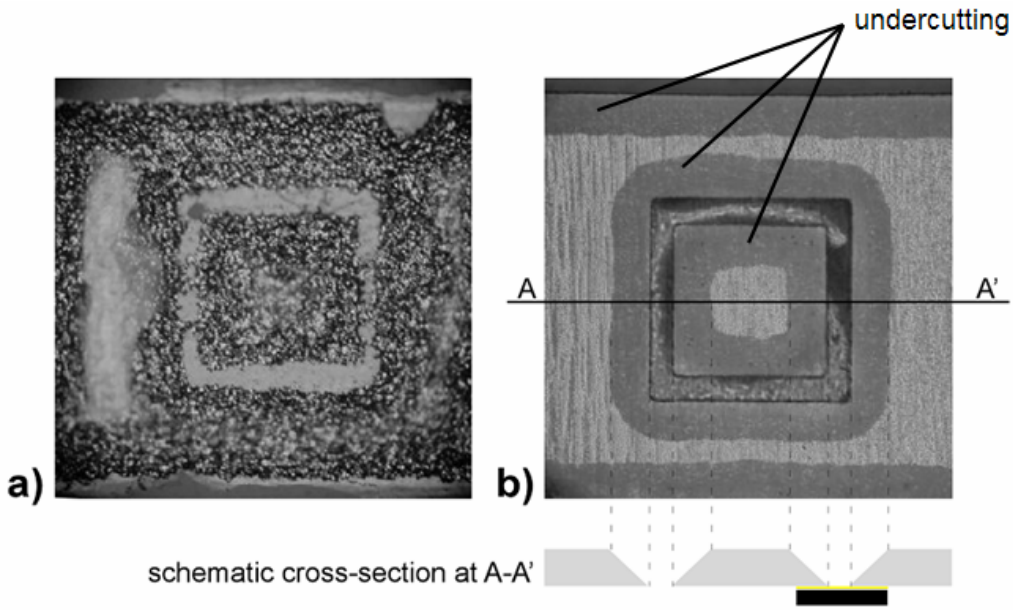

Figure 8. Back side of sample following flap release etch. a) Result of etching a flap in 5:1 water:HF. b) Result of etching in 15:1:0.5:0.7 H_2O:BOE:HF:H_2O_2 and using thick photoresist S220-7. A schematic of the cross section is shown for reference. The substantially isotropic etch resulted in sloping side-walls and undercutting.

The final etch, involving buffered oxide etch, hydrofluoric acid, hydrogen peroxide, and water, proved to be the best bulk etch. This recipe produced the smoothest sidewalls as well as maintaining the protective resist mask through etching.

2.2.2 Double-sided alignment

Titanium, unlike Kapton, is not transparent. This was important when the pattern for substrate etching needed to be aligned on the back side with respect to features on the front side. With the transparent Kapton, alignment marks on the front side were aligned while looking through the back side with a standard single-side aligner.

For the non-transparent titanium sheets, a double-sided aligner needed to be used (EVG 620), which was acquired by the university during the course of this thesis. This machine allows for alignment marks on one side of a sample to be aligned to a mask on the opposite side.

The titanium substrate was a 50 mm x 50 mm square. The only substrates the double sided aligner was designed to accept, however, were full 4" and 6" round silicon wafers. These wafers are held in place by a series of vacuum channels on the chuck beneath the wafer. All of these channels need to be covered for the machine to produce a vacuum seal, needed to lock the sample into place for alignment. A photograph of the vacuum chuck can be seen in Figure 9a.

To allow for the titanium sheets to be used in the double sided aligner, an adapter needed to be designed. The adapter needed to transfer the vacuum for holding the substrate to the top of the adapter. This was accomplished by etching a standard 4" silicon wafer in two steps. A schematic of the adapter can be seen in Figure 9b. The first step was etching half way through the thickness of the wafer using a DRIE (deep reactive ion etching) system (STS). This first etch established the two windows required by the alignment system for the back side cameras to look through for alignment mark location. It also produced a channel allowing vacuum transfer to the front of the adapter. A second etch was conducted on the opposite side to make a series of vacuum channels connected to the through-channel. This second etch also fully opened up the windows and vacuum transfer channel etched partially on the first side.

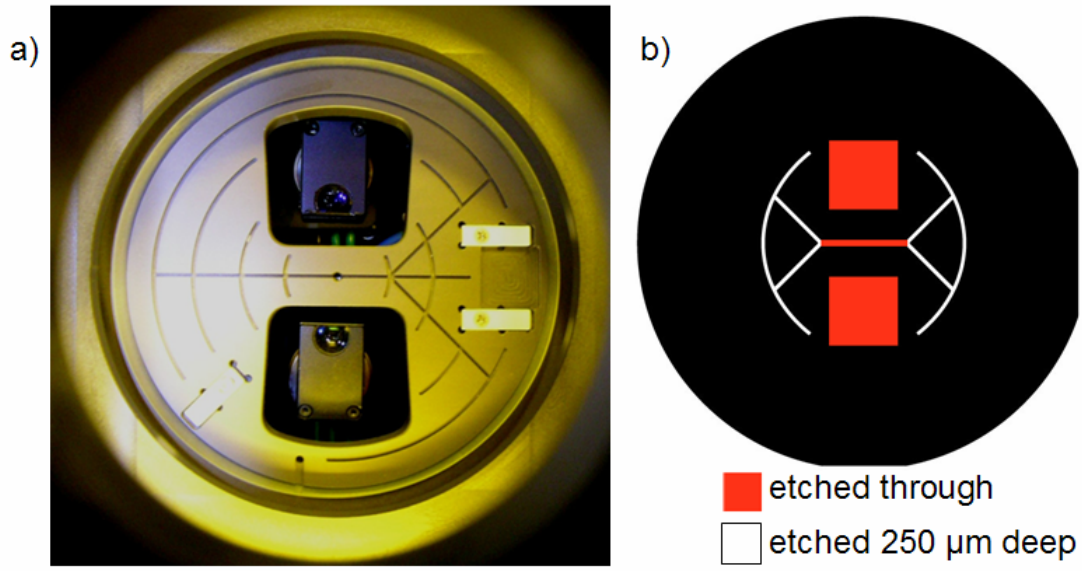

Figure 9. a) Overview of the double sided aligner chuck. b) Schematic of the sample adapter.

The adapter was successful in allowing the titanium samples to be used in the double sided aligner. The vacuum sensor within the double-sided aligner detected no leakage.

2.2.3 Fabrication Sequence

The process sequence for fabricating micro-valves on a Ti substrate follows. Masks were basically the same as the Kapton substrate masks. However, the electrical conductivity of the titanium substrate did not allow for growing of multiple PPy thicknesses on one sample by breaking Au contacts.

1. A titanium substrate (gray) was cleaned using a standard household oil-removing surfactant (Dial) followed by cleaning in acetone, methanol, and isopropanol.

2. The titanium sheet was sputtered with a layer of Au as described in the Kapton substrate process sequence. The thickness of the gold layer was determined by application requirements using the curvature data set forth in Section 3.1.3 as well as the force data in Section 3.5.2. (Thermal evaporation or e-beam evaporation could be used as alternatives to deposit the Au.) No adhesion layer was required.

3. The gold layer was patterned using standard photolithography as described in the Kapton substrate process sequence.

4. A layer of S220-7 resist (Shipley) was spun on the top (Au) side at 3500 rpm for 30 seconds. The sample was baked at 90 °C for 100 seconds and then at 110 °C for 100 seconds. Hexamethyldisilazane (HMDS, MicroSi, Inc.) was spin-coated on the bottom side at 3500 rpm for 30 seconds to improve adhesion between the Ti and the

resist. S220-7 PR was also applied to the bottom side by spin-coating and put through the same processing steps. The S220-7 was left to sit a minimum of for 2 hours before patterning, which then produced finer detail following the develop step .

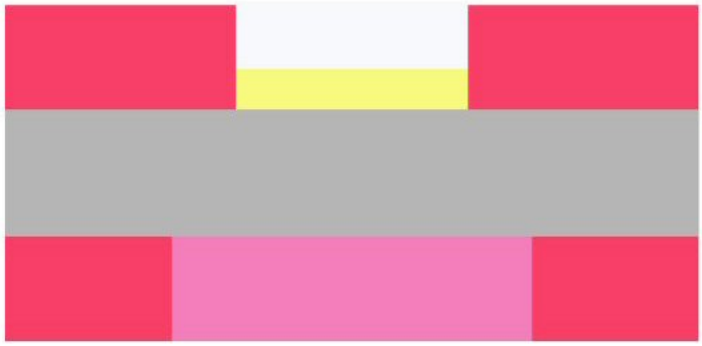

5. The top-side resist was exposed for 45 seconds to 12 mW/cm^2 405 nm light and developed in CD-30 for 4 minutes. This opened a well for PPy deposition later. The bottom side was exposed (shown as pink) using the double sided aligner (EVG model 620) to align the features on the bottom with the pattern on the top. The double sided aligner has a power density of 47.8 mW/cm^2, and the exposure time was 13 seconds.

6. PPy (black) was deposited electrochemically as described in the Kapton substrate process sequence.

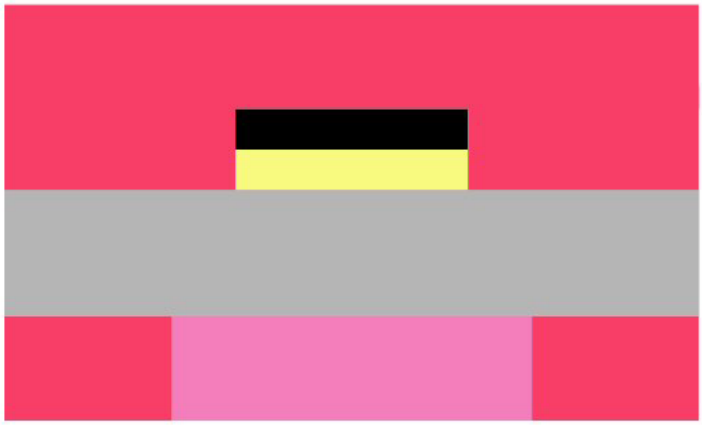

7. A protective layer of S220-7 was applied over the whole top side by spin coating and baked as described above.

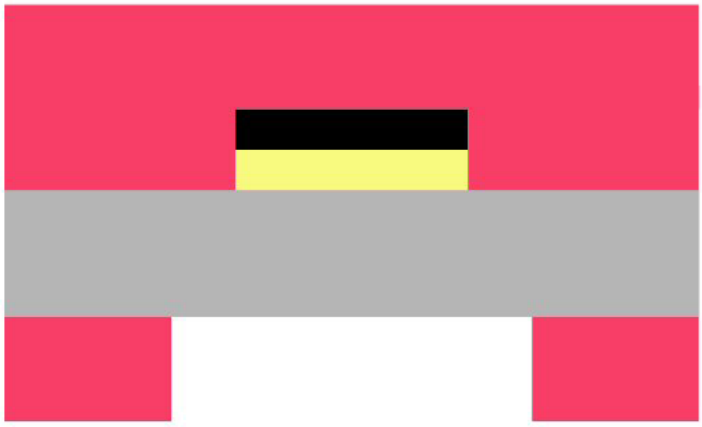

8. The sample was placed in undiluted CD-30 developer for approximately 2 minutes to develop the previously exposed back side.

9. The sample was etched in a 15:1:0.5:0.7 (H2O:BOE:HF:H_2O_2) solution for approximately 20 minutes. During this etch a plastic pipette was used to gently remove bubbles which formed at the resist/titanium interfaces. These bubbles tend to accelerate peel-up of resist. This etch recipe etched the exposed titanium while maintaining relatively straight edges. The resist was undercut to some extent, even in this recipe. The lateral etch rate was faster than the through-substrate etch rate.

2.2.4 Results

Once the fabrication sequence was finalized, several sets of samples were successfully produced (Figure 10). These samples used the same basic layout as the original Kapton samples shown in Figure 3. A thickness of 3000 Å was chosen as the Au thickness for testing based on successful bending witnessed in the lab previously by Mr. Oh.

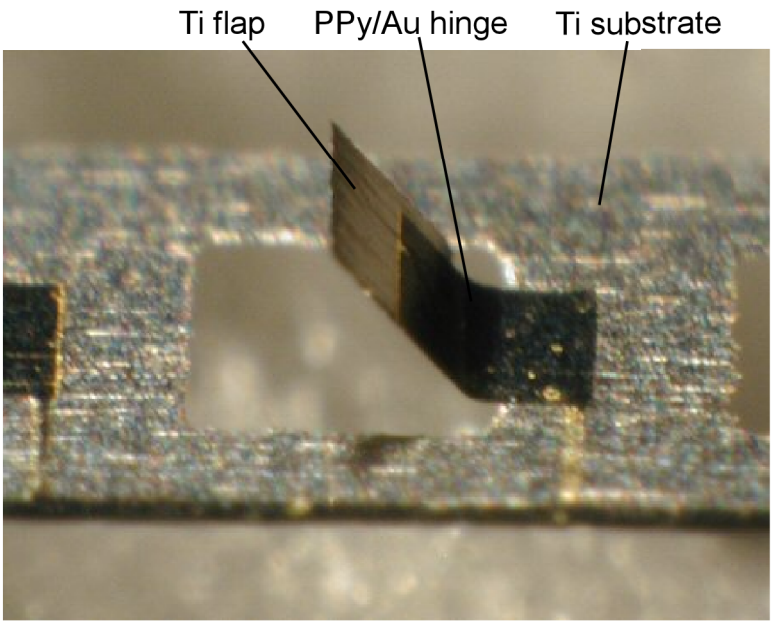

Figure 10. Completed Ti flap rotated approximately 60° from the substrate by a PPy/Au hinge.

The samples had four different hinge lengths for measurement: 20 μm, 40 μm, 60 μm, and 80 μm. Each of these hinges were 300 μm wide.

The edges of the etched titanium, from which the hinge length was defined, were cleaned up dramatically from initial etching methods. Despite this, the extreme thickness of the substrate made crisp, straight hinge borders quite difficult to achieve. Therefore, each hinge length needed to be measured individually following fabrication. An example of the rough edges that needed to be evaluated to determine the hinge lengths can be seen in Figure 11. Substrate portions jutting out on either side of the back of the hinge needed to be taken into consideration to determine what portion of the bilayer would bend unhindered.

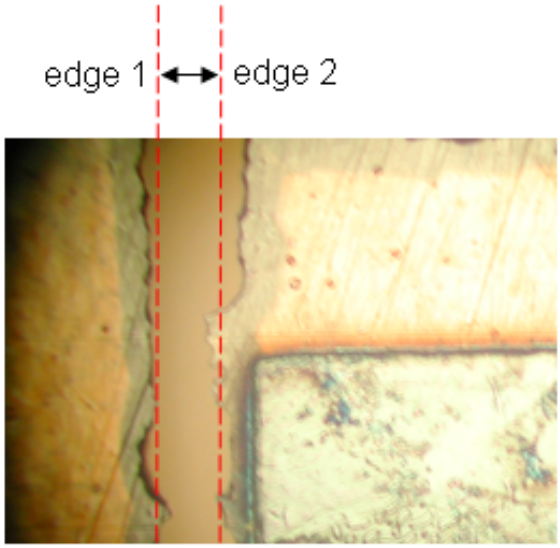

Figure 11. Example of typical hinge edges. Hinge length was measured from edge 1 to edge 2. Since the edges were not crisp, hinge lengths were only approximated by counting large jutting features as the hinge end.

During these hinge length measurements, samples were also evaluated for use in data collection. Two things in particular that would preclude a sample from use during tests were incomplete removal of the titanium substrate behind the bilayer and damage to the PPy. Both of these problems are illustrated in Figure 12.

a) 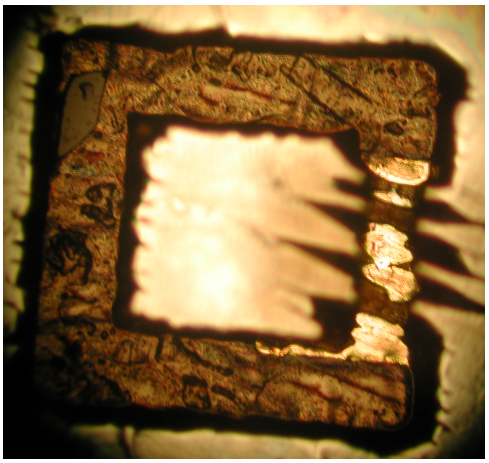 b) 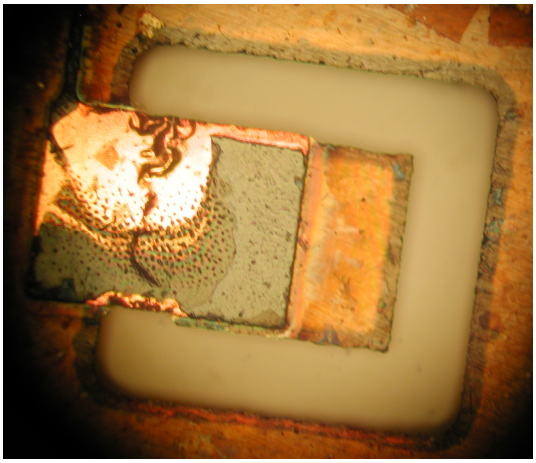

Figure 12. (a) Incomplete removal of titanium behind the bilayer as well as (b) PPy damage were reasons actuators were not used in bending tests.

The first battery of tests was to determine the amount of bending relative to the hinge length and layer thicknesses. Each sample was cycled 0.1 M NaDBS. Like the Kapton samples, the Ti samples produced an unacceptable amount of scatter (Figure 13). This was not due to the controlled parameters since all geometric possibilities were covered by having a knowledge of the PPy thickness, Au thicknesses, and the hinge length. This meant that there was another parameter producing an adverse effect on the samples, which must have been a result of a processing step. The PPy on the titanium substrate samples were exposed to several conditions not present during Kapton fabrication.

The titanium substrate samples underwent significantly less bending than the Kapton samples. Later characterization, Figure 30, showed that the geometry of these samples may have been a cause of the lessened bending. Every sample was to have 8 identical hinge lengths of each of the four designed into the masks. However, due to etching

variations, many hinge lengths were present, as can be seen in the 3000 Å Au thickness sample shown in Figure 13.

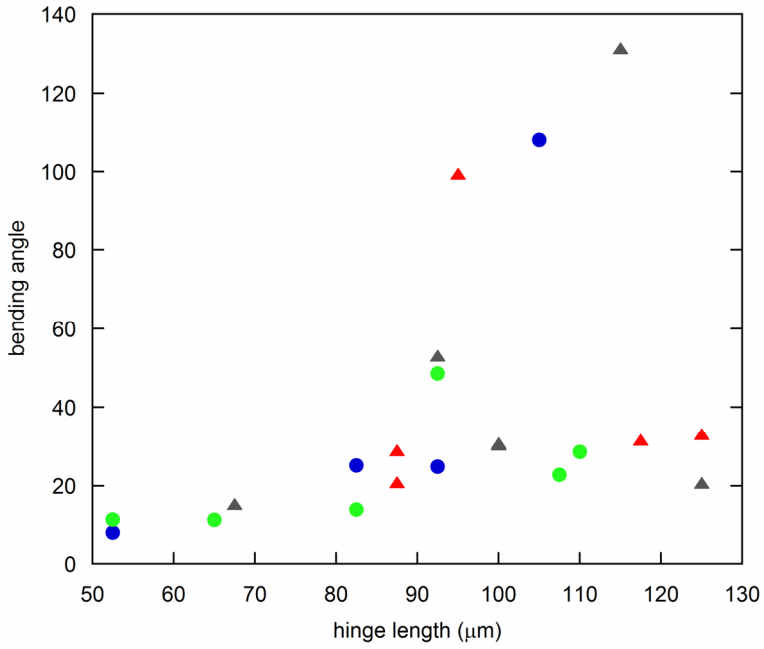

Figure 13. Graph showing the scatter produced by titanium substrate samples. Each color corresponds to one of four rows. Hinge lengths were measured individually after fabrication. This sample had a thickness ratio of 6:1 (16860 Å PPy:2800 Å Au). There was also a 1200 Å electroplated Au layer for adhesion promotion deposited on top of the flat sputtered Au.

A curvature value was calculated from the data in Figure 13 after reproducible data were obtained from surface micromachined PPy/Au bilayers fabricated by Marc Christophersen (discussed in section 3.3). A graph showing the trend line of the data in Figure 13 with some of the outlying data points removed can be seen in Figure 14. This was done to see if a representative slope of the points would produce a curvature value close to what was found in the later samples. The curvature for the titanium substrate samples was 0.0043 μm^{-1}, which was approximately seven times smaller than the 0.03

μm^{-1} value of Marc's surface machined actuators. This strongly supports the notion of an adverse effect on the PPy during the titanium substrate fabrication.

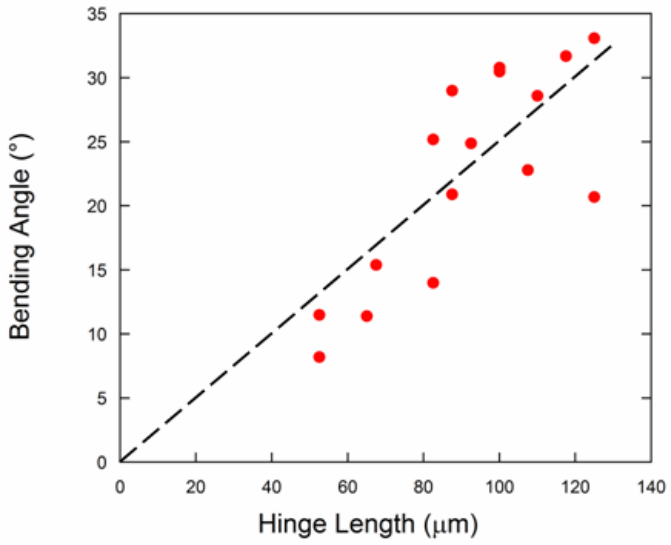

Figure 14. Graph showing the trend line of the data displayed in Figure 13 with outlying points removed. The curvature was 0.0043 μm^{-1}, which was approximately seven times smaller than the curvature of surface machined PPy/Au bilayers.

A more reliable fabrication method needed to be developed to create reproducible actuation and to understand the relationships between bending and the bilayer's geometrical parameters. If Ti is used in the future, work should be carried out to isolate the step or steps responsible for the hinge damage. A small change in the fabrication sequence may result in useful titanium substrate PPy/Au actuators.

Since Ti is biocompatible, inexpensive, and readily available, and knowing that MEMS devices using titanium substrates could not be found on the market or in the literature, a provisional patent was filed by the OTC based on what we believe is possible with this technology. This recipe for etching titanium substrates in a consistent manner should

prove generally useful for other applications. The titanium substrate may not work for this application, however, due to detrimental effects of the process sequence on the PPy.

2.3 Si Substrate Microvalves

DRIE (deep reactive ion etching) is a well-controlled, anisotropic etch method for silicon substrates. This was expected to result in greater uniformity of hinge lengths than was possible in Ti. The fabrication process used to create samples from silicon substrates was based on one in the literature [22]. One change that was made to the original process sequence was that DRIE was used in place of RIE (reactive ion etching) to etch through the silicon.

It was theorized by Dr. Smela, Mike Furst, and myself that some of the strange behavior exhibited by previous samples was due to "ears" at sample edges that arise when PPy is grown within a resist well. The sides of the PPy grow up along the edges of the well and form spikes that are much higher than the average PPy height. A schematic of this effect can be seen in Figure 15. To prevent thickness non-uniformities, PPy can be deposited over the entire surface and patterned by RIE [22].

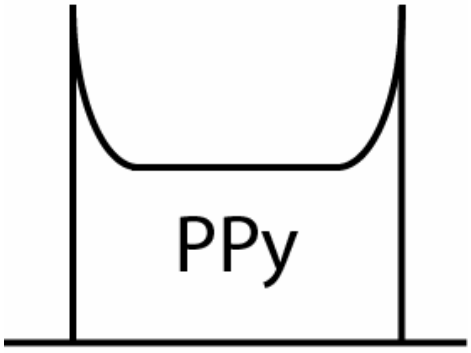

Figure 15. Schematic drawing of the "ears "produced by growing PPy within photoresist wells. These thickness variations are undesirable.

2.3.1 Fabrication Sequence

1. First, a Si wafer with oxide on both sides was used. Etching all the way through the wafer was difficult, so the thicker the oxide layer (dark brown) and thinner the Si substrate (light brown) the better. The selectivity between the oxide/photoresist and the silicon itself wasn't high enough to allow etching through an entire 500 μm wafer with a layer of typical photoresist and 1 μm of oxide.

2. Alignment marks needed to be established on the top side for later alignment of both the top and bottom sides. An 1813 photoresist layer was deposited and patterned as in the Kapton substrate section.

   The oxide on the top was etched in an RIE machine (Trion). The etch conditions

were a flow rate of 20 sccm CF_4, a pressure of 50 mTorr, and an RF power of 100 W. The etch was conducted at 0.1 μm/min in this recipe. The samples should be surrounded by additional oxide-coated Si pieces to keep the etch as uniform as possible.

3. The bottom side was patterned into a mask for plasma etching the silicon, with the oxide and a thick photoresist acting as the masking materials. A layer of S220-7 resist was applied, exposed and developed as in the titanium recipe.

   The sample was placed in an RIE machine to etch the bottom side oxide layer as in step 2. The protective SPR220-7 layer remained as a mask on the unexposed areas.

4. The Si was etched from the back side using a high rate etch in a DRIE system (STS). The etching process alternated between a duty cycle of 10 seconds of etch with 130 sccm of SF_6 and 13 sccm of O2 followed by a passivation time of 6.5 seconds with 85 sccm of C_4F_8. This recipe etched at approximately 5 μm/min. This etching step defined the Si flaps that moved by the bilayer actuators. Some silicon was left behind

the thin top-side oxide layer as a mechanical stiffening layer, so the samples were robust enough to survive until the final release in step 10.

5. A layer of chromium and gold was deposited as in the Kapton fabrication sequence. The thickness of this gold layer would be determined by application requirements using the curvature data set forth in section Section 3.1.3 as well as the force data set forth in Section 3.5.2.

6. PPy (black) was deposited electrochemically as in the Kapton fabrication sequence, but over the entire top side surface in this case.

7. PPy patterning in this method was different from the other process sequences in that the PPy was grown everywhere and then removed from the places it was not desired by the RIE. Previously, the PPy was grown within photoresist wells. The RIE removal method has been found to leave crisper edges and no 'ear' effect [22]. The PPy layer patterning began with standard photolithography, with a slightly thicker than usual protoresist. This was done by spin-coating the surface with a layer of Shipley 1818 photoresist (red) at 4000 rpm for 30 seconds on a spinner (Headway Research model # EC-102) and soft-baking for 60 seconds on a hot plate at 90 °C. The photoresist was exposed beneath a transparency mask (3000 dpi from a commercial printer such as RGM Graphics, Bethesda) for 14 seconds in a mask aligner (Karl Suss MJB3) to UV light of 365 nm with and a power density of 8 mW/cm^2. The resist was developed in undiluted CD-30 (Shipley) for 30 seconds to remove the exposed photoresist.

8. The uncovered PPy was removed using an oxygen plasma. The sample was placed in a RIE machine. The etch conditions within the system were a flow rate of 50 sccm O_2, a pressure of 250 mTorr, and an RF power level of 100 W. The etch was conducted at 0.5 μm/min for PPy in this recipe. The samples should be set up surrounded by Si pieces (preferably Si covered with PPy) to keep the etch as uniform as possible.

9. The gold layer was patterned using the existing resist as a mask. The sample was placed in a commercial gold etch and etched as in the Kapton process sequence.

10. This step involved a two part etch to release the flaps. The first step was needed to remove what silicon was left to support the flaps behind the thin oxide layer. This

was accomplished by RIE. (The etch conditions within the system were a flow rate of 50 sccm SF_6, a pressure of 300 mTorr, and an RF power of 100 W. The etch was conducted at an etch rate of 0.5 μm/min for silicon in this recipe.)

The second step was an etch to remove the SiO_2. This etch type was conducted as before.

11. The final step was to remove the photoresist. This was done by immersing the sample in 200 proof ethanol (AAper Alcohol & Chem. Co.). A five minute immersion was sufficient to remove all photoresist. It should be noted that the flaps noticeably bent out of the plane of the substrate at this point.

2.3.2 Results

As with the titanium and Kapton substrate samples, bending was measured. The samples were subjected to the same testing methodology as in section 2.2.4.

The fabrication of these silicon samples differed from the titanium samples in that the bulk of the substrate etching was done anisotropically, by the DRIE. There was a final step however, in which the release of the flaps was carried out in an RIE system.

Therefore, the final etching was isotropic. The result was that hinge lengths differed from those designed into the masks.

For the silicon samples, the gap in front of the flap portion had to be enlarged. The silicon substrate was ten times thicker than the original Kapton and titanium substrates. The flap hung down so much farther than in the previous cases that it would also swing out far enough to hit the substrate on the opposite side of the gap. An example schematic showing the reason for this redesign can be seen in Figure 16.

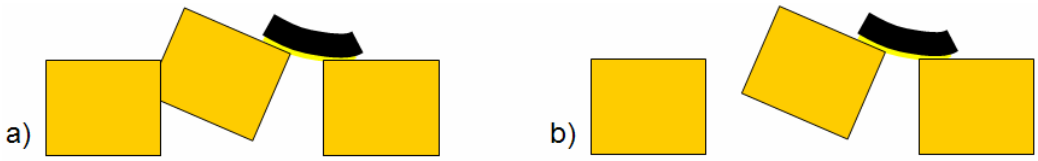

Figure 16. Schematic of the redesign that needed to take place in order for the flap made from the thicker silicon substrate to be able to swing up without impacting the substrate on the opposite side.

During fabrication, these varied feature sizes produced severe loading and lagging. This resulted in greater lateral etching in the cavity on the flap side opposite the hinge, which can be seen in Figure 17. Once the actuator was fully released, the hinges were longer than originally designed. As shown in Figure 17, the flaps were so long that they rotated more than +180° to -180°, impacting the substrate in both the oxidized and reduced states. Therefore, bending data could not be gathered from these samples at either of the redox limits for comparison to other samples. (All other testing was conducted at the redox limits of the sample, 0 V and -1 V in 0.1 M NaDBS.)

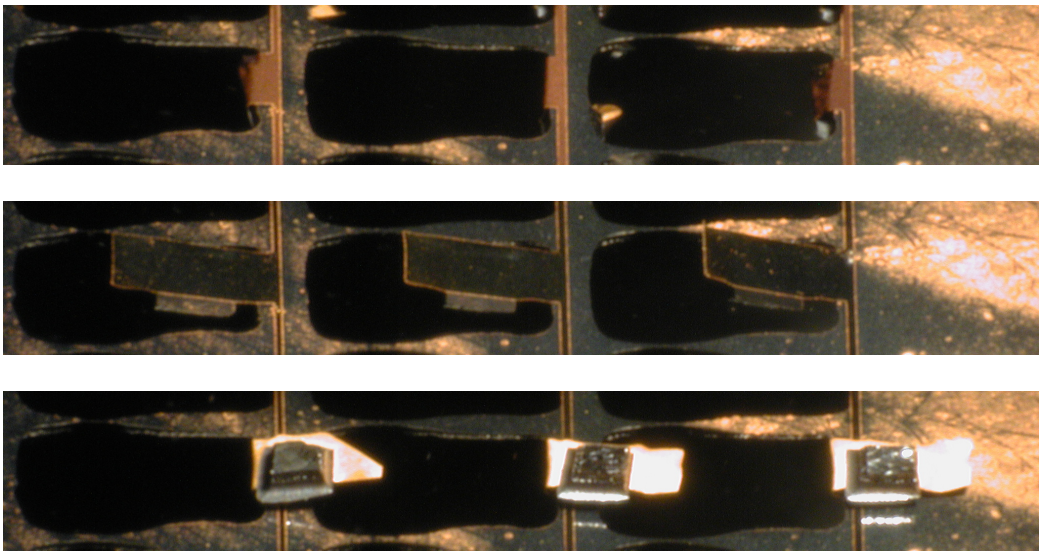

Figure 17. Photos of a set of silicon substrate samples. These actuators produced an exceptional amount of bending due to the combination of the long hinge lengths and the favorable process sequence. Notice the flaps impact the substrate in both the oxidized and reduced positions.

After this set of samples was created, Dr. Christophersen's surface machined samples were shown to actuate reproducibly. This led to further testing on those, instead of continuing this processing technique and creating more samples. This fabrication method was shown to work, however, and to produce moving actuators. Tighter tolerances during future fabrication would allow for greater bilayer hinge length control. Etching further through the substrate with the DRIE process, for example, would allow for less isotropic etch spreading in the final release step. This would more tightly control the eventual hinge lengths and make them closer to the originally intended lengths.

This type of fabrication method could be used to fabricate valves that required no pliability in the substrate, such as in the end of a tube. A thinner silicon substrate would be more desirable than a standard 500 μm wafer to reduce the required etch time. An

oxide thickness greater than 1 μm would allow for longer etching before breaking through the oxide to the silicon, which, once it occurs, just thins the entire wafer.

2.4 Surface Machined Samples

Another type of device was designed by Marc Christophersen, Mr. Liu, Dr. Smela, and myself in order to gather bending angle data from bilayers with more ease and accuracy. This device had several advantages over the original L design. The first was that the samples had no holes beneath the flaps. This allowed for better visibility of the flap edges against the background. Sample geometries were also crisper since they were surface machined as opposed to bulk machined. Another advantage was that there was a greater variety of hinge lengths, allowing for more data points to be used in determining curvature (Section 3.1.3). The hinge lengths ranged from 4 μm to 200 μm, with 13 total different hinge lengths. Built into the mask was also a greater redundancy of samples, as approximately 3000 devices were present on a quarter of a 4'' wafer (Figure 18). The yield was also high, over 90%.

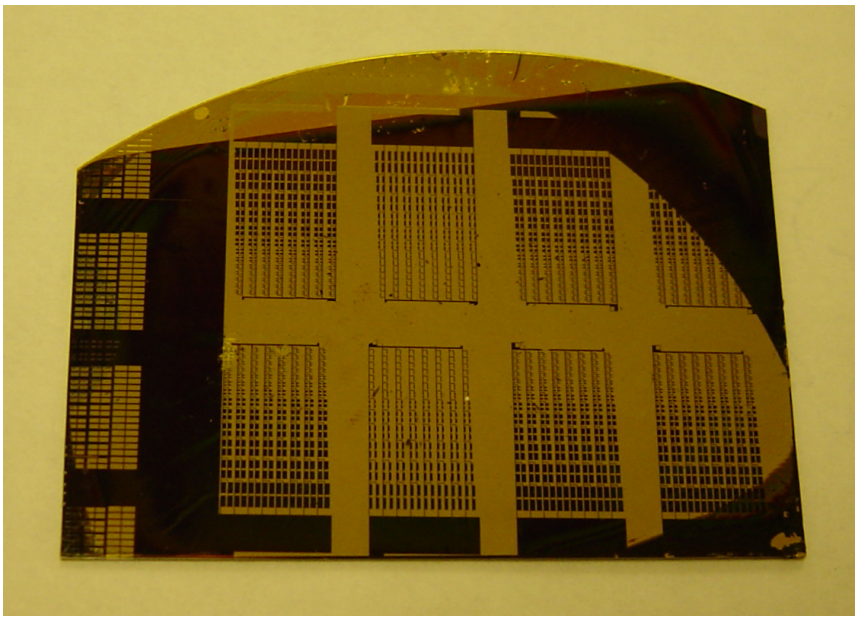

Figure 18. Overview of a quarter wafer showing the immense redundancy and number of hinges for characterization purposes. Samples fabricated by Dr. Christophersen.

The fabrication sequence took advantage of differential adhesion [15] . The best bending data was gathered from this type of actuator. A detailed discussion of the results gathered from these samples is in section 3.1.3.

2.5 Two-Electrode Actuators

Samples that included a counter electrode (Figure 19) were designed to allow leakage testing (discussed in section 3.6). These samples were also made to be larger. Prior leakage testing by Mr. Oh had been done with arrays of small microvalves, which were difficult to observe, and since there were many valves, the source of leaks could not be identified. The possibility that the bilayer actuation force was too small to seal the valve was also considered. The large size of the flap allowed a gasket to be employed as a secondary sealing aid (section 2.7).

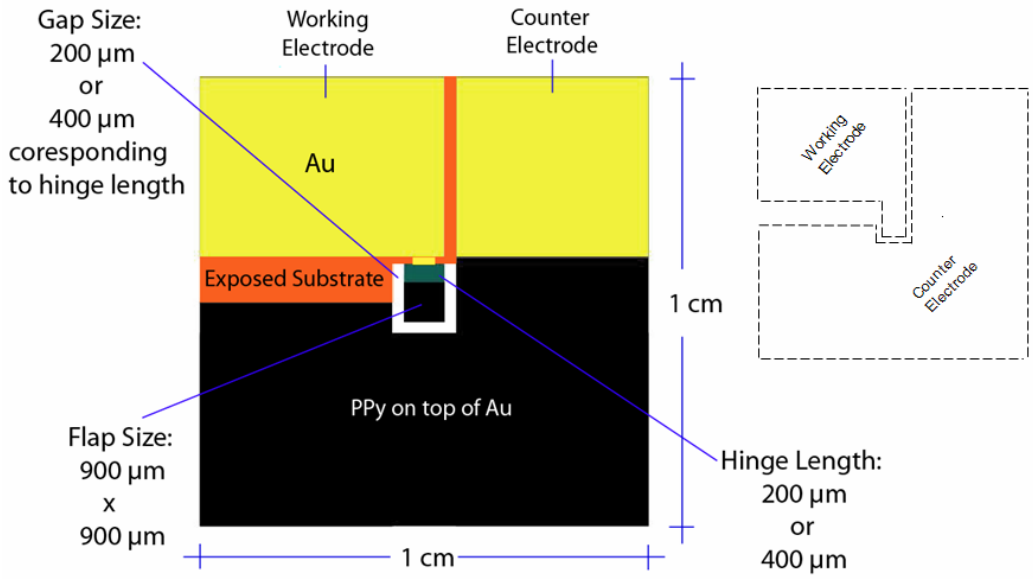

Figure 19. Schematic of the two-electrode design used for testing functionality and leakage.

Testing was conducted to determine the operating voltages for this sample when it was operated in a two-electrode configuration without a reference electrode. The 0 V to -1 V redox limits of PPy are only applicable with a Ag/AgCl reference electrode. From the cyclic voltammograms, an operating range of 0 V to -1.68 V was found to be optimal.

2.6 Seat Development

Following Kapton valve fabrication, the hinge was capable of bending backwards, as well as forwards, through the hole. In order to create a functioning valve, a "seat" needed to be fabricated and attached beneath the substrate for the plug, or flap, to contact in the closed position. Several materials were tested and proved adequate for the initial needs of the seat, including transparency sheets, Kapton sheets, and Mylar sheets.

2.6.1 Hole Creation

A hole needed to be created to allow the liquid to flow through the valve in the open position. The diameter of the hole needed to be smaller than the flap, so that the valve sealed in the closed position. Two methods were considered in order to create holes in the seat materials, RIE and physical drilling.

The square flaps shown in Figure 19 were 550 μm on a side. This was a relatively large size for a "micro" device, and thus allowed the use of drilling. Physical drilling was found to be fast and cheap and to produce clean holes. This made testing of the RIE method unnecessary. (RIE may be a viable technique once devices need to be micro-fabricated.) A 500 μm drill bit with an adapter was purchased from McMaster-Carr. This allowed the hole to be small enough to fit beneath the test flaps, and still have tolerance for some misalignment.

To drill a hole using this small drill bit, the bit was secured in an adapter chuck to allow the bit to be used in a standard drill press. The spindle speed of the drill press (Ryobi DP101 10" Drill Press) was set to 1390 RPM, the press's medium setting. If the speed was too high, the drill bit oscillated, thus widening the hole. A fully fabricated Kapton substrate sample with an affixed drilled transparency seat can be seen actuating in Figure 20.

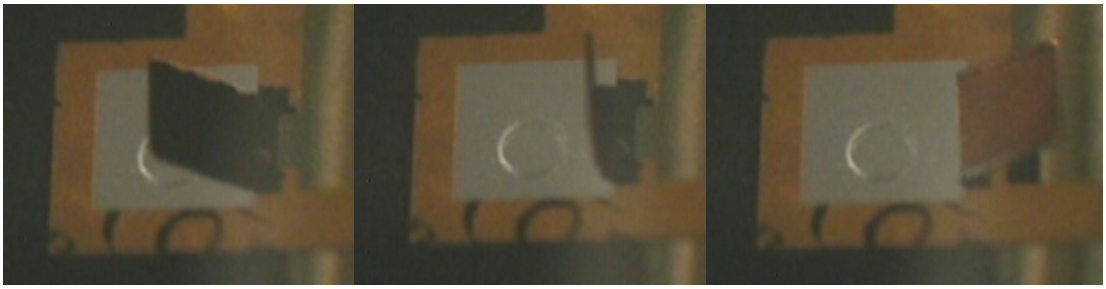

Figure 20. Series of photographs demonstrating a Kapton substrate flap opening over an attached seat with a physically drilled hole.

Upon fabrication of the valves with seats, it was discovered that the valves leaked in the closed state (see section 3.6). An additional step in the fabrication process was then devised to aid in sealing.

2.7 Sealing Gaskets

2.7.1 Gel Rings

A micro-gasket was employed to aid in prevention of leakage. A schematic showing the valve with the gasket can be seen in Figure 21. Several gasketing materials were investigated by Mr. Furst and myself to achieve the desired seal. The most successful used polyacrilymide hydrogels [23].

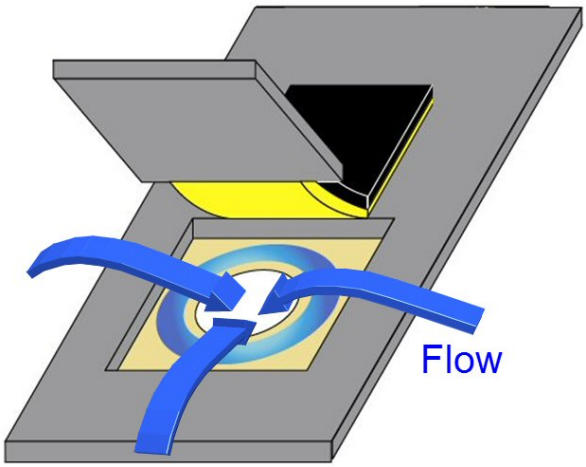

Figure 21. Schematic of the assembled valve with a gel ring positioned beneath the flap for sealing in the closed position.

Transparency film was chosen as the seat material because it provided two advantages. Firstly, the gels adhered better to transparency films than to the other two substrates. Secondly, the transparency films were UV (and visible light) transparent. This was an important consideration for the assembly method described in section 2.7.2, as UV light needed to shine through the seat material to cure the adhesive.

Mr. Furst used the method for polyacrylamide hydrogel fabrication developed by P. Arquint [23]. He began with mixing a base solution. This base solution consisted of 200 mL of ethylene glycol and 500 mg of DMAP (dimethylaminopyridine), a photo-initiator, which was stirred for 5 minutes. The base solution can be stored in the refrigerator almost indefinitely. Next, 50 mL of the base solution was mixed with 10 g of acrylamide. This combination (solution A) was first swirled by hand for initial mixing, and then mixed with a magnetic stirring bar for final mixing. The final solution was made by adding 60 µL of TEDGMA (tri-ethylene glycol dimethacrylate), which is the

crosslinker, for every 3 g of solution A. After the final gel solution was mixed together, a simple test was conducted to be sure the solution would gel. This test involved sucking some of the gel solution into a plastic disposable pipette and placing it under a UV lamp for 90 seconds. The solidified gel was then squeezed and bent to make sure it was pliable and not brittle. Pliable gels are needed for functional gaskets, since they need to readily deform to seal.

To pattern the gel rings, the substrate (transparency film) was placed on an acrylic plate. This was done so that the UV light would not bounce back up and produce poor patterning. The transparency film mask was affixed to a glass plate. A sheet of SealView film (polyolefin) was wrapped around the glass plate, covering the mask. This film assured that the gel adhered to the substrate and not the mask. A few drops of the gel solution were placed upon the substrate surface. The mask was placed over the substrate, and the weight of the mask dispersed the solution into a thin layer (approximately 30 μm). Patterning of the gel rings was conducted using a hand-held 365 nm UV lamp (Spectroline EN-180) or from an aligner bulb (Karl Suss MJB3). The exposure time for both was approximately 90 seconds. A patterned gel ring can be seen in Figure 22.

Once the gel rings were patterned, drilling took place. The gel rings for the testing samples had an inner diameter of 550 μm and an outer diameter of 850 μm. The drill bit had a diameter of 500 μm and fit with some tolerance in the center of the gel rings. A

microscope (Nikon SMZ-1) needed to be used to precisely position the drill bit in the center of the gel ring. The microscope was positioned to view the ring from an angle.

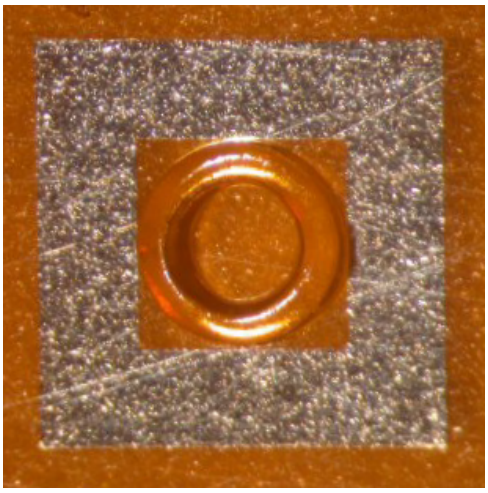

Figure 22. Photo showing a patterned gel ring (550 µm inner diameter, 850 µm outer diameter) . Surrounding the ring is a Cr square with a 900 µm x 900 µm open center to demonstrate the alignment capability. Photo is courtesy of Mr. Furst.

2.7.2 Affixing Process for Seat

Several methods were investigated in order to attach the seat to the actuator. The most successful used photopatternable Loctite glues. (Use of these materials was pioneered in our laboratory by S. Mosely, M. Urdaneta, and R. Delille.) Loctite 3108 was applied to the back of the actuator substrate. A thin wire was used for glue placement. The wire was dipped into the 3108 and dragged along the back of the sample, with enough room for the glue to spread during assembly and not touch the actuator itself. Once the UV patternable glue was applied to the sample, it was taped upside down onto a clear glass plate. The transparency sheet was taped to another glass plate. This setup allowed for the hole in the transparency film to be aligned to the sample below because the substrate

could be seen through the film. Once aligned, the two sheets were pressed together within the aligner. Exposure within the MJB3 at 365 nm took place for 1 minute. A schematic of this process can be seen in Figure 23. One the top and bottom layers were affixed, the tape was peeled off and the sample removed.

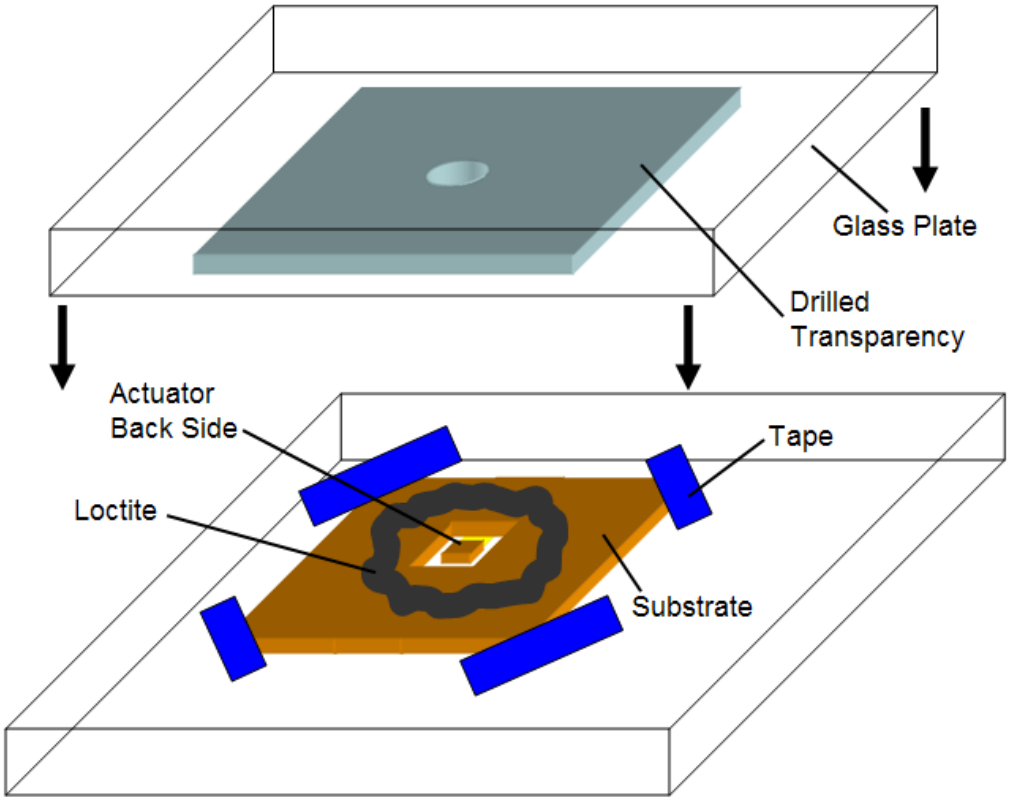

Figure 23. Schematic of two-electrode valve assembly process.

Originally, glue was tried to adhere the actuator to the seat. This was found to be sloppy and ruined most samples. An adhesive that would not adhere until the alignment process was completed was needed. Typical glues could not provide both the flexibility to be set on command and the quick set times of UV curable glues. Loctite's UV curable glue line also has many variations, which may accommodate varying needs for different applications.

2.8 Chapter Conclusions

The evolution of sample types from a Kapton substrate to a titanium substrate to a silicon substrate has resulted in several viable fabrication methods for future microvalves. Provided the valves would not be used in the body, Kapton is a distinct possibility. Titanium substrates are also promising for this application, and in addition they have the possibility to be used in other bioMEMS applications. The development of a bulk titanium substrate etching process compatible with MEMS processing is therefore significant.

The culmination of the work into a two-electrode, fully assembled microvalve ultimately proved successful. The device only needs to be optimized for force output to overcome the pulldown force exerted by liquid pressing against the back of the closed device (see section 3.6). The sealing gasket was a success in that the microvalves assembled without them leaked and those with them did not.

Future work should focus on making the process a batch process. Currently the seat fabrication and seat attachment is labor and skill intensive. Glue placement and pressure applied in the aligner during assembly, in particular, required skill developed over time.

Chapter 3 Bending, Force, and Leakage Measurements

To successfully design a device using PPy/Au bilayers as the actuating mechanism, there are many design parameters that affect one another that need to be understood. A design will undoubtedly have requirements for stroke and output force. The experiments conducted for this thesis help to provide this understanding needed for design. In particular, how the design parameters affect bending, both at room temperature and elevated temperatures, as well as output force was investigated. Microvalves were also tested for their sealing capabilities in a testing apparatus and in a live animal test.

In the case of the female urinary incontinence valve system, force will be the parameter of primary importance. This is because the flaps will need to overcome a pull-down force exerted by the pressure of the urine in the bladder in order to open. Bilayer output force is determined by PPy thickness, PPy/Au thickness ratio, and hinge width. However, the flap needs to bend out of the way of the flow once the initial pull down force is overcome and the valve opens. This means that the hinge must be long enough, since a given thickness ratio and initial Au thickness correspond to a given curvature, in order to bend 90° or more from the port hole. These relationships are explained in detail in section 3.1.3.

To fully characterize the PPy/Au bilayers, there were many experiments that needed to take place to relate the design parameters to the output parameters. Relating these values

involved varying the PPy/Au thickness ratio, Au thickness, and hinge length. Various types of samples were created by Dr. Christophersen, Mr. Furst, and myself to determine these relationships.

3.1 Bending Angle Measurements

This section describes the approaches that were taken to measure, quantify, and model bending performance. Bending angle was used to obtain curvature. Curvature has units of 1/m and is the inverse of the radius of curvature. A better bender has a larger curvature value.

3.1.1 Previous Methods – Side On

Carrying on Mr. Oh's previous work [3], further studies were conducted on bending angles. Bending angle measurements were at first done in the same manner as Mr. Oh's experimentation, in that angle measurements were taken from a side-on view.

The L-shaped samples were hung perpendicular to the surface of the table in the electrochemical cell and photographed through the microscope from overhead. A portion of a side-on view of a Kapton substrate sample can be seen in Figure 24.

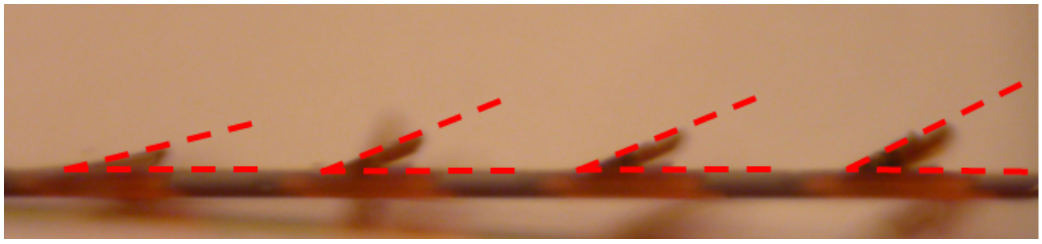

Figure 24. Photo showing the bending angle measurement technique using the side-on view on Kapton substrate samples. One row at a time was measured this way. The angle could be measured directly between the two red dashed lines.

As was discussed previously, it proved difficult to obtain accurate data from Kapton samples. This was not due to viewing method, but to fabrication issues.

3.1.2 Previous Methods – Slightly Angled

Photographs were also taken of the samples from a slightly angled view, of which an example can be seen in Figure 25. The main advantage to this method was that it allowed for several rows of devices to be photographed simultaneously by nearly closing the aperture on the microscope to increase the depth of focus. The resolution of the digital camera allowed for isolation of individual flaps during subsequent evaluation.

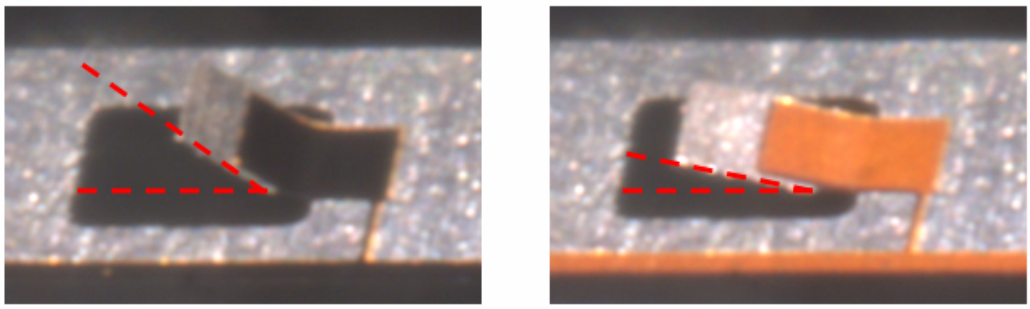

Figure 25. Photo showing the bending angle measurement technique using the slightly angled view. Several rows at a time were measured this way. The angle could be measured between the two red dashed lines.

The angle measurements were, unfortunately less accurate than those produced by the side-on method. The lack of accuracy was due to inconsistent viewing angle from day to day. These angles needed to be taken into account in curvature calculations.

3.1.3 Final Method – Overhead

The surface machined sample type (Figure 18) designed and fabricated by Dr. Christophersen allowed for measurements to be taken from directly overhead more easily than the L-shaped samples: since there was no through-hole beneath the flap, visualization was easier. The ability to take measurements on several hinges simultaneously was preserved.

All surface micromachined samples were brought up to the step just prior to release by Dr. Christophersen and stored dry until needed for testing. This allowed the hinges to remain unreleased until the moment they were to be used. From the stored state, they needed only to be placed in Au etching solution (two minutes per 1000 Å of Au at room temperature), followed by a four minute photoresist removal/flap release soak in ethanol. Following those two steps, the actuators were ready for use.

For the curvature measurements, the surface machined samples were secured to a plexiglass holder with electrical connection screws protruding upward (Figure 26). This holder was partially immersed into the testing electrolyte, which was contained within a shallow Pyrex dish. The sample (working electrode) was electrically connected by

clipping to the screws, which protruded from the surface of the liquid. A graphite counter electrode was placed in the dish and electrically connected, through a portion protruding from the liquid, with a flat copper clip. Finally, an Ag/AgCl reference electrode was placed between the working and counter electrodes. The reference was approximately 1 cm from the counter. A clip was used to electrically connect the reference. All bending angle measurement tests in this section were conducted in 0.1 M NaDBS. All three electrodes were connected to a potentiostat.

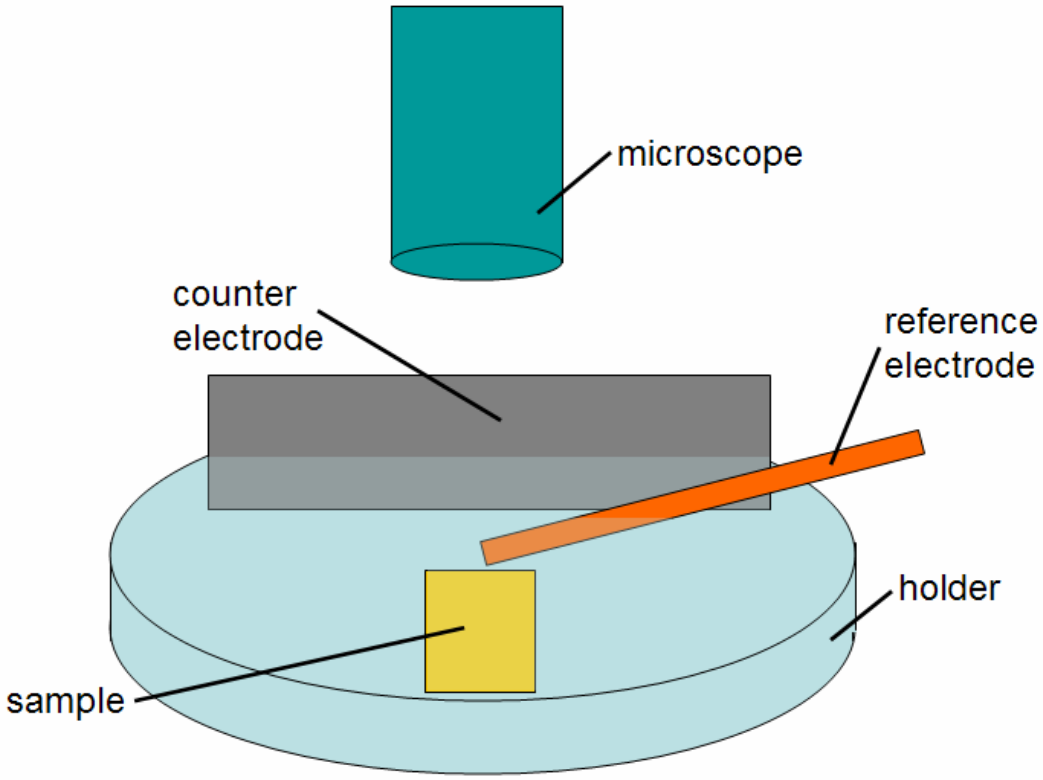

Figure 26. Schematic showing the testing setup for overhead bending angle testing.

Before curvature measurements in NaDBS, the samples were cycled between 0 V and -1 V vs. Ag/AgCl 15 times to break in the samples. Cycling was done at a ramp rate of 50

mV/sec. This allowed the first cycle effects of PPy [24] to be eliminated during testing. The first cycle of PPy typically exhibits behavior much different than that of subsequent cycles.

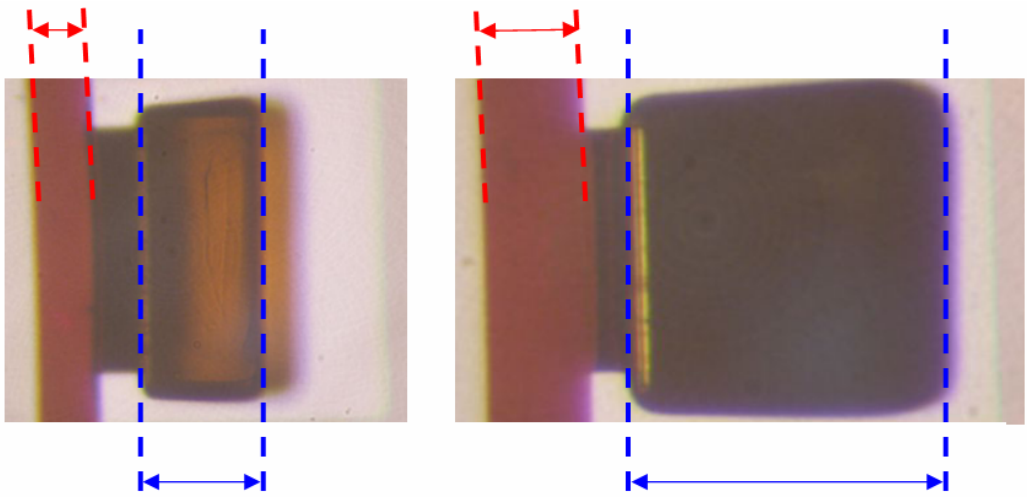

Figure 27. Photo showing the bending angle measurement technique using the overhead view. The left photo shows a bent hinge and the right, a flat one. Several rows at a time were measured this way. The length of the blue arrows (perceived flap length) were compared to the length of the red arrows (a PPy strip next to the sample which was of known width). Knowing the flap length, this would geometrically yield the amount of bending.

3.2 The Timoshenko Equation

A model originally designed to predict the behavior of thermally actuated metal bilayers, the Timoshenko equation, provided a starting point [25] to model the PPy/Au bilayers. This model assumed that all strains and stresses in the x and y directions were constant. It was also assumed that the curvature κ was small compared to the beam thickness: $\kappa << h_1 + h_2$, where $\kappa = 1/R$ and R is the radius of curvature. The variables were layer

thicknesses h, Young's moduli E, and actuation strains ε. Two ratios were defined: $m = h_1/h_2$ and $n = E_1/E_2$, where 1 corresponds to the PPy layer and 2 to the Au layer.

In this model,

$$\kappa = \Delta T \frac{(\varepsilon_1 - \varepsilon_2)}{h_2} \frac{6mn(1+m)}{1+4mn+6m^2n+4m^3n+m^4n^2} \quad (1)$$

The only changes from the Timoshenko model was to consider the 'thermal expansion coefficient' (α) as a 'voltage expansion coefficient' (ε), which would also change the temperature change (T) to a voltage change (V). In the case of polypyrrole, this replaced the α with the in-plane actuation strain value. The gold would, of course, have a strain of zero induced by the application of voltage. This equation predicts a peak in curvature as a function of the thickness ratio m (Figure 28).

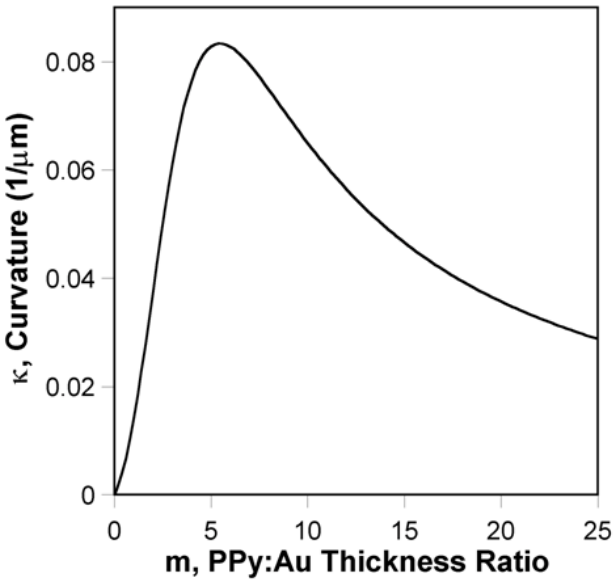

Figure 28. A graph of the Timoshenko equation versus the layer thicknesses. In this example, h_2 = 100 nm, E_1 = 0.2 GPa, E_2 = 83 GPa, and α = 5%.

3.3 Curvature in NaDBS at Room Temperature

In this section we present base-case data on bilayers cycled in 0.1 M NaDBS at room temperature from Dr. Christophersen. From a set of hinge lengths having identical PPy/Au thickness ratios, a curvature value for that thickness ratio could be accurately obtained. From plots of bending angle vs. hinge length, the curvature value for each thickness ratio was calculated from the slope of what was a linear relationship, which can be seen in Figure 29. Note the linear portion becomes flat as the last four measurements in this case are all 180°. This is due to the sample bending completely around to touch the substrate, at which point it can bend no further.

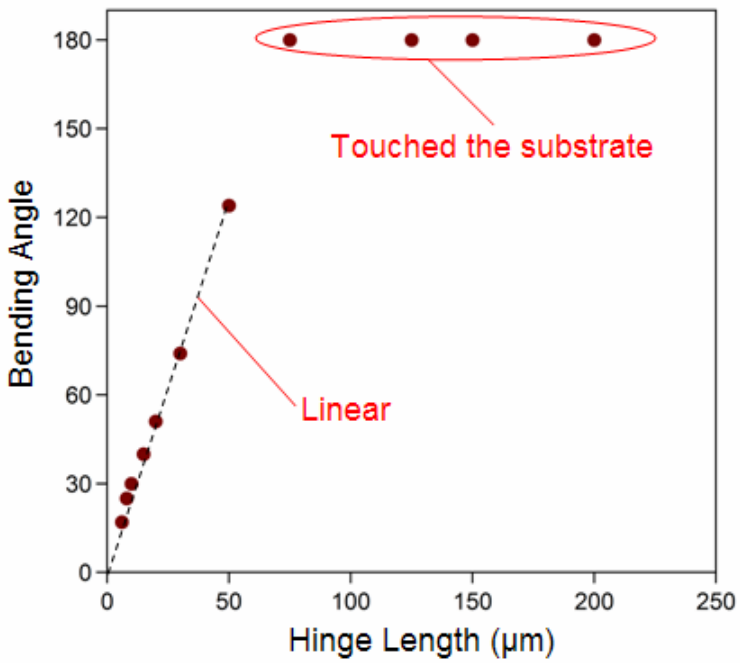

Figure 29. Example plot of bending angle vs. hinge length, in this case for a thickness ratio of 20,750 Å PPy:1000 Å Au. Each graph of this type produced a linear portion, yielding the curvature value. Data from Dr. Christophersen.

A graph similar to that in Figure 29 was created by Dr. Christophersen for each thickness ratio fabricated. A curvature value was calculated for each point within the linear sloped portion of each graph using equation (2)

(2) $\kappa = [\pi * (\text{bending angle})] / [180^{o} * (\text{hinge length})]$

From these curvature values, an average value was found and a standard deviation calculated. The standard deviation was obtained by individually calculating the curvature value for each point on the linear portion of the plot and then comparing all of them to the average value already calculated. Each of these graphs similar to Figure 29 produced one point in Figure 30.

Curvature vs. PPy/Au thickness ratio data were gathered for three different Au thicknesses by Dr. Christophersen (Figure 30). The curves have a peak, as predicted by equation 2 and shown in Figure 28. The thickness ratio at which the peak value occurs remains consistent at approximately 5:1. This Au thickness affects the magnitude of the peak.

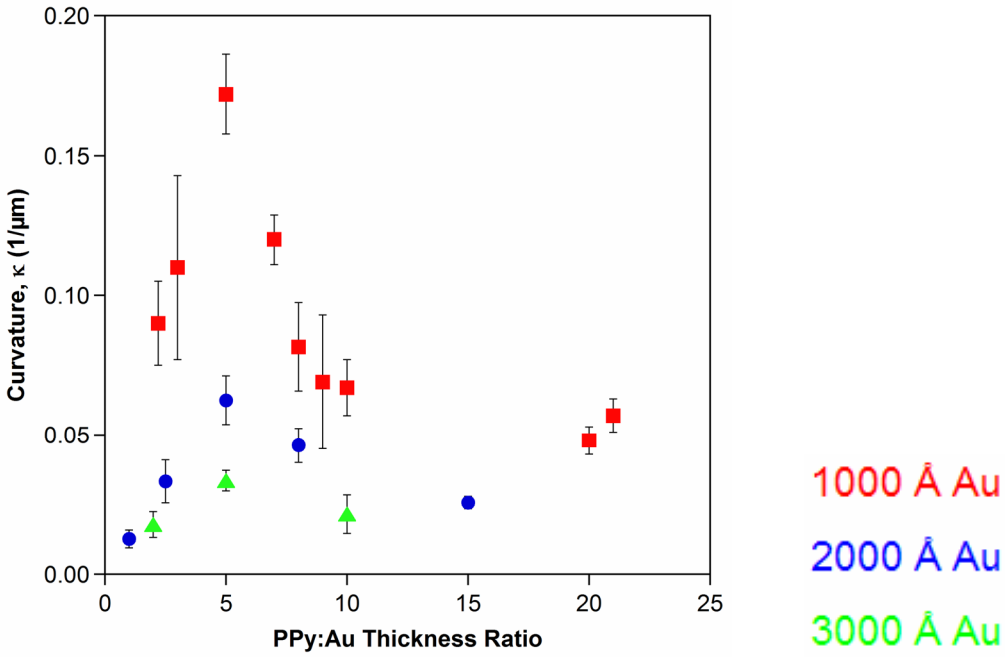

Figure 30. Plot of curvature vs. PPy/Au thickness ratio for various initial Au thicknesses cycled within 0.1 M NaDBS. This plot demonstrates that peak curvature occurs around a thickness ratio of 5:1. Note that as the Au thickness increases beyond that, the peak curvature value decreases as well. The data were gathered and analyzed by Dr. Christophersen.

A reliable fabrication method and observation method had finally been achieved. The data gathered from such samples can be used to design actuators with specific curvatures, depending on the task. Future work should concentrate on other PPy deposition recipes that have been presented in the literature so that the various types of PPy can be quantitatively compared for the first time.

3.4 Curvature: Temperature Effects

Once the curvature relationship was established with respect to PPy/Au thickness ratio at room temperature, testing needed to be conducted at higher temperatures in order to

evaluate bilayer performance in environments such as the body. Body temperature is approximately 37 °C, whereas room temperature is approximately 23 °C.

3.4.1 Temperature Effects in NaDBS

For the plot shown in Figure 31, a new sample was used for each of the temperature levels, and it was run in 0.1 M NaDBS. Each sample was first cycled five times at room temperature at a sweep rate of 50 mV/sec. A data point was taken holding the sample first at the oxidized state and then in the reduced state. The second data point was taken at the elevated temperature holding it once again in the oxidized state and then the reduced state. The sample was cycled five times at the elevated temperature and a third data set taken thereafter. Each point after was taken using this five cycle / data set approach. The final data point for each temperature was taken after a minimum of one hour of settling time once the heat was turned off. After this time, the sample was cycled five times at room temperature and a data set taken thereafter.

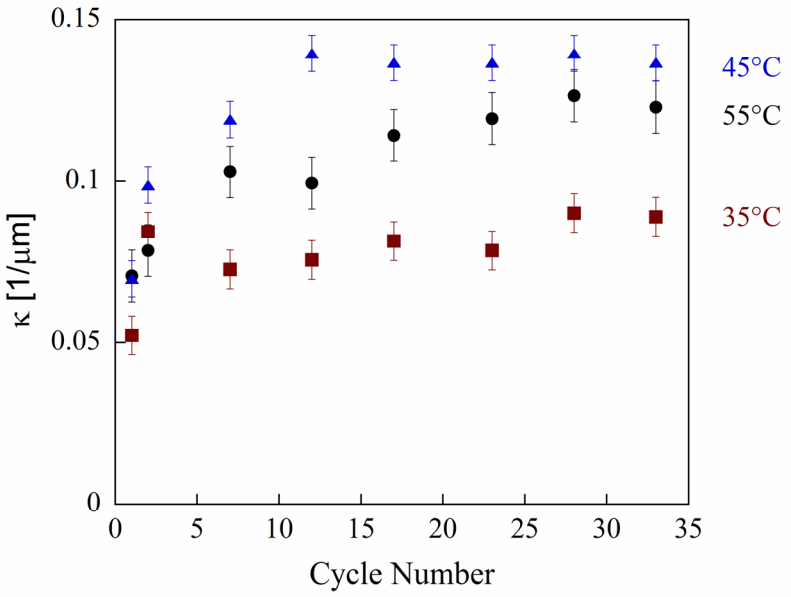

Figure 31. Plot showing curvature values in the oxidized state. The first cycle number shows curvature for that sample at room temperature after 5 cycles. The second cycle number shows curvature for that sample at the designated elevated temperature prior to any cycling at that temperature. The remaining data were taken every five cycles. The final point was taken at room temperature.

The data displayed in Figure 31 show an interesting temperature effect. As the temperature was increased during cycling, the overall curvature in the oxidized state increased. It is also noticeable that at 55 °C the bending began to decrease, as well as to scatter. These data suggest an effect negatively impacting the bending beyond approximately 45 °C. The final data points also suggest that this temperature effect is non-reversible, although only one data point was taken for each sample after cooling.

The plot shown in Figure 32 shows that the temperature effect is cycle dependent and not time dependent. A sample was cycled five times at room temperature in 0.1 M NaDBS and held in the oxidized and reduced states to be photographed for data collection. As a next step, the sample was raised to 45 °C and held there for 30 minutes, then allowed to

cool back to room temperature. The second data point was gathered at room temperature. Since no cycling took place at the elevated temperature, and no discernable curvature difference was observed, it can be seen that time spent at an elevated temperature is not a dominant effect. The cycling at elevated temperatures is the driving input affecting curvature change.

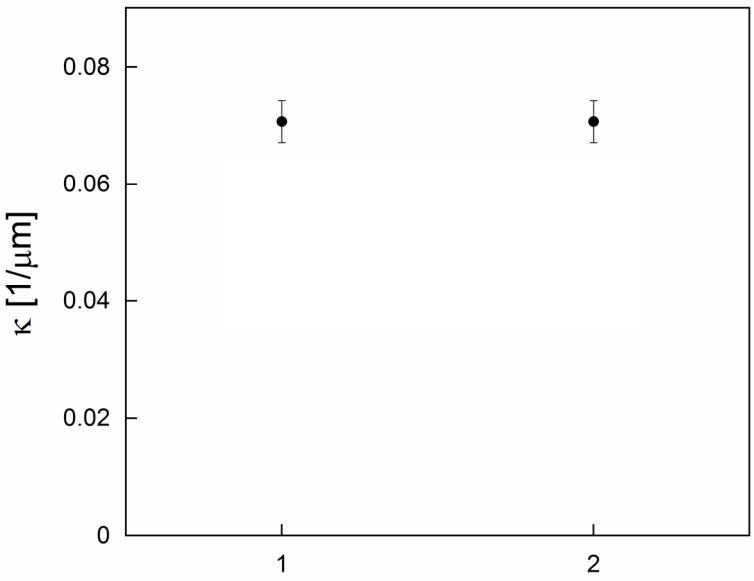

Figure 32. Plot showing the curvature of a 15:1 thickness ratio sample with 1000 Å Au following a holding period at various temperatures within 0.1 M NaDBS. The first point (1) was taken after five cycles at room temperature in the oxidized state. The second point (2) was taken at room temperature after 30 minutes sitting at 45 °C following the initial room temperature cycles.

In Figure 33, the 2000 Å Au data of Figure 30 are compared to those from an identical sample tested at 45 °C for various thickness ratios. The data points collected at 45 °C were obtained by cycling the sample at 45 °C 15 times and then holding in the oxidized and reduced states while the actuators were photographed. The cycling was done by cyclic voltammetry at a sweep rate of 50 mV/sec.

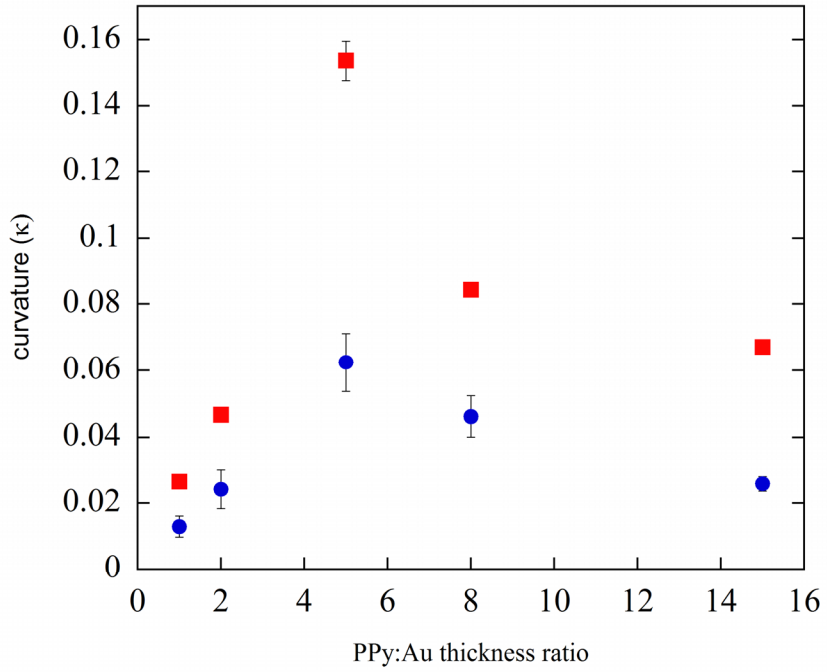

Figure 33. Plot showing the 2000 Å Au portion of Figure 30 (blue circles), which was taken at room temperature, and comparing those curvature values of identical samples cycled at 45 °C (red squares). Notice the increase in overall curvature due to the higher temperature.

The behavior exhibited in Figure 33 needed to be further investigated. This was done by running the same type of experiment on a 1000 Å Au sample at 45 °C and comparing the data to that of the room temperature tests. The curvature for the peak thickness ratio of 5:1 was raised from 0.17 to 0.34 (Figure 34).

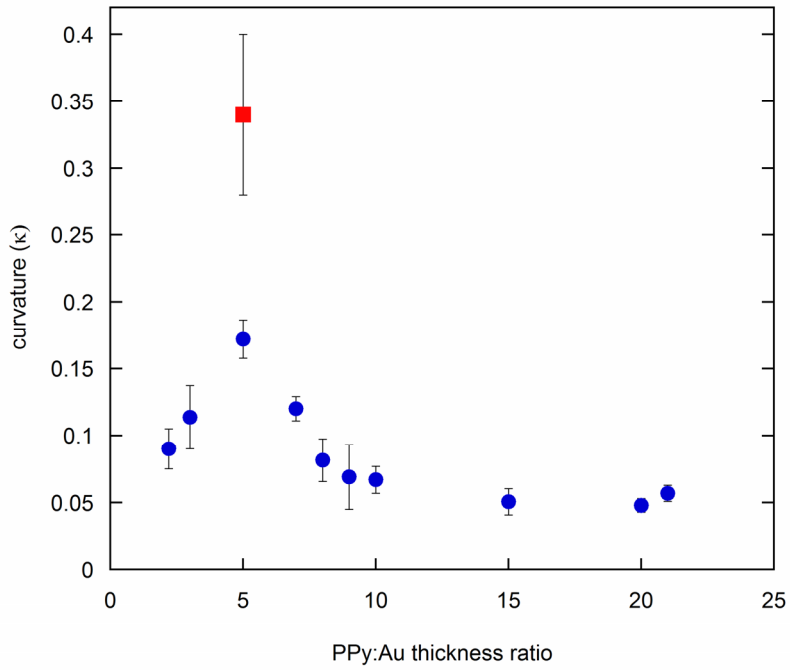

Figure 34. Plot showing the 1000 Å Au portion of Figure 30, taken at room temperature, and the curvature of an identical sample cycled at 45 °C.

It can be seen that the greatest curvature value still lies at a thickness ratio of 5:1 in Figure 33. The curvature at the elevated temperature is approximately double the value exhibited at room temperature.

The interesting bending behavior captured during the temperature testing allowed for some speculation to be made using the Timoshenko equation model. The variable that could be changed to most reasonably account for the temperature effect was the PPy strain. In the model graphs shown below, E_{PPy} was held at 0.15 GPa and E_{Au} at 54 GPa [26]. A PPy strain value of 8% was shown to best approximate the room temperature behavior, as can be seen in Figure 35. A PPy strain value of 18% was shown to best approximate the room temperature behavior, as can be seen in Figure 36. All models

were adjusted to best approximate the peak value occurring at a PPy/Au thickness ratio of 5:1.

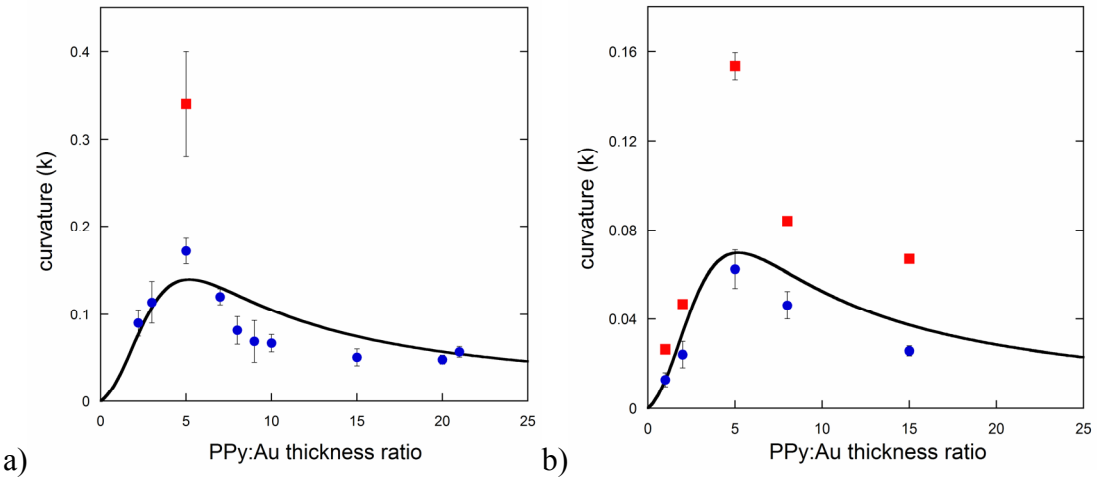

Figure 35. Room temperature Timoshenko type bilayer modeling for (a) 1000 Å Au and (b) 2000 Å Au. All blue points are the curvature values at 25 °C (room temperature), and all red points are the curvature values at 45 °C. The only value changed within the model between these two graphs was the Au thickness. The model best captured the room temperature curves with values of E_{PPy}=0.15 and α_{PPy}=0.08.

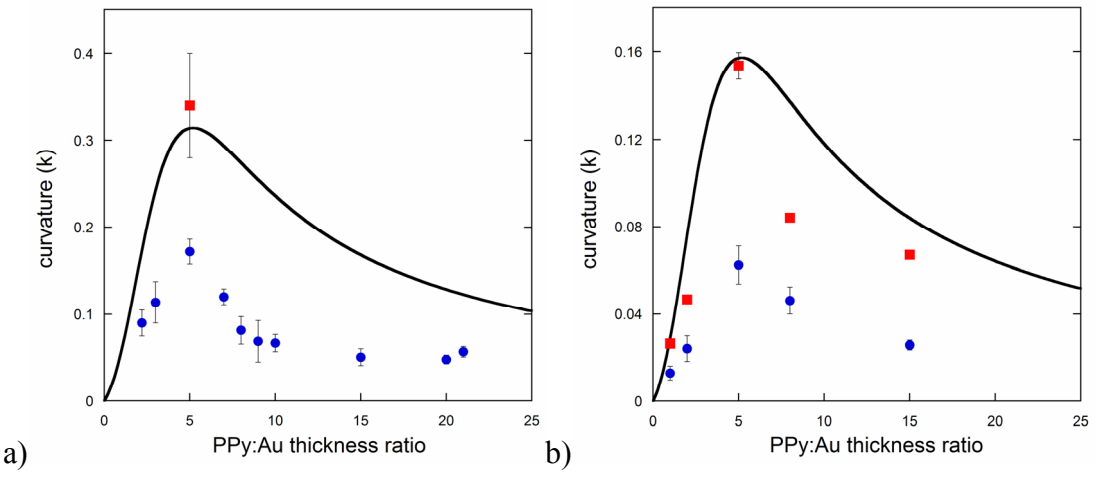

Figure 36. Elevated temperature Timoshenko type bilayer modeling for (a) 1000 Å Au and (b) 2000 Å Au. All blue points are the curvature values at 25 °C (room temperature), and all red points are the curvature values at 45 °C. The only value changed within the model between these two graphs was the Au thickness. The model best captured the 45 °C temperature behavior with values of E_{PPy}=0.15 and α_{PPy}=0.18.

Testing was done to determine the influence of PPy's CTE (coefficient of thermal expansion) on the temperature effects that had been observed. The same experimental setup as described in section 3.1.3 was used. A 7:1 thickness ratio sample (with 1000 Å of Au) and a hinge length of 10 μm were used. These samples were from the same batches used in all the temperature experiments. The actuators were cycled five times in 0.1 M NaDBS at room temperature. The oxidized state curvature was measured. The solution temperature was raised to 45 ºC with the sample held at 0 V (the oxidized state) throughout, which took approximately 15 minutes. The bending angle decreased from 34° to 31.4° for one flap and from 33.5º to 31.4º for another. The sample was switched to the reduced state while at 45 ºC and photographed, then cooled back to room temperature and photographed while being held in the reduced state throughout, which took approximately 35 minutes. In the reduced state case the bending angle increased from 15.5º to 24.6º for one flap and from 17.6º to 26º for another.

Using these data and the Timoshenko equation described in section 3.2 it was possible to back out the coefficient of thermal expansion of PPy. Inputting a CTE of 14.2 for Au [27], the curvature values corresponding to the bending angles, and the hinge dimensions into the Timoshenko equations allowed for solving for the CTE of PPy. The curvature calculated from the bending angles and bilayer dimensions, for the oxidized cases, changed from 0.055 to 0.059 1/μm in one case and from 0.055 to 0.058 1/μm in the other. This was a curvature change of 8.4% and 6.6% respectively. The curvature change caused by the cycling temperature effect, with these sample parameters, was on the order of 100%. This shows that the CTE of the PPy is negligible when evaluating the

temperature effects observed above. The curvature calculated for the reduced state cases changed from 0.042 to 0.027 1/μm in one case and from 0.045 to 0.031 1/μm in the other.

The CTE of PPy was calculated using equation (3). An example of which can be seen in equation (4) using m = 7000 Å /1000 Å = 7 and n = 0.1 GPa / 54 GPa = 0.00185. This yields a value of 4.1453 for the (1+4mn+6m2n+4m3n+m4n2) term and a value of 0.62222 for the 6mn(1+m) term. The CTE of PPy(DBS) in the oxidized state was found to be 109 μm/m°C for the first case and 140 μm/m°C for the second case. The CTE for the reduced state was found to be 481μm/m°C for the first case and 515 μm/m°C for the second.

(3) $$\varepsilon_{PPy} = \frac{\Delta\kappa * h_{Au} * (1 + 4mn + 6m^2n + 4m^3n + m^4n^2)}{6mn(1+m)\Delta T} + \varepsilon_{Au}$$

(4) $$\varepsilon_{PPy} = \frac{(0.059 - 0.055) * 0.1 * 4.145}{0.622 * 21} + 14.2 * 10^{-6} = 141 \frac{\mu m}{m \cdot °C}$$

Further testing should be done to quantify the exact value, as it is interesting information. For the purposes of this thesis however, this suggests that the CTE has a minimal effect on the PPy temperature effects observed.

Polymer CTE values fall over a wide range. For example, silicone has a value of 170 μm/m-°C [28], polyethylene has a value of 140 μm/m-°C [29] and Kapton has a value of 20 μm/m-°C [30]. Unfortunately the only published value found for PPy was a "calculated" value and neither the calculation nor the assumptions were given [31].

Based on the CTE's of these other polymers, the values for PPy found experimentally do fall in the same order of magnitude.

Temperature has a minor effect on peak positions in CV's of PPy(DBS). The shape of the CV's change significantly however, and encompass a greater area. This effect can be seen in Figure 37, which shows the polymer being cycled during temperature testing. One curve corresponds to room temperature and the other to 45 °C. The first anodic peak shifts closer to the center of the operational voltage with increasing temperature.

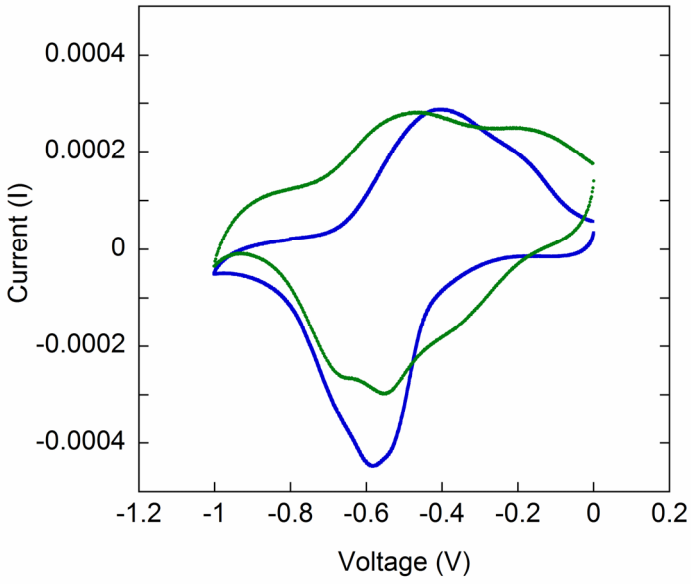

Figure 37. Cyclic voltammograms of PPy actuators in 0.1 M NaDBS. The blue CV corresponds to 23 ºC and the green corresponds to 45 ºC.

All data reported on the temperature experimentation was for PPy's oxidized state. This was done as a result of bending limitations imposed by the sample design. Since the bilayers were fabricated on the surface of the substrate, they could only bend over a range of 180º. The dramatic shift in bending angle caused by the elevated temperatures made it

necessary to choose if the oxidized state or reduced state would be analyzed, as the opposite state would contact the surface. No curvature data can be taken from a bilayer device that is lying flat on the substrate surface, as its true position without the substrate blocking is unknown. Dr. Christophersen had conducted his room temperature curvature measurements in the oxidized state, so I chose to do mine in the same state, as this would allow for comparisons to be drawn between room temperature and elevated temperature bending performance. Future work should further characterize PPy curvature performance by analyzing the reduced state.

Further testing should be conducted around 37 º C. Any future design work will have to consider these temperature effects, as the amount of bending would be incorrect if not taken into account.

The negative effect on the PPy that occurred at 55 º C also needs further investigation. Reliable data collection at this temperature proved difficult, as repeatability was harder to obtain than with lower temperatures. Also, will the bending continue to decrease if even higher temperatures are applied to the sample?

All data collected thus far indicates that the temperature effect, which increases bending, is non-reversible. Future testing should confirm this by running experiments similar to those examined in this thesis, but running sample tests over several hours following cool down to room temperature.

Future work should also obtain curves similar to those in Figure 33 for a range of temperatures. Perhaps a maximum rise in peak values can be observed.

3.4.2 Temperature Effects in Urine

To continue towards developing a microvalve for use with urinary incontinence, performance in urine needed to be evaluated. It was shown that PPy/Au bilayers functioned at elevated temperatures using NaDBS as the electrolyte. Applications using urine from the human body would need to be performed at temperatures exceeding room temperature as well. Human urine was obtained from Quantimetrix Corporation.

The first set of urine tests were bending angle studies which were conducted on the silicon substrate actuators. These samples were immersed in urine and first cycled 10 times at room temperature. The sample was held and photographed at 0 V and -1 V respectively. The urine was then raised to 32º C, and the same cycling and photographing steps were followed. As in the NaDBS tests, the overall bending of the sample increased at the elevated temperature. However, once the sample was brought up to 40º C, the amount of bending dropped dramatically. Following the testing at 40º C, the sample was brought back down to 32º C and tested again. The bilayers did not increase their bending to the level previously seen at 32º C. The reduced bending at 40º C remained as a permanent effect, but in urine high temperature decreased bending, as opposed to the increase seen in the NaDBS. Each of these temperature steps can be seen in Figure 38.

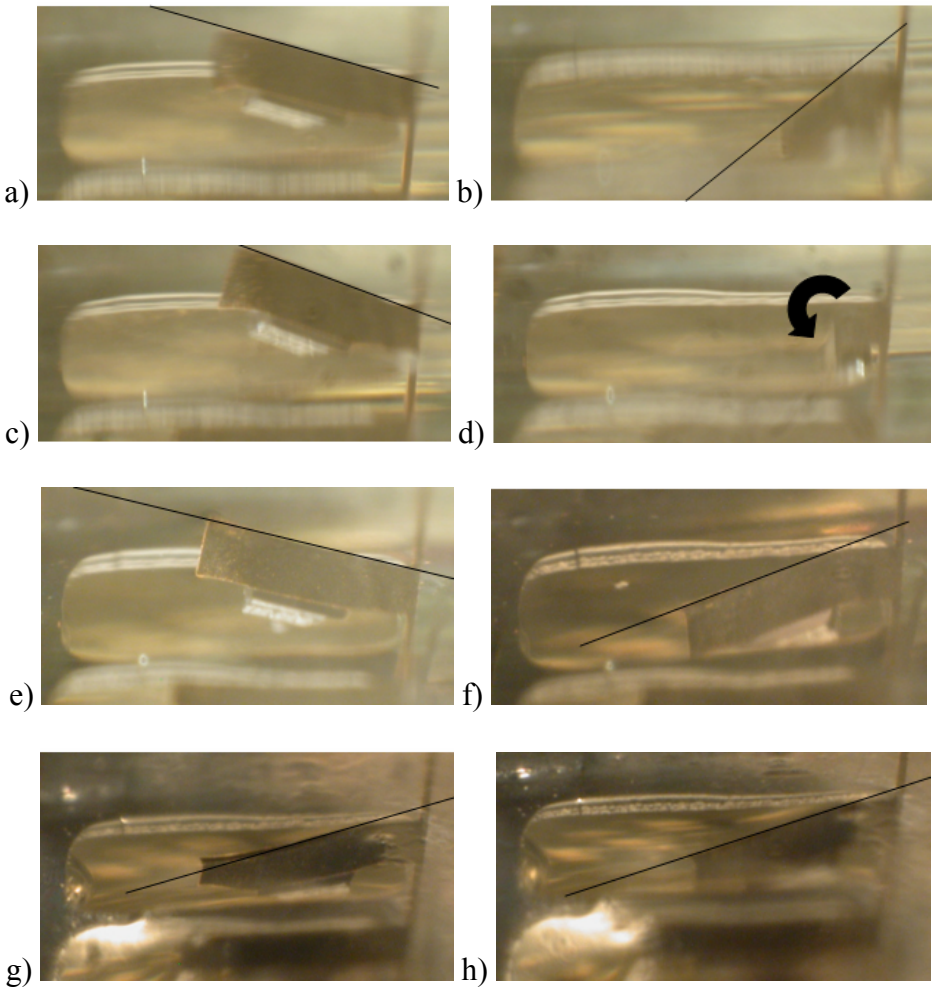

Figure 38. A progression of temperatures was applied to a silicon substrate sample in urine. At each temperature, the sample was cycled 10 times and then photographed. The sample began at room temperature (25 ºC), was brought up to 32 ºC, brought up to 40 ºC, and then brought back down to 32 ºC. a) 0 V at 22ºC b) -1 V at 22 ºC c) 0 V at 32 ºC d) -1V at 32 ºC (which bent all the way under the substrate to touch the other side) e) 0 V at 40 ºC f) -1 V at 40 ºC g) 0 V at 32 ºC h) -1 V at 32 ºC.

Thin films of PPy were cycled in urine to observe the effect of temperature on the cyclic voltammograms. The samples were created by sputtering a layer of Cr/Au on a silicon wafer and then depositing PPy on top of that. Small rectangular samples were cut from the wafer and placed in the electrochemical cell used for bending angle studies. Four sets of 5 cycles was followed by photographing at the redox limits of 0 V and -0.8 V. One set

of 10 cycles followed by one final set of 20 cycles was then applied, each of which were photographed also. These tests were conducted at 25 º C, 30 º C, and 45 º C with a fresh sample for each temperature test. The cyclic voltammogram shape over time can be seen in Figure 39. Notice that with increasing temperature, the CV flattens out dramatically, showing lessened oxidation and reduction reactions. An overlay of the 14th cycle at each temperature tested is shown in Figure 40. Even at room temperature, however, the peaks decreased with time, which does not occur in NaDBS.

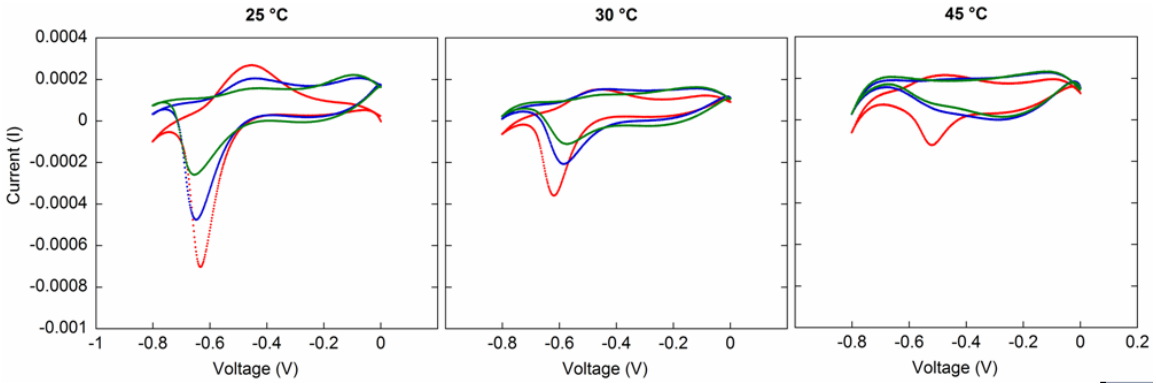

Figure 39. Cyclic voltammograms of PPy in urine taken at 50 mV/sec . The 2nd CV is in red, the 14th in blue and the 49th in green.

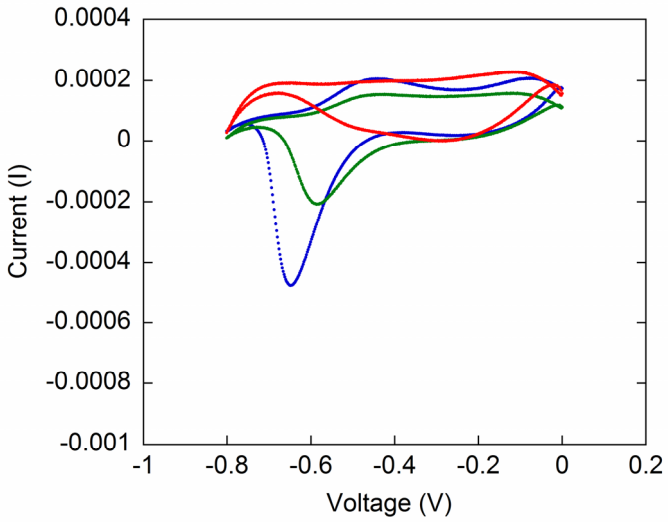

Figure 40. An overlay of 14th CV taken at three temperatures in urine. (red=25 ºC, blue=30 ºC, and green= 45 ºC.)

A decrease in peak height indicates either a loss in PPy electroactivity or delamination. The former can be caused by degradation of the polymer or by layers on the surface that block the transport of ions.

Bilayer failure within urine was visually evident by either large scale delamination or by spots in the PPy of a different color. Delamination occurred in samples cycled in NaDBS as well, but typically after many more cycles. Hundreds or thousands of cycles were typical in NaDBS, even at elevated temperatures. In urine, failure due to delamination occurred, at temperatures above room temperature, within tens of cycles in about 1/3 of the samples tested. An overhead example of large scale delamination can be seen in Figure 41. This picture shows entire hinges, flaps, and connection lines peeling off the substrate during actuation.

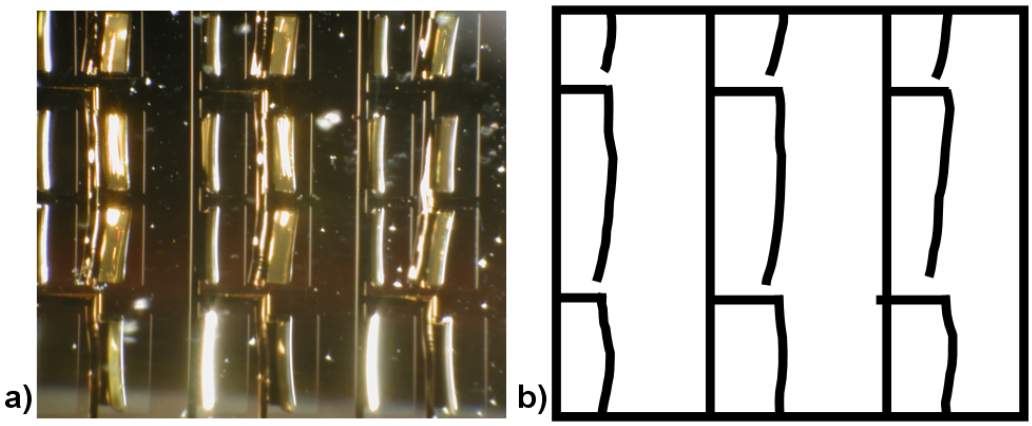

Figure 41. a) A photograph showing delamination during a trial in urine. b) A tracing of the Au connection lines from the photo, which should all be straight, showing the Au peeling up from the surface and curling away from the substrate.

The second of the two typical types of failure at in urine was the appearance of colored spots in the PPy. Once such spots appeared, more cycles (in the tens of cycles range) resulted in spots in every part of the PPy (Figure 42). Each small spot grew in diameter with each successive cycle. As more spots appeared, actuation came to a halt. Both photos in Figure 42 were taken in the reduced state. PPy changes color when cycled from its oxidized to reduced states. The spots are red on what was supposed to be green (the green color is an interference effect [32]. It is not yet clear whether these spots indicate loss of eletroactivity or some degree of delamination.

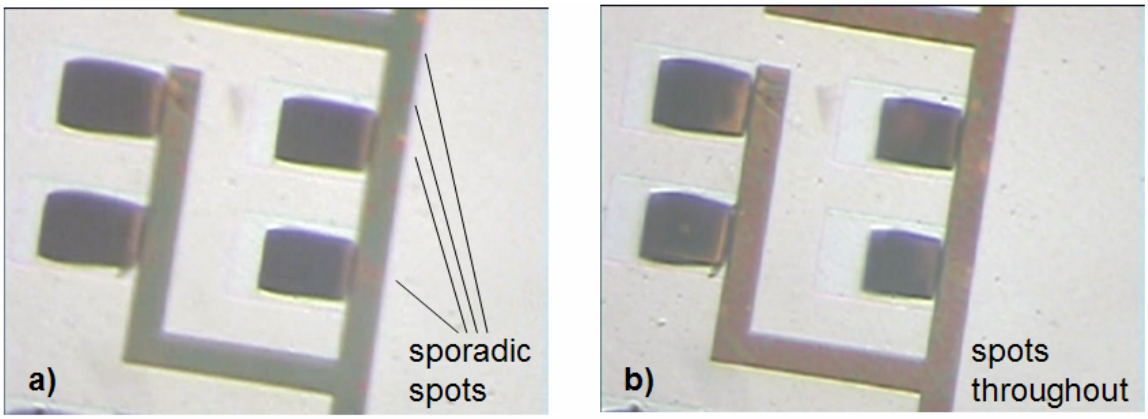

Figure 42. The appearance of spots was associated with a lessening of bilayer bending performance. The red spots would form, and with each successive cycle become larger in diameter. These spots were 'dead' spots in which oxidation and reduction did not take place. Both photos were taken at -0.8 V (a) after 3 cycles and (b) after 30 cycles.

Delamination is of great concern for every type of actuator contained within this thesis. A solution to this problem is needed. Several methods were explored by Y. Liu, including roughening the gold surface. This was accomplished in one of two ways: electroplating or etching. The thickness of the rough layer is quite important. Some type of adhesion promotion will need to be applied to any future PPy/Au bilayer actuator, especially for those applications in a body environment. It would seem that urine accelerates the delamination process, especially at elevated temperatures.

There may be some charged matter in the urine that may be attracted to the surface of the polymer during the electrochemical processes. This may cause a build-up of materials on the surface of the polymer. Anything blocking the surface of PPy will impede ion transport, which is required for switching.

Attempts were made to isolate what constituent in the urine was responsible for the adverse effects on the PPy. Urine is comprised of many things. An example of constituent concentrations from an example batch of urine can be seen in Table 2 [33].

Table 2. Approximate urine constituent values [33].

Analyte	Value	Units	Valence
Amylase	75	Units/L	
Calcium	1.7	mM	+2
Chloride	115	mM	-1
Creatinine	6.5	mM	
Glucose	2.75	mM	
Magnesium	3.4	mM	+2
Phosphorous	7.75	mM	
Potassium	36	mM	+1
Sodium	95	mM	+1
Total Protein	0.2	g/L	
Urea Nitrogen	150	mM	
Uric Acid	0.3	mM	

From this table an approximation can be made of the total ionic strength in urine. Using the standard ionic strength (I) formula [34] as shown in equation (5), with the molarity (m) and charge number of each ion (z) from Table 2, the ionic strength is calculated. The ionic strength is 0.133 mol/L. The various proteins are of unknown charge. Amylase is large a complex enzyme.

$$I = \frac{1}{2}\sum_i m_i z_i^{\,2} \tag{5}$$

A test was conducted with urea to see if that was a problem constituent. The first step was to mix a testing solution. This was done by mixing a concentration of 0.15 M of uric acid into the 0.1 M NaDBS solution used for the standard experimentations. The behavior within the NaDBS solution was known so this was a logical testing solution.

Using this solution, an experiment was done in the same manner as those shown in Figure 31. A 5:1 thickness ratio sample (with 1000 Å Au) was chosen. The sample was cycled at room temperature and then brought up to 45 ºC and cycled. The curvature changed from 0.18 1/μm at room temperature to 0.39 1/μm at 45 ºC. This curvature increase was the same as those in the temperature tests conducted in the 0.1 M NaDBS alone that can be seen in Figure 35 and Figure 36. This was unlike the temperature tests within the standard urine, in which the sample bending decreased by a sizable amount. Therefore this constituent alone is not the component responsible for the adverse effects on PPy, since behavior with urea present in the 0.1 M NaDBS solution was the same as that of the 0.1 M NaDBS solution alone.

Protein-free urine was also obtained from Quantimetrix to ascertain the roles of protein on the bending performance. Testing was done within this solution at elevated temperature. It was found that actuator degradation occurred at an even more accelerated rate than standard urine. The sample was cycled at 30 ºC, and spots like those seen in Figure 42 became quite apparent. Bending became so minimal it could barely be noticed. The process during which the protein was removed from the urine may be responsible for this. Quantimetrix shifts the pH of the urine using chemicals to remove the proteins, which may alter the urine as they are not completely removed. The pH of the urine is brought back to neutral before shipping.

A literature search determined how much of a role ionic concentration plays in the performance of PPy(DBS) [35,36]. This was done to see if the different ionic

concentration present in urine could explain the observed effects. In particular, others have done research in an electrolyte solution containing NaCl, which is the predominant component of urine [35]. Peak positions of PPy (DBS) shift with varying ionic concentration. The main reductive peak shifts from -0.4 V vs. Ag/AgCl at a concentration of 0.001 M to -0.15 V at a concentration of 1 M. The main oxidative peak shifts from -0.1 V at a concentration of 0.001 M to -0.2 V at a concentration of 1 M. This shows the shift to be small over concentration changes of many orders of magnitude. The small shift rules out the possibility that the oxidation and reduction of the PPy did not fully take place. In addition, the voltage range in my work was chosen by initially running the samples in urine over a larger range (0.1 V to -1 V) than the one finally used (0 V to -0.8 V) to determine the locations of the oxidation and reduction peaks, ensuring their inclusion in the operational voltage range. CV's of PPy(DBS) in urine can be seen in Figure 39 and Figure 40.

Future work should explore if applying a slight positive voltage could expel any unwanted material build-up from the surface that may be accumulated biological fluids. If the matter on the surface is indeed charged, this may prevent its build-up.

3.5 Force Measurements

Full characterization of PPy/Au actuators also needed to include how design parameters affect the force output of the actuator. As mentioned previously, the microvalves need to open against a considerable static pressure and hold open during fluid flow.

3.5.1 Previous Method – Weights

Initial work was conducted by Mr. Oh using a series of physical weights to gage actuator output force [3]. This method involved placing glass weights onto Kapton substrate actuator flaps prior to an actuation cycle. Weights were increased until the actuator could not lift the weights any more, thus determining the maximum force output [22].

This method provided an initial range for the force output. Exact values were unattainable for two reasons. Firstly, the weights were a fixed value of 0.52 mg each, so the measurement resolution was bound by this. Secondly, the weights tended to shift and lie partially on the surrounding surface, leading to a component of the weight being supported by the substrate.

3.5.2 New Method – Force Transducer

An approach using a force transducer (Aurora 406A), which had a higher resolution and lower error, was later developed as a result of work conducted by Mr. Furst, Mr. Liu, Dr. Christophersen, and myself. This was used to measure the force exerted by the actuators fabricated upon the surface of the silicon substrate. Actuators were measured that bent to a position of 180° in the oxidized state. The transducer head was positioned over the flap's back side while the bilayer was in the oxidized state. Upon reduction, the back of the plate touched the transducer when the hinge tried to straighten. These data were easier to collect, since in the reduced states, the hinges did not lie at 0°. Future work should measure flaps starting in the reduced position for comparison.

The force transducer head contains a capacitor with one movable plate, to which a glass tube is attached. This capacitor detects changes in the movable plate position, which can be related to force by calibration. A tungsten wire was affixed within the glass tube using paraffin wax, and it protruded from the end of the glass tube, allowing for outside sample contact. The tungsten wire was electrochemically sharpened by Changyi Li using a process for scanning tunneling microscopy tip sharpening [37]. These sharpened tips allowed for increased placement accuracy on the backs of the flaps over tungsten wire cut with wire cutters. The sharpened tip was approximately 10 μm in diameter.

The tip of the sharpened tungsten wire was placed on the center of the back of the flap. The observation of the flaps and positioning was facilitated by a Leica Z16 microscope positioned at a slightly angled view. Once contact was observed, the wire was backed off to just above the flap surface. These fine position adjustments were accomplished using a three axis micro-positioning system (Newport Optics), to which the force transducer was affixed. The attachment device affixing the force transducer to the positioner, as well as the apparatus affixing the positioner to the optical table, were machined from acrylic by Mr. Furst. The entire apparatus was placed over a two-axis microscope stage, which allowed for the coarse adjustments, as well as movement from flap to flap.

A series of measurements was conducted for each thickness ratio. The surface micromachined samples had identical hinge lengths grouped into sets of four. Measurements involved at least three of these groups from adjacent rows, all with identical hinge lengths, for a minimum of twelve individual measurements. These

measurements were averaged and the standard deviation calculated. The measurements taken by both Mr. Liu and myself can be seen in Figure 43 and Figure 44. Averages were calculated by taking the raw data and determining the slope of the rest position at the beginning and at the end. These values were used to level the data. The average was then taken of the flat portion of the measured force. This average force value had the average rest value subtracted from it to obtain the change in output voltage from the force transducer. The voltage value was converted to a force value using a conversion factor dictated by the calibration of the device.

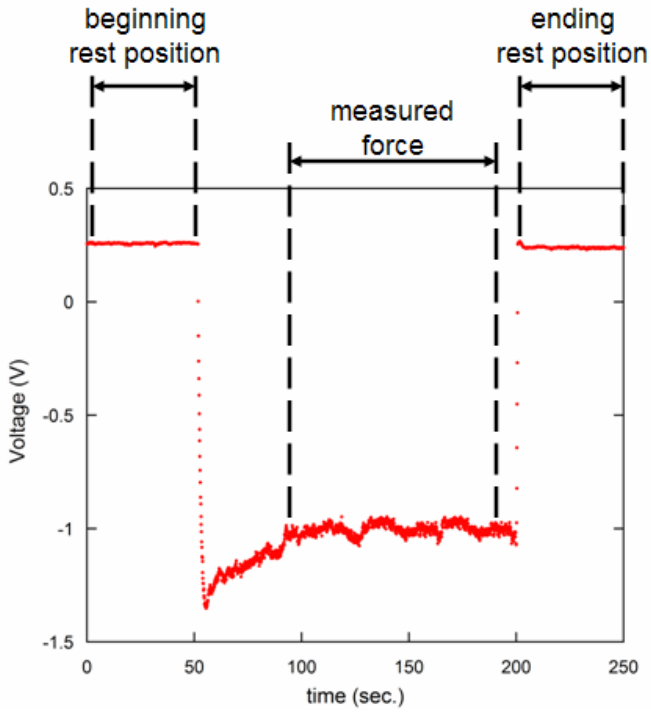

Figure 43. Example raw data from the force transducer showing the beginning and ending rest positions

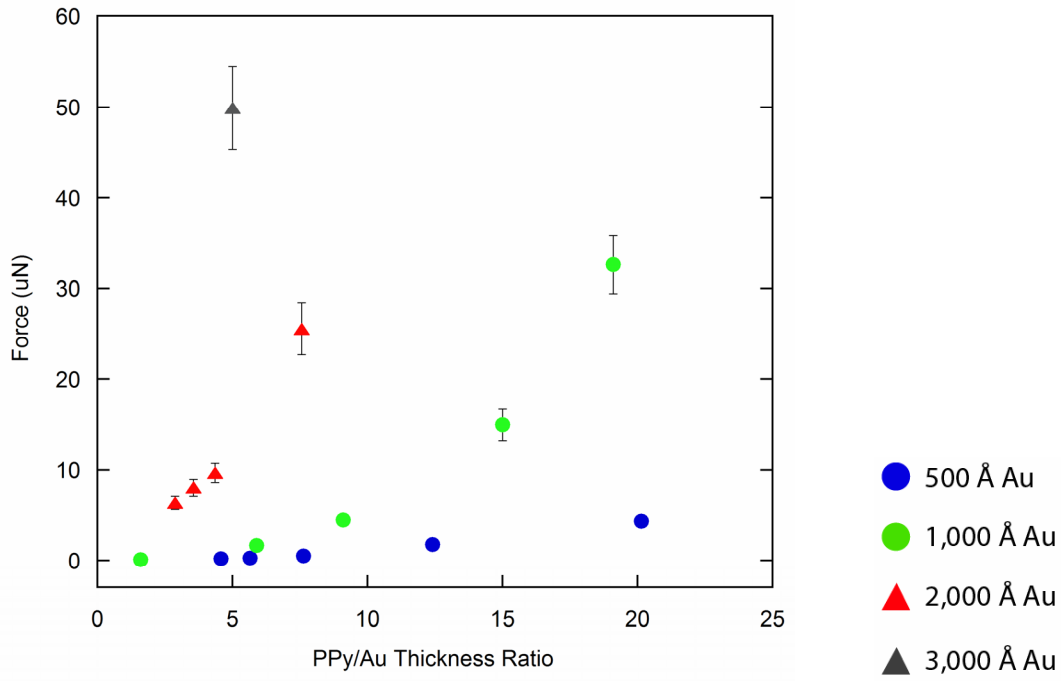

Figure 44. Plot showing the output force as a function of the PPy/Au thickness ratio, all with 400 µm hinge lengths.

As a result of the new measurement technique that was developed, reproducible and accurate force measurements are now possible on micro-scale PPy/Au bilayer actuators. Figure 44 provides information over the entire range of Au thicknesses deemed reasonable by the curvature experiments. The information displayed in Figure 44 can be used in conjunction with the information about bending performance to optimize the design of any future actuator using PPy/Au bilayers. For applications requiring large force, for example, the 500 Å Au devices cannot be used: thicker Au layers are required (Figure 44), or the hinges need to be made wider.

To use the device described at the end of Chapter 2 in vivo, the device would need to satisfy certain force requirements. The typical human female urethral diameter is 6 mm.

The hole diameter used in this example sample was 500 μm. To have the same area through which the urine was to flow, there would need to be 36 holes arrayed on the incontinence controller.

The pressure at the end of the urethra varies over a range of approximately 10 cm of water to 110 cm of water [3]. The maximum pressure translates to 8.7 mN of force on a 900 μm x 900 μm flap. This would need to be overcome in order for the actuator to open. From Figure 44 it can be seen that a 400 μm wide hinge with 2000Å Au and a 5:1 thickness ratio produces a 10 μN force. Since this means that the device would need to be 870 times longer than 400 μm, the square flap device geometry would not work. A louver type of design would be a good place to start, meaning increasing the hinge width and decreasing the flap length and therefore the flap area. Higher thickness ratios and a thicker Au film would also undoubtedly need to be used to make a working actuator for this type of project.

Future work should begin with gathering a full 3000 Å Au force curve. The design of the samples surface machined on the silicon surface made this impossible due to the small curvature of the 3000 Å Au samples. Longer hinge lengths are needed to increase bending angle to 180º. The next step should involve temperature studies of bilayer output force. The technique developed for gathering force data in this thesis would be just as useful in the testing of temperature effects on force. These tests should be conducted in a similar manner as the curvature temperature experiments. A fresh sample should be used for each different temperature measured.

Other work that should take place are measurements of flap force bending from the reduced state to the oxidized state. This would then provide a complete picture of the force the bilayers are capable of in both directions. This information would be of particular use to applications similar to the urinary incontinence microvalve. The force to open the valve against the static urine is obtained by going from the reduced to oxidized state, in the opposite direction to what was measured here.

3.6 Sealing Tests

3.6.1 Leakage Tests in Lab

Assembled microvalves needed testing to determine their sealing capabilities. Initially, actuators glued to a transparency sheet seat with a drilled hole, as seen in Figure 20, were tested. A schematic description of these valves is shown in Figure 45.

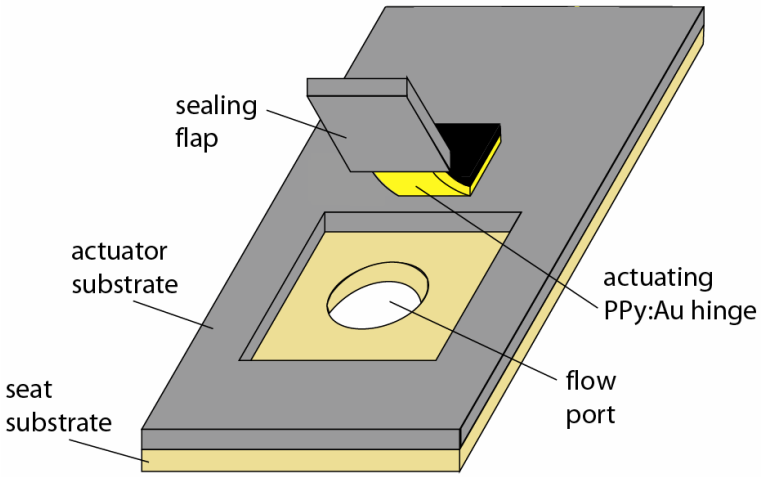

Figure 45. Schematic of the initial valve, in which the actuator is glued to the top of a seat substrate.

To test the sealing capability of the microvalves, a leakage testing apparatus was needed. As nothing like this was commercially available, an apparatus was designed and created, which was quite challenging. First, an overall three-part design was decided upon by Mr. Furst and myself. This consisted of an electrolyte containment tube with a flange, a flange mate bottom with a through-hole allowing for flow, and a small sample clamp. These three components can be seen in parts a, b, and c of Figure 46. All components were machined from acrylic. A flange was chemically fused, using methylene chloride, onto the electrolyte containment tube to create the first part.

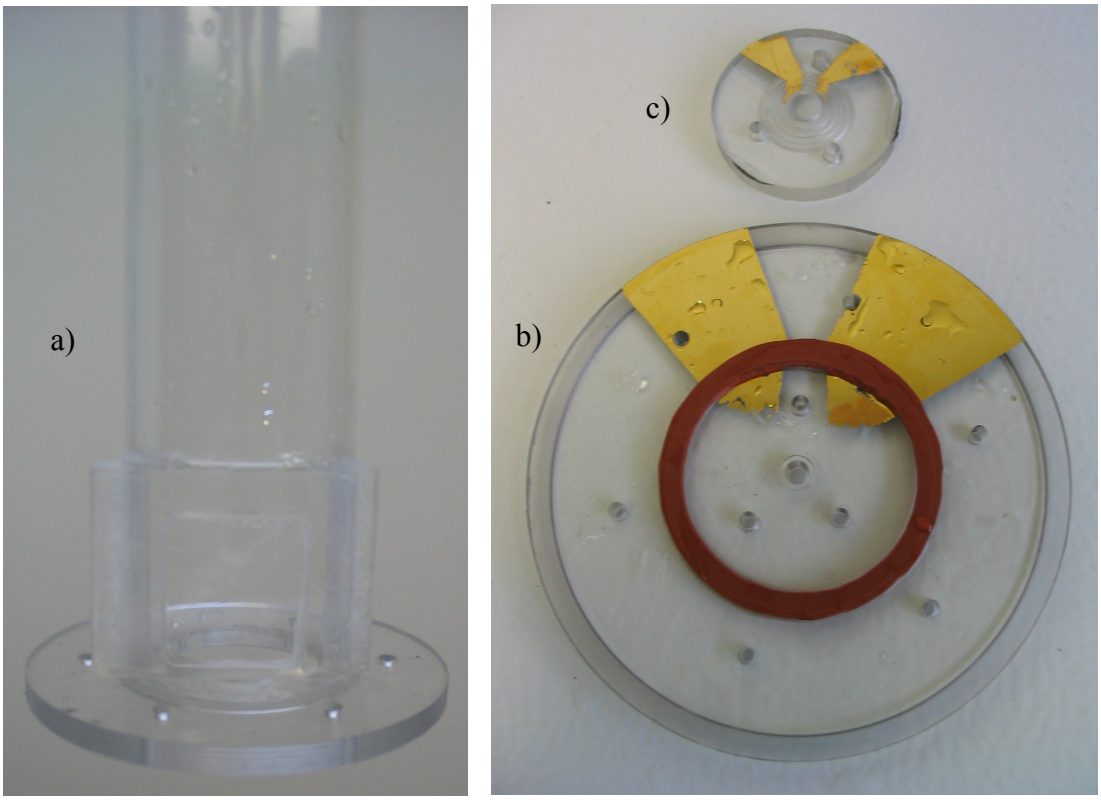

Figure 46. Leakage testing apparatus composed of three pieces: a) electrolyte containment tube with flange, b) flange mate bottom with through hole, and c) sample clamp with electrical contacts.

Secondly, a reliable electrical connection from outside of the sealed device to the sample within needed to be incorporated. The connection method employed was pressure contacts. This was accomplished by evaporating Cr/Au on two of the machined acrylic parts, the top of the flange mate bottom and the bottom of the small sample clamp. Some portions were taped off, which defined the pattern of the electrodes once the tape was peeled away. The electrical path followed the top of the two sample electrodes touched by the bottom of the patterned sample clamp, which further out touched the top of the flange mate. The top of the flange mate bottom was larger than the piece above it, allowing for the two electrical contacts to be made here with clamps. The three components of the leakage testing apparatus can be seen assembled in Figure 47. Fabrication and assembly were conducted by Mr. Furst and myself.

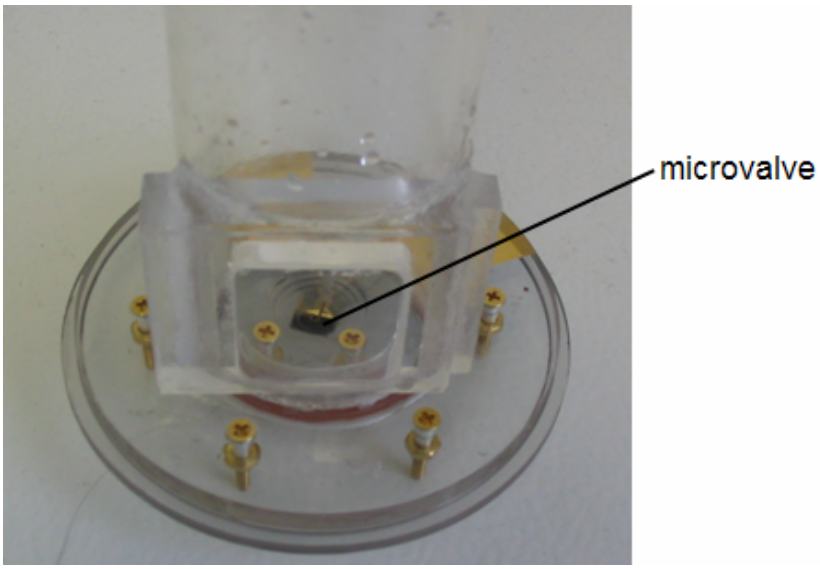

Figure 47. Fully assembled leakage testing apparatus with inserted microvalve sample.

Once the tube was filled with electrolyte, 0.1 M NaDBS, the cloudiness of the solution combined with the curvature of the tube made seeing the valve in the bottom center impossible. A portion of the tube towards the bottom was removed to allow for installation of a thin flat acrylic window. This window helped to allow observation of the valve during testing. The improved viewing capability can be seen in Figure 48. It should also be noted that focusing on the flap with the microscope needed to take place after the NaDBS was added, as a result of the index of refraction differences between air and the liquid.

Figure 48. Photo showing the improved observation allowed by the flat window installed in the sealing testing apparatus.

Sealing between all testing apparatus components was of great concern. Complete sealing was accomplished by the application of two different methods. The first method was the implementation of o-rings. Large o-rings were cut from a rubber sheet with exact-o blades, and are the red rings seen in Figure 46. These large o-rings were placed between flanges to inhibit leakage. Smaller o-rings were cut from the same material to lie beneath each screw head, which held the sample clamp circle down. The second

method was to apply silicone around the installed window. This was done because the chemical bonding was insufficient.

Once the apparatus was assembled and sealed, a two-electrode sample with an attached seat was inserted. This was done by placing the sample over the corresponding electrical contacts in the leakage testing device and securing it down with the machined sample clamp. A small amount of 0.1 M NaDBS solution was placed in the tube above the valve. The bottom of the apparatus was placed within a container of NaDBS. This was done so the valve would be submerged in the electrolyte and no leakage would take place at that initial stage. The sample was then put through a 'rewetting' session. This consisted of cycling the sample between the redox limits ten times. The apparatus was taken out of the NaDBS container for leakage testing. More NaDBS solution was poured into the tube above the valve. The bottom of the apparatus was dried and held at 0 V, the open position. A steady flow of NaDBS was seen flowing from the back of the valve in this state, as expected. Next, the valve was switched to the reduced state and held. The overall flow decreased, but the valve failed to seal.

As a result of the sealing failure of the samples with no gasket, the microvalves that had the gel o-rings fabricated on the seat were tested. Better sealing was anticipated. The same rewetting process was conducted as the valves without the gel o-rings. Following this preparation, initial flow in the open position was observed as with the samples without the gel rings. Next, the reduced state (the closed position) was tested for sealing capability. The bottom of the apparatus was dried with paper towels, and no leakage was

observed. The valves with gaskets successfully prevented flow in the closed position. As a final test, the valve was oxidized once again in an attempt to open the valve against the pressure provided by the electrolyte holding tube. Unfortunately, the valve remained sealed regardless of the amount of NaDBS over the flap.

Overall, the leakage tests were a success. The valve sealed when closed in a flow. Unfortunately the valve did not open again against the flow. The valve should be optimized to overcome the pulldown force using the bending and force data presented in this thesis. Further investigation should be done to determine the best shape of the flap, as well.

Eventually these microvalves would need to be fabricated using only microprocessing techniques. Therefore, the means by which the seats were created and affixed to the actuators would be unacceptable for production. The RIE method of drilling holes into the seat would be a logical next step towards microvalve development, since it could be a batch fabrication step. Affixing the samples would need to take advantage of the UV patternable nature of the Loctite. There were issues with patterning the Loctite for initial testing however. Loctite that is not crosslinked during exposure is not easily removed. Typically acetone is used within the lab for removal, but this affects the PPy. Loctite manufactures a large number of UV patternable products, and more of those should be investigated for use in microvalve fabrication.

3.6.2 Pig Leakage Tests

Once initial leakage testing was completed, a more realistic bodily environment test was conducted. Gary Barrett of IBT arranged a live pig test, which was conducted on a sedated pig. A catheter was inserted into the urethra of the pig. This catheter tube was kept long, so it would hang outside the body. This allowed an assembly containing a single microvalve to be attached to the end of the catheter.

IBT's approach to valve testing was to wire-bond metal wires to the two electrodes on the microvalve. This would allow the contacts to be reached from outside a silicone casing. The valve was to be inserted vertically into the center of a mold, which can be seen in Figure 49, designed to create the silicone casing around the microvalve.

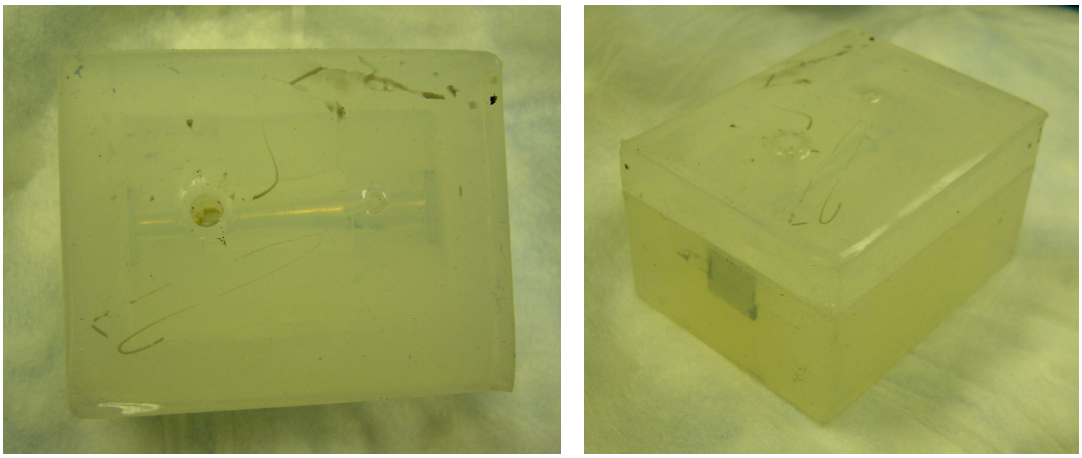

Figure 49. For rapid incorporation of valves into a silicone casing. These encased valves were attached to the end of a catheter inserted into the pig. (The mold was designed and fabricated by Mr. Barrett at the Albany Nanotech Center.)

Two machined metal rods would be butted up against either side of the microvalve's center hole to prevent silicone from setting near the actuator itself. Any silicone touching

the actuating valve would have interfered with operation. The top of the mold would be attached, and quick setting silicone injected into the mold. A finished set microvalve and casing can be seen in Figure 50. The mold was flexible enough to peel back away from the casing and reused.

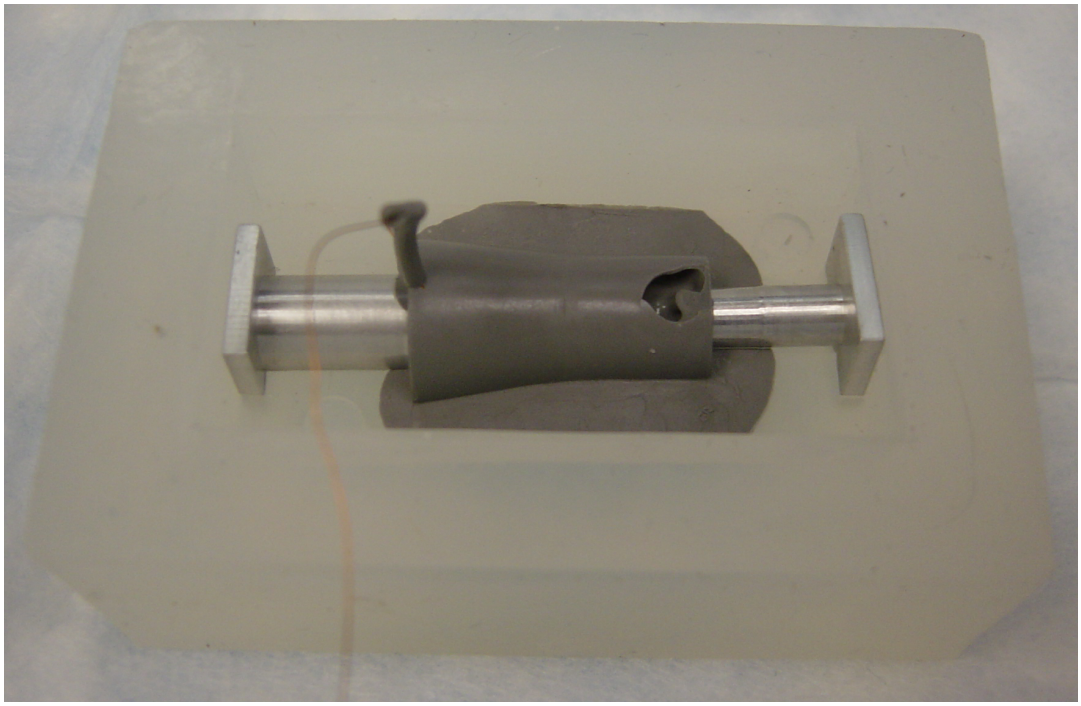

Figure 50. Molded silicone casing (gray) around a louver microvalve (fabricated by Yogesh Ekanath Kashte at Georgetown University). Note the two machined metal plugs pressed against either side of the louver valve. These plugs assured the absence of silicone on either side of the microvalve, so flow could pass through the casing if the valve was opened.

The silicone casing acted as an adapter, allowing for simple valve attachment to the end of the catheter. A schematic of the casing, valve, and catheter tubing can be seen in Figure 51.

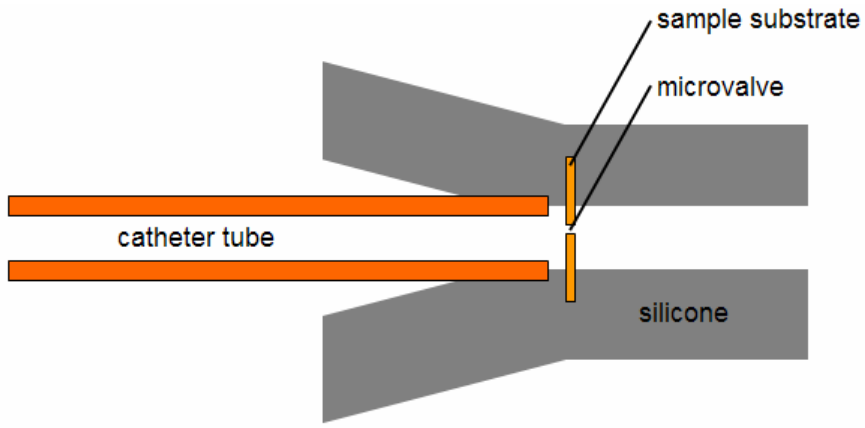

Figure 51. Schematic of an adapter assembly, which allowed a microvalve to be attached to a catheter for leakage tests.

The mold assembly was originally designed for use with a set of louver type microvalves used by IBT. This made incorporation of my two-electrode valves difficult due to the size difference of the two samples. The silicone needed to connect to itself on both sides of the device so it could bond. The two electrode square samples had a larger surface area, which stuck out on all sides of the silicone casing. This did not allow the valve to be completely encased by the mold. Just prior to the valve testing using the pig, I improvised a method to attach the two electrode devices and allow for leakage testing to take place. The front half of a silicone casing was glued to the microvalve and seat using the UV curable glue used to attach the seats to the actuator substrate (Figure 52).

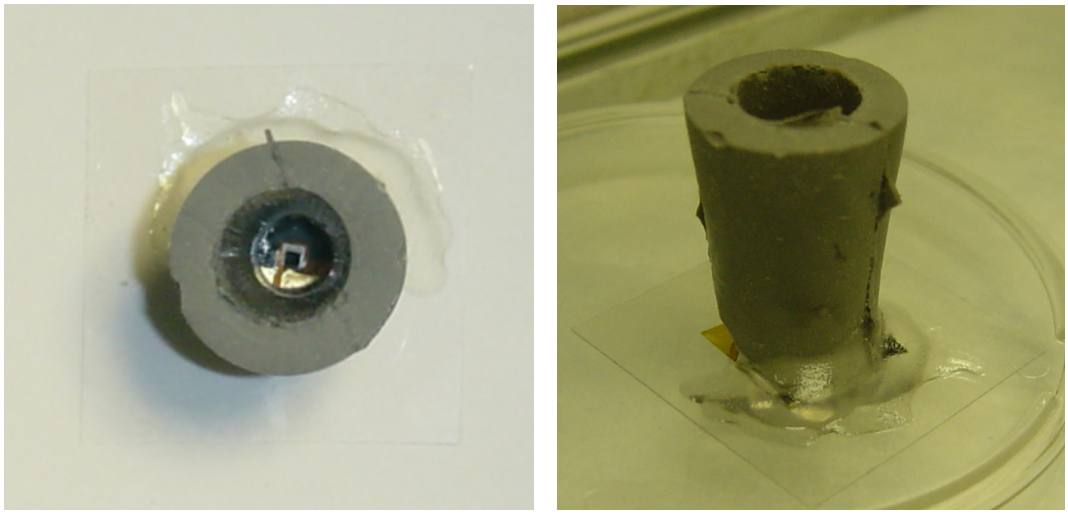

Figure 52. Microvalve with attached seat and gel ring attached to silicone catheter adapter using Loctite 3108.

For the actual pig test, the microvalve, with a and gel ring, in its casing was pressed onto the end of the catheter. The catheter was pinched off to prevent urine flow at this point. The working and counter electrodes were hooked up to the potentiostat with clips as seen in Figure 53. The valve was put through a 'rewetting' session in which it was cycled in a container of urine before the catheter was opened.

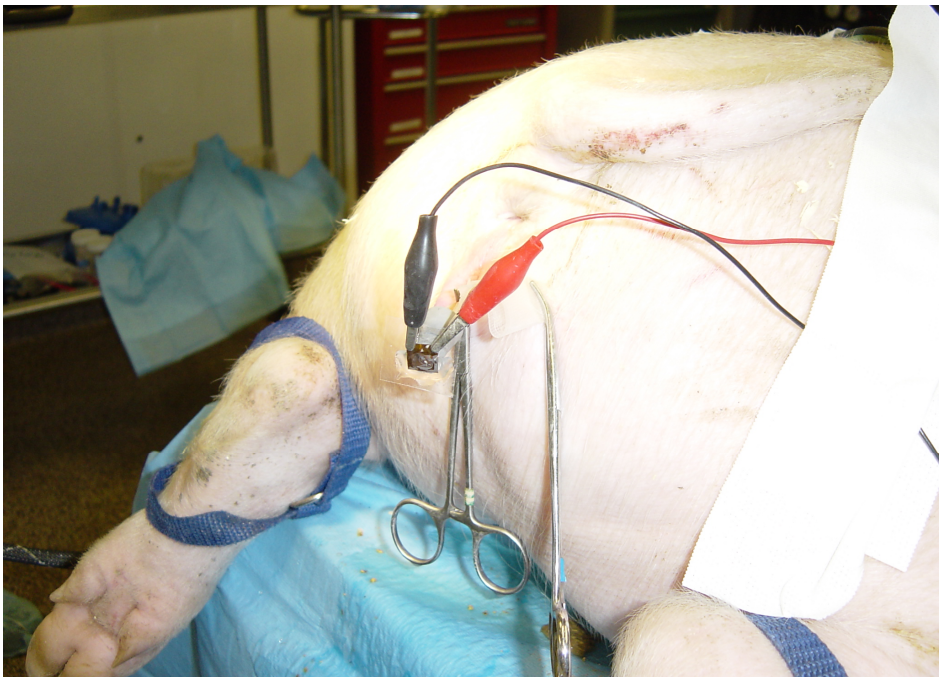

Figure 53. Live animal testing with microvalve attached to catheter through use of molded adapter.

The catheter was opened and urine was observed leaking through the valve hole. The urine was flowing in a steady small stream dripping from the bottom of the back of the valve sample. The actuator was electrochemically reduced in an attempt to close and seal the valve. Once the device was closed, the urine was wiped from the back. No further beading formed. Therefore, complete sealing of the valve was observed. This proved that the device could in fact work for at least one cycle in an environment using urine as the electrolyte.

The next test was to attempt to open the valve against the pressure of the bladder. There continued to be an absence of urine flow, showing the valve remained sealed. The valve could not open against the pressure of the bladder. It should be noted that the bladder pressure was earlier increased in order to get a steady high flow of urine in the open

catheter state. This was done by injecting urine, taken from the pig over several hours, back into the pig's bladder through the catheter. The urine had been stored in a warmer at body temperature. As a secondary test, the catheter was pinched off to attempt opening the valve in static urine. At this point, urine flow was seen dripping out of the back of the valve. The valve successfully opened against the static urine that did not have the full pressure of the bladder behind it.

The pig test can be considered an initial success for a first live animal test. The valve successfully closed with an over-pressurized bladder and sealed perfectly in the path of the urine flow. The valve also opened in the static urine, but unfortunately, not in the path of the full urine flow. This behavior is consistent with the force analysis discussed in section 3.5.2.

Chapter 4 Conclusions

A valuable set of data has been collected to aid in the development of PPy/Au actuators. Using the material collected in this thesis, bending and force requirements can be translated into required geometric parameters.

Future work should be conducted on the promising titanium substrate samples. A series of tests should be done on PPy alone to determine if there is a step in the fabrication sequence that damages it. Once the step is isolated, a potential replacement step should be investigated. The ability to fabricate titanium substrate MEMS is now possible, but being able to use the PPy/Au bilayers, as was the original intent of this thesis, would be useful.

A previously unknown temperature effect has also been discovered in these actuators. It would seem that actuation strain in PPy(DBS) increases dramatically at 40 ºC in NaDBS. Quite interestingly, raising the temperature within urine seems to have an opposite effect, which may be a potential stopping point for the urinary incontinence project. Further investigation needs to be conducted to determine its cause and at what exact temperatures it takes place. This can be done by following the testing methods laid out in this thesis. A new sample should be used at each temperature.

Once bending within urine is fully understood, force measurements should be conducted in urine at room temperature. If there is a range above room temperature in which the bilayers operate, the fore should also be tested there.

Successful sealing of assembled microvalves was very important in proving that a PPy/Au microvalve can work, although it may not work in urine as was its original intent. Future work should be done to make the fabrication sequence a batch fabrication process. The seat in particular is labor intensive, as is the attachment of the seat to the actuator. If the devices were shrunk down, the fabrication and assembly method used here would be quite difficult. The implementation of an RIE etch to create holes within a substrate, especially for future arrays, is needed. Different types of Loctite should be investigated to ease attachment of the seat to the actuator without adversely affecting the PPy.

Appendix A

The attached conference paper "Fabrication of folding microstuctures actuated by polypyrrole/gold bilayer" was presented by Y. Liu with S. Fanning as a contributing author at the IEEE International Conference on Solid State Sensors, Actuators, and Microsystems, Transducers, in Boston, MA, 8-12 June, 2003. It appears on pages 786 to 789 of volume 1.

FABRICATION OF FOLDING MICROSTRUCTURES ACTUATED BY POLYPYRROLE/GOLD BILAYER

Yingkai Liu[a], Lance Oh[a], Steve Fanning[a], Benjamin Shapiro[b], and Elisabeth Smela[a]
Department of Mechanical Engineering[a] and Aerospace Engineering[b]
University of Maryland, College Park, MD 20742, USA
Tel.: (301) 405-5265, Fax: (301) 314-9477, e-mail: smela@eng.umd.edu

ABSTRACT

We have developed a method to fabricate substrates that can fold themselves. The microstructures are actuated by an electroactive polymer, polypyrrole (PPy). A series of bilayers is defined on one surface of the substrate, and hinges are formed by etching the substrate from the back side to undercut the bilayers. A shape-morphing object is demonstrated that comprises multiple hinges. This object was able to bend both forward and backward. We are applying this technology to fabricate medical devices that operate in bio-fluids.

INTRODUCTION

Researchers have shown increasing interest in forming 3-dimensional structures at the micron scale since the early 1990s. Because standard microfabrication procedures produce inherently 2-dimensional structures, these must be folded to achieve 3-D objects. Various methods have been demonstrated to accomplish this. For example, Pister et al. rotated polysilicon components out of the plane of the substrate on surface micromachined pin-in-staple hinges to assembly a micro-mirror [1]. Brittain et al. patterned metal layers by microcontact printing, and then folded the layers along pre-designed hinges to make micro-origami figures, including a bird [2]. The folding step, however, has typically been realized manually at a probe station. It is time-consuming, and the tiny structures are easily broken by the operation. Thus, it is important to automate the folding.

Different approaches to automatic folding have been demonstrated based on mechanisms that include surface tension forces (using molten solder) [3], thermal expansion [4], and the residual stress of lattice mismatch [5]. These methods are "one-way" procedures: the components cannot go back to their original positions once they are actuated. Reversible folding has been achieved using electrostatic fields [6], magnetic fields [7], and shape memory alloys [8], to name just a few. Based on these techniques, microactuators have been exploited to achieve assembly of microstructures.

Another reason for developing components that can bend out of plane is for actuation. Ideally, microactuators should be robust, produce relatively large displacements, exert sufficient force, and hold fixed positions. A large number of out-of-plane bending technologies have been developed. One of these was our polypyrrole (PPy) bilayer hinge [9,10]. PPy changes volume under electrochemical stimulation when it is immersed in a salt-containing solution (electrolyte). Applied potentials change the number of electrons on the PPy backbone, and to maintain charge neutrality, ions enter and leave the film, producing an in-plane actuation strain on the order of a few percent. The second component of the bilayer is a metal film that serves not only as the electrode, but also to convert the strain in the PPy to bending. The concept is essentially the same as that of a thermal bilayer. In prior work, we have shown that such bilayers can rotate rigid plates with working electrical devices [11] out of the plane of the wafer.

In this paper, we report an extension of the PPy bilayer technology to 1. fold an entire substrate and 2. use polymer substrates such as Kapton instead of silicon. We are developing methods to make self-folding origami; reconfigurable 3D shapes would represent a new capability for MEMS. The ability to fabricate devices on polymer substrates could potentially lead to inexpensive, mass-produced MEMS made by roll-to-roll fabrication processes. In addition, this technology has a number of biomedical applications because PPy actuators operate in body fluids and require only low voltages (typically 1 V or less) [12], and the Kapton has excellent chemical resistance [13]. For example, we are collaborating with Infinite Biomedical Technologies to use this technology to develop a micro-valve to control the flow of fluids in the human body. The basic Kapton hinge concept is shown in Figure 1.

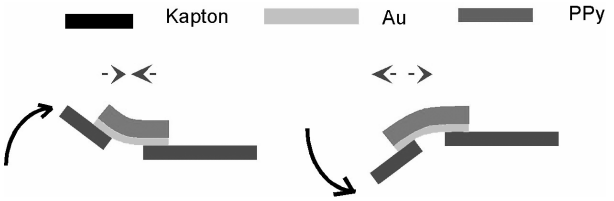

Figure 1. PPy/gold hinge to fold the Kapton substrate.

EXPERIMENTAL

In order to obtain working devices, the fabrication processes were critical. Therefore, we will describe the fabrication methods in some detail.

Process Development. The fabrication process is conceptually simple; it entailed deposition and patterning of a metal layer, deposition and patterning of the PPy, and etching through the substrate, as illustrated in Figure 3. To achieve this, however, careful attention had to be paid to each step, particularly to the interfaces.

Kapton sheets (HN200, 50 μm thick, DuPont Co.) approximately 5×5 cm^2 were carefully cleaned before use with acetone, methanol, isopropanol, and deionized (DI)

water; surface contamination prevented the deposited metals from adhering. An adhesion layer of chrome was either e-beam or thermally evaporated (10 nm, 0.3 nm/sec, $<5\times10^{-6}$ Torr) onto one side, referred to as the front side. A thick layer of chrome was used because the Kapton surface was rough (~60 nm peak to peak). The chrome layer was indispensable: without it the electrodes delaminated during actuation.

A layer of gold was evaporated next without breaking the vacuum (~200 nm, 0.5 nm/sec, $<5\times10^{-6}$ Torr). It is necessary that the electrodes be electrochemically inert; either gold or platinum can be used. The gold was patterned by photolithography and wet etching (gold etchant, Transene), and then the chrome was etched (chrome etchant, Transene) (Figure 3a). After the photoresist was stripped, surface residues left by the chrome etching step were removed in freshly mixed piranha etchant (1 part sulfuric acid, 1 part hydrogen peroxide, and 5 parts water). This was necessary to prevent PPy from electrodepositing laterally over the entire Kapton surface instead of just on the electrodes.

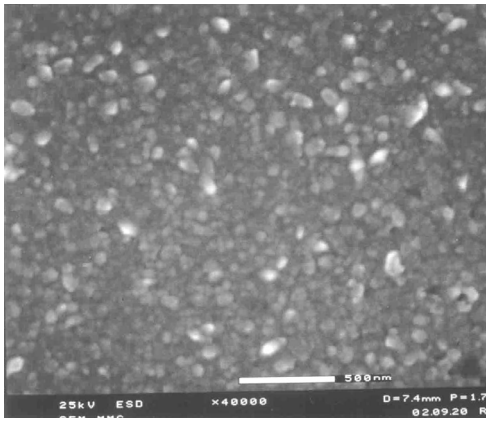

Figure 2. SEM micrograph of a 50 nm thick electroplated layer; nodules increase in size with thickness.

To prevent delamination between the PPy and gold layers during later actuation, we electroplated a rough layer of gold over the thermally evaporated metal (Figure 2). This results in mechanically interlocking the layers [14]. We electroplated at –0.9 V (vs. Ag/AgCl) using a solution of Oromerse SO part B diluted 1:10 with 1.7 M Na_2SO_3. The sample was immersed into this solution, except for the contact pads, and connected to a potentiostat (EcoChemie Autolab). A 150 nm thick layer was deposited in 2 minutes (Figure 3b). The sample was rinsed with DI water.

The pyrrole monomer (Aldrich, stored at –40 °C) was purified by passing it through aluminum oxide. An aqueous solution of 0.1 M pyrrole and 0.1 M sodium dodecylbenzene sulfonate (NaDBS, Sigma) in DI water was freshly mixed. (PPy can be grown in various electrolytes, but NaDBS results in very good actuators [15].) The PPy film was electrochemically deposited onto the gold by applying 0.5 V (vs. Ag/AgCl) until the desired thickness was deposited. (Figure 3c; see [16] for details on PPy deposition). The samples were rinsed with DI water.

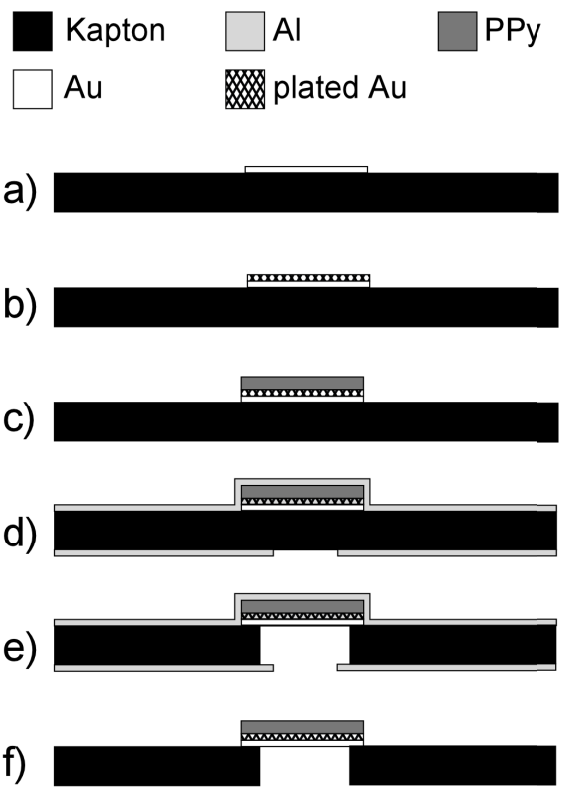

Figure 3. Process sequence for hinge formation.

Next, the aluminum for the back side etching mask was deposited. Just prior to that, the samples were rinsed in methanol and DI water to ensure Al adhesion. The Al was either e-beam or thermally evaporated (200 nm, 0.5 nm/min, $< 5\times10^{-6}$ Torr). This film was patterned photolithographically and wet etched (Al etchant, Transene). Another 200 nm Al film was deposited on the front side to protect the PPy layer during subsequent RIE etching (Figure 3d).

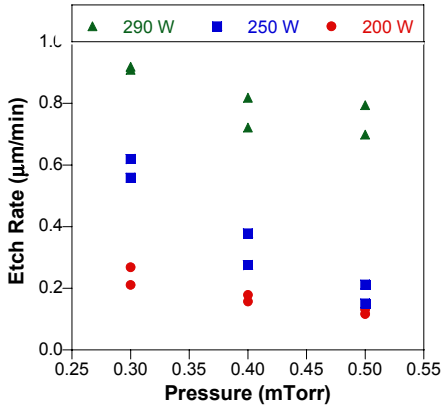

Figure 4. Kapton etch rate vs. pressure & power.

The back side of the Kapton was etched by reactive ion etching (RIE) with an oxygen plasma (March Jupiter III) to form hinges by removing the substrate beneath the bilayer (Figure 3e). The pressure and voltage during RIE were obviously important parameters. At higher O_2 pressures, the etch rate for Kapton slowed (Figure 4) and the Al was damaged; 0.2 mTorr gave good results. At 300 W and 0.2 mTorr, the Kapton etch rate was approximately 1.3 µm/min.

It was also very important that the sample remained perfectly flat on the plate in order to ensure uniform etching. The Kapton had a tendency to bow, which could result in samples catching fire during the RIE etching. The use of weights to hold down the edges of the sample was inadequate. It is best if an adhesive is used to attach the front side of the sample to another substrate, such as glass; we are working to perfect this method.

The last step was to remove the aluminum (Al etch, Transene) from both sides, completing the devices (Figure 3f).

Actuation. The devices were immersed in an aqueous electrolyte (0.1 M NaDBS) and connected to a potentiostat. A voltage cycle (from 0 V to –1 V vs. Ag/AgCl, ramp rate 0.02 V/s) was applied to the device. Upon reduction, the PPy expanded, causing the hinges to bend backwards, and upon oxidation the PPy contracted, bending the hinges forward. Fixed potentials between 0 and –1 V can be used to hold the device in particular positions (Figure 5).

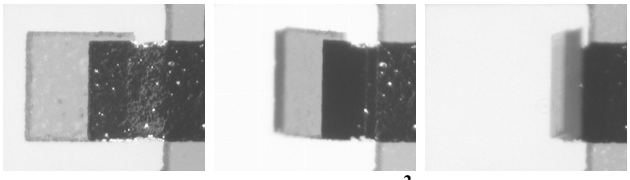

Figure 5. Kapton plate 430×430 μm^2 at 0°, 45°, and 90°.

RESULTS AND DISCUSSION

The PPy is electrodeposited in the oxidized state. When it is electrochemically reduced (-1 V), cations (Na^+) enter the film, resulting in volume expansion, and when it is oxidized (0 V), the cations leave, resulting in a contraction.

Figure 6 shows a demonstration device that folds into a sphere. Each segment, 400 μm wide at the center, is actuated by 27 bilayer hinges, each 50 μm wide. Figure 6a shows the device before voltage cycling. When the PPy is oxidized, the segments bend forward (Figure 6b-d). During reduction, they bend backwards into another sphere (not shown).

In order for the PPy to be adopted by the MEMS community, the material needs to be characterized and its behavior modeled. This is not straightforward because strain, stress, and Young's modulus are functions of the applied potential (oxidation level). Furthermore, a strain gradient exists in the PPy film as a result of the electropolymerization process. We have developed simple bilayer bending and force models, and their predictions are shown in Figure 7. The two bending angle curves result from using the Young's modulus of the oxidized, 0.45 GPa, and reduced, 0.2 GPa, states of PPy(DBS) [17] and a gold film modulus of 50 GPa [18]. We are verifying these curves experimentally with angle and force measurements for samples with different PPy and gold thickness ratios. These data will allow us to refine the models.

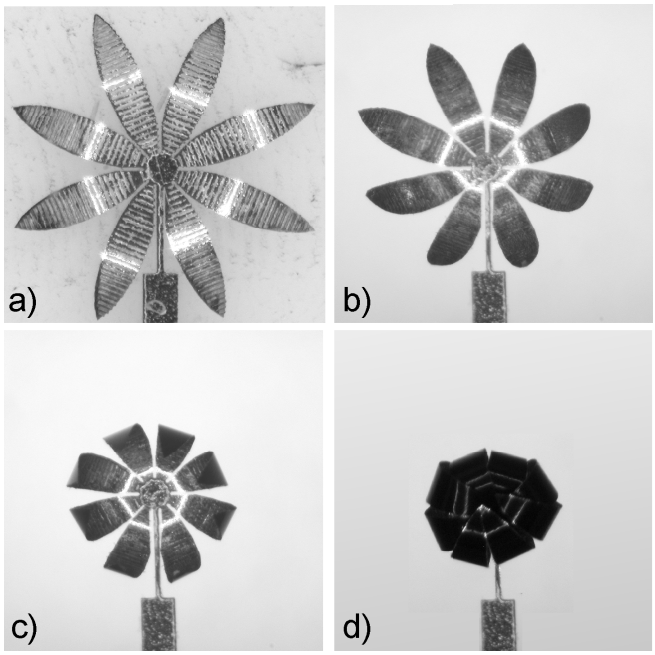

Figure 6. Multi-hinged surface folding into a sphere. The diameter of the unfolded structure is 3.5 mm.

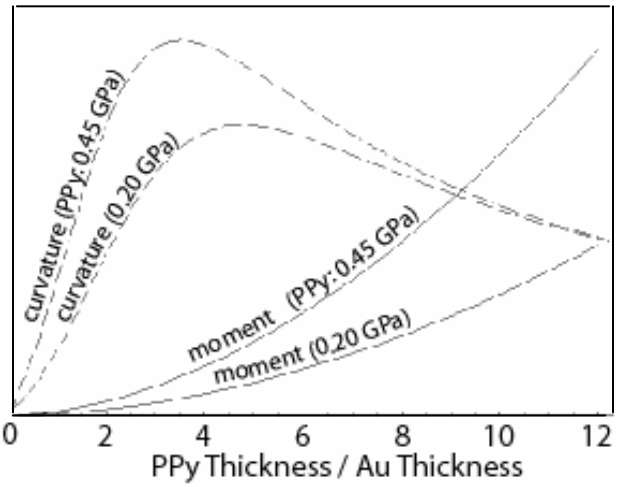

Figure 7. Predicted bending angle and moment as a function of PPy:gold thickness ratio (normalized).

The next step in this project will be to fabricate devices with hinges on both the front and back sides of the substrate. One of the challenges we have overcome was delamination of the protective aluminum on the front side over the PPy during Al etching. This was due to swelling of the PPy in the aluminum etchant, which produced cracks, holes, and peeling of the aluminum layer. Using a gold layer to replace the aluminum solved this problem. The remaining fabrication challenge is the RIE etching. Because both front and back sides of the substrate need to be etched, we must devise a method to protect the delicate, free structures during the second RIE step.

SUMMARY AND CONCLUSIONS

We have developed a microfabrication technique to create PPy/gold bilayers on polymer substrates. By

controlling the applied electrochemical potential, the substrate can be folded automatically and reversibly by the bilayers. In particular, rotating plates and a 360° curved surface have been implemented. This technique provides an approach to fold two-dimensional components to form three-dimensional, complex structures at the micron scale. The devices have potential biomedical applications due to their biocompatibility, low operational voltage, and operation in bio-fluids. Currently, we are applying the techniques reported here in the development of a microfluidic valve for use in the body. More complicated folding devices with bilayers on the both sides of the substrate are also in progress. Characterization of the bilayers and the PPy material is being performed to build models that predict device performance.

ACKNOWLEDGMENTS

This work is funded by the Minta Martin Aeronautical Research Fund and the Maryland Industrial Partnerships program, University of Maryland. We would like to thank Mr. T. Loughran of the Department of Electrical and Computer Engineering for his helpful advice and support.

REFERENCES

1. K. S. J. Pister, M. W. Judy, S. R. Burgett, and R. S. Fearing, "Microfabricated hinges", *Sens. Act. A* 33, 249-256 (1992).

2. S. T. Brittain, O. J. A. Schueller, H. Wu, S. Whitesides, and G. M. Whitesides, "Microorigami: Fabrication of small, three-dimensional, metallic structures", *J. Phys. Chem.* 105, 347-350 (2001).

3. R. R. A. Syms, "Equilibrium of hinged and hingeless structures rotated using surface tension forces", *J. Microelectromech. Syst.* 4(4), 177 -184 (1995).

4. T. Ebefors, E. Kälvesten, and G. Stemme, "New small radius joints based on thermal shrinkage of polyimide in V-grooves for robust self-assembly 3D microstructures", *J. Micromech. Microeng.* 8, 188-194 (1998).

5. P. O. Vaccaro, K. Kubota, and T. Aida, "Strain-driven self-positioning of micromachined structures", *Appl. Phys. Lett.* 78(19), 2852-2854 (2001).

6. M. J. Daneman, N. C. Tien, O. Solgaard, A. P. Pisano, K. Y. Lau, and R. S. Muller, "Linear microvibromotor for positioning optical components", *J. Microelectromech. Syst.* 5(3), 159-165 (1996).

7. I. Son and A. Lal, "A remotely actuated magnetic actuator for microsurgery with piezoresistive feedback", 2nd Annual International IEEE-EMBS Special Topic Conference on Microtechnologies in Medicine & Biology, Madison, Wisconsin, USA, 2002 p. 332-336.

8. P. Krulevitch, A. P. Lee, P. B. Ramsey, J. C. Trevino, J. Hamilton, and M. A. Northrup, "Thin film shape memory alloy microactuators", *J. Microelectromech. Syst.* 5(4), 270-282 (1996).

9. E. Smela, O. Inganäs, and I. Lundström, "Controlled folding of micrometer-size structures", *Science* 268(23 June), 1735-1738 (1995).

10. E. W. H. Jager, "Microsystems Based on Polypyrrole Microactuators: Microrobots and Cell Clinics", PhD Thesis, Department of Physics and Measurement Technology, Linköpings universitet (2001).

11. E. Smela, "A microfabricated movable electrochromic "pixel" based on polypyrrole", *Adv. Mat.* 11(16), 1343-1345 (1999).

12. E. Smela, "Conjugated polymer actuators for biomedical applications", *Adv. Mat.* 15(6), (2003).

13. D. P. Birnie, "Rational solvent selection strategies to combat striation formation during spin coating of thin films", *J. Mater. Res.* 16(4), 1145-1154 (2001).

14. C. C. Bohn, M. Pyo, S. Sadki, E. Smela, J. R. Reynolds, and A. B. Brennan, "In-situ measurement of conducting polymers on evaporated and electrochemically deposited Au surfaces", *Chem. Mater.* (accepted), (2003).

15. Q. Pei and O. Inganäs, "Electrochemical applications of the bending beam method; a novel way to study ion transport in electroactive polymers", *Sol. State Ion.* 60, 161-166 (1993).

16. E. Smela, "Microfabrication of PPy microactuators and other conjugated polymer devices", *J. Micromech. Microeng.* 9, 1-18 (1999).

17. L. Bay, S. Skaarup, K. West, T. Mazur, O. Joergensen, and H. D. Rasmussen, "Properties of polypyrrole doped with alkylbenzene sulfonates", Proc. SPIE's 8th Int. Symp. Smart Struc. Mater., Electroactive Polymer Actuators and Devices (EAPAD), Newport Beach, CA, 5-8 March 2001 Vol. 4329, p. 101-105.

18. H. D. Espinosa and B. C. Prorok, "Size Effects on the Mechanical Behavior of Thin Gold Films", Symposium on Mechanical Properties of MEMS Structures, the ASME 2001 International Mechanical Engineering Congress and Exposition, New York, 2001.

Appendix B

The attached conference paper "Polypyrrole/gold bilayer characterization" was presented by S. Fanning at the SPIE 12th Annual International. Symposium on Smart Structures and Materials, EAPAD, in San Diego, CA, 6-10 March, 2005. It appears on pages 292 to 301 of volume 5759.

Polypyrrole/Gold Bilayer Characterization

Steven Fanning, Yingkai Liu, Marc Christophersen, Matthias Düerkop, and Elisabeth Smela
Mechanical Engineering Dept., University of Maryland, College Park, MD 20742

and

Benjamin Shapiro
Aerospace Engineering Dept., University of Maryland, College Park, MD 20742
* Author for correspondence. email: smela@eng.umd.edu, tel: +1 301-405-5265, fax: +1 301-314-9477

ABSTRACT

Polypyrrole/gold bilayer microactuators are being developed in our laboratory for biomedical applications such as microvalves. To fully open and close the valves, the bilayer hinges must be able to rotate between 0° and 180° within a few seconds against external forces. The layer thicknesses and hinge lengths must therefore be properly designed for the application. However, existing models fail to predict the correct behavior of microfabricated PPy/Au bilayer microactuators. Therefore, additional experimental data are needed to correctly forecast their performance. Bilayer actuators were fabricated with ranges of PPy thicknesses and hinge lengths. Bending angles were recorded through a stereomicroscope in the fully oxidized and reduced states. Isometric forces exerted by the hinges were measured with a force transducer, the output of which was read by a potentiostat and correlated with the applied potentials.

Keywords: polypyrrole, bilayer, bending angle, force, modeling

1 INTRODUCTION

Bilayer microactuators are being developed in our laboratory for several applications [1]. For example, polypyrrole/gold (PPy/Au) bilayers are being developed to open and close microvalves that control the flow of biological fluids (Figure 1). Polypyrrole actuators are ideal for this application because they operate in liquids, require only small operating voltages, and produce large bending. Biolabs-on-a-chip are another application [2]. In these devices, PPy/Au actuators are used to confine cells over sensors inside microvials.

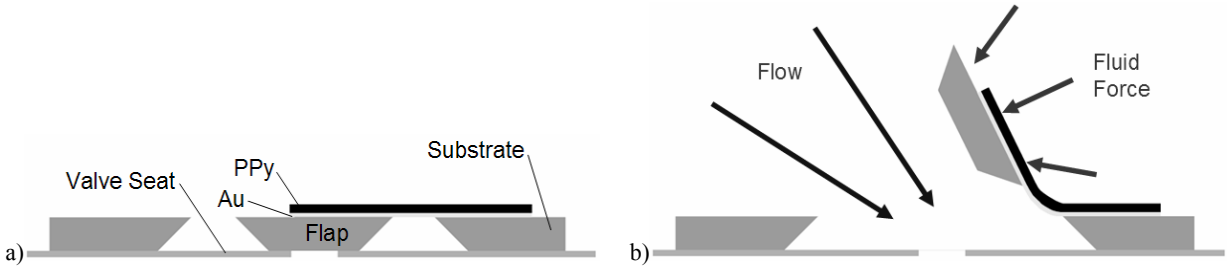

Figure 1. Schematic drawing of microvalve in both a) closed and b) open states.

To design such microactuators, relationships are needed between hinge parameters (length, PPy thickness, and PPy to Au thickness ratio) and performance (bilayer curvature and output force). Models have been created [3], but they do not accurately account for the behavior of the microactuators for a number of reasons, including 1) there is a strain gradient in the PPy arising from the electrodeposition process [4]; 2) during actuation, the Young's modulus of the polymer

varies [5]; 3) the modulus of PPy has only been measured for thicker films [5] and may be thickness dependent; 4) the morphology [6] and strain [7] of the PPy change with thickness; and 5) the properties of the PPy are affected by the microfabrication process steps, which include exposure to solvents, bases, vacuum, and elevated temperatures. This leads to a need for experimental characterization of the microfabricated bilayers. Based on the experimentally determined curvatures and forces, a model can then be developed that includes those of the effects that are found to influence the behavior.

Simple initial models based on standard bilayers provide a starting point from which to begin characterization. The radius of curvature can be estimated by the Timoshenko equation [8]:

$$\frac{1}{R} = \kappa = \left(\frac{\alpha_{PPy} - \alpha_{Au}}{h_{Au}} \right) \frac{6mn(1+m)}{1+4mn+6m^2n+4m^3n+m^4n^2} \quad (1)$$

where κ is the curvature (the inverse of the radius of curvature R), h is the thickness of the layer, E is the Young's modulus of the material, and α is the inplane actuation strain of the material. The variables m and n are the ratios:

$$m = \frac{h_{PPy}}{h_{Au}} \text{ and } n = \frac{E_{PPy}}{E_{Au}}$$

The Young's modulus of PPy doped with dodecylbenzenesulfonate, PPy(DBS), which we use in our work, has been reported to be 0.45 GPa in the oxidized state and 0.20 GPa in the reduced state for films 10 μm thick [5]. (Note that since differential adhesion was used to fabricate these samples, they are real bilayers: there is no Cr adhesion layer to consider.) The Young's modulus for thin gold films has been shown to be 53-55 GPa [9]. The strain in PPy(DBS) has been reported to be approximately 3% in the plane of the film, α_{PPy}=0.03, and the gold does not change volume, α_{Au}=0. Using these values, equation (1) predicts that the curvature of the bilayer is a maximum at a PPy:Au thickness ratio of approximately 3.5:1 (Figure 2). Since PPy(DBS) contracts in the oxidized state, and the bilayer bends up from the substrate, we assumed that the Young's modulus value for the oxidized state would be more appropriate to use in an initial estimate. Figure 2a shows how the curvature and peak position change if the value used for the modulus of gold is varied (83 GPa is the value for bulk material), Figure 2b what happens if the modulus of PPy is varied, and Figure 2c what happens if the strain is varied. In all these extreme cases, the PPy:Au thickness ratio giving the greatest curvature is between 2:1 and 6:1.

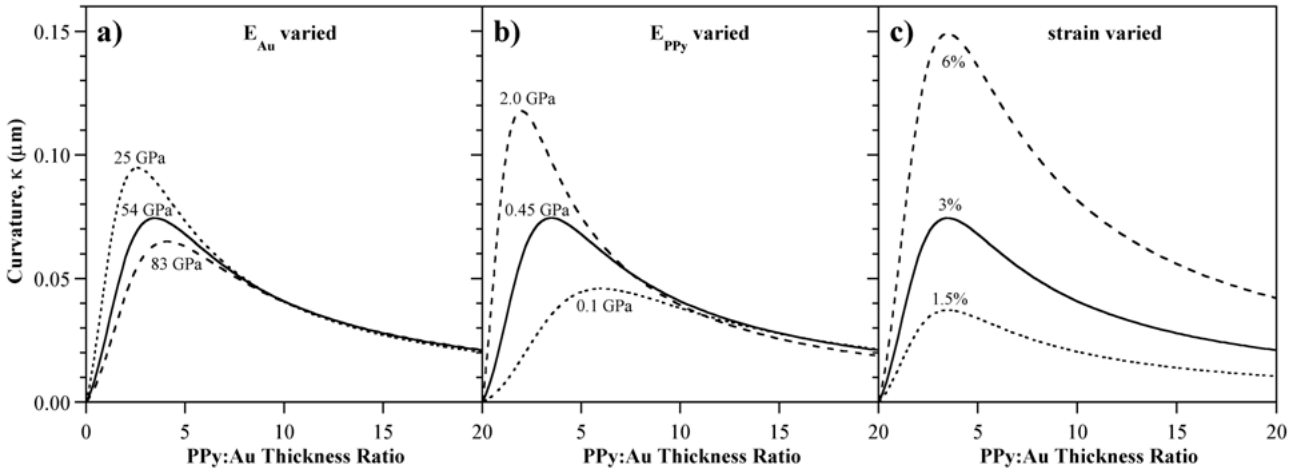

Figure 2. Graphs of curvature as a function of thickness ratio predicted by equation (1) showing (solid lines) a peak at a thickness ratio of 3.5:1 for values of E_{Au} = 54 GPa, E_{PPy} = 0.45 GPa, and α_{PPy} = 0.03. The graphs also show how the peak height and position depend on these parameters.

The moment per unit width of a beam, M, is the force exerted by the beam times the length of the beam. The moment is given by:

$$M = \frac{E_{Au} h_{Au}^{2} m(1+m) n(\alpha_{PPy} - \alpha_{Au})}{(2+2mn)} \quad (2)$$

Since M = F*L and the moment does not depend on beam length, the force decreases as the beam gets longer. The moment exerted by the bilayer increases with increasing PPy thickness. There is no peak: more is simply better.

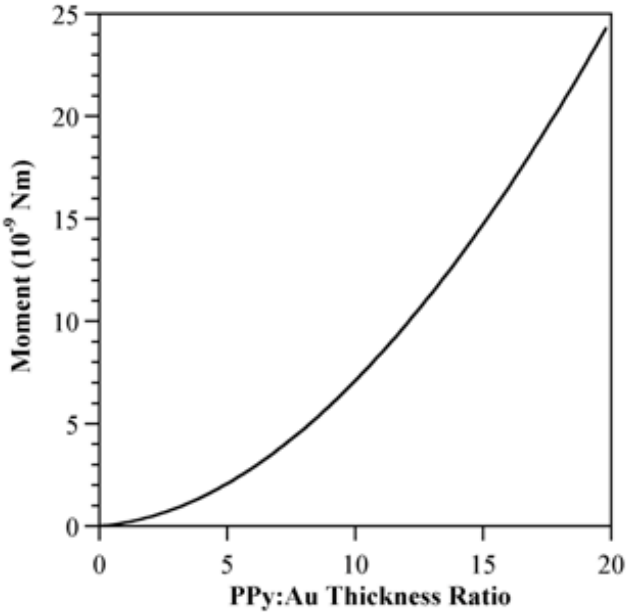

Figure 3. Moment per unit width as a function of thickness ratio as predicted by equation (2) for values of E_{Au} = 54 GPa, E_{PPy} = 0.45 GPa, and α_{PPy} = 0.03.

To design an actuator for a given application, certain requirements must first be established: the actuation force required to act against external forces on the moving part, the desired radius of curvature, the bending angle, and the speed. The maximum PPy thickness is limited by the required speed. The gold thickness would be selected to give the PPy:Au thickness ratio that yields the required radius of curvature, but this must take into consideration that there is a minimum gold thickness of 1000 Å, which is required for structural stability [10]. The hinge length is chosen to satisfy the required bending angle. The hinge width is adjusted to give the required force (since PPy thickness and hinge length are already constrained).

2 EXPERIMENTAL

2.1 Bilayer Fabrication

In microfabrication, there are two basic approaches that can be taken to create structures [11]. The first is bulk micromachining, in which the substrate itself is etched, and the second is surface micromachining, in which the moving structures are created on top of a passive substrate. In the bulk micromachining approach, which is used for the microvalves since the fluid goes through the substrate, the flap is created from the substrate using wet chemical etching or reactive ion etching [10]. In surface micromachining, which is required for the cell clinics because the substrate is covered in circuitry [12], the flap is formed from a thin film, such as a photopatternable polymer. This approach has a less complex fabrication sequence and exposes the PPy to milder processing conditions, so it was used in the present

study to characterize the bilayers. Our microvalves are created on three types of substrates: Kapton (DuPont), titanium, and silicon. The three substrates require quite different fabrication sequences. In future studies, the effect of fabrication method will be examined, but qualitative results have already been obtained. Kapton is etched using reactive ion etching in an oxygen plasma with either a thermally evaporated or sputtered aluminum etch mask, with the flaps released from the back side. The long etch time for Kapton, which takes place at elevated temperatures, has been found to reduce bending angles. Titanium substrates are etched in hydrofluoric acid. An as-yet-unidentified step in this process sequence has proven to have an adverse effect on the functionality of the bilayers. Silicon substrates are etched through the back using deep reactive ion etching (DRIE). These samples had the most bilayer movement.

The surface micromachining process sequence used to produce the actuators in this paper followed one that has been previously published [4, 13]. There were two differences: SU-8 was chosen as the rigid plate material, as opposed to BCB, and photoresist was removed in ethanol after the RIE etch step, rather than through further RIE etching. Flaps lifted slightly from the surface after ethanol soaking, signifying release. Full bending occurred upon immersion in the electrolyte.

The Au thickness was 1000 Å, and the PPy was deposited potentiostatically at 0.48 V vs. Ag/AgCl from a 0.1 M aqueous solution of NaDBS and pyrrole. These first-generation samples did not include an electroplated gold layer to promote adhesion between the gold and the PPy [14, 15] because we did not yet know how to account for such a layer in our mechanical model. They did, however, include a range of hinge lengths from 4 μm to 200 μm, and the PPy was deposited to different thicknesses to obtain thickness ratios from 3:1 to 19:1.

2.2 Bilayer Actuation

The sample was held flush against the bottom of the cell with a gold-plated screw and nut pressing down on one of the contact pads. Each contact pad ran to one series of actuators, and there were multiple series on each sample. A graphite counter electrode (VWR) was placed near the sample, and a Ag/AgCl reference electrode was placed between the working and counter electrodes. A potentiostat (EcoChemie pgstat30) electrochemically cycled the sample in a 0.1 M NaDBS solution.

2.3 Bending Angle: Setup & Methods

Bending angles were recorded through a Leica Z16 APO stereomicroscope with a 187 mm working distance, viewing the samples either from directly overhead or from an angle. Several bending samples could be measured simultaneously this way. The bending angle of each flap was determined from photographs taken with the potentials held at the redox limits of 0 and -1 V vs. Ag/AgCl.

The overhead viewing method (Figure 4) was used for the majority of the measurements. Photographs were taken of the flaps in the fully oxidized and reduced states and later analyzed. The apparent lengths of the hinge and flap when viewed from above were measured and compared with the original, unbent length, and geometrical relationships were used to determine the amount of bending.

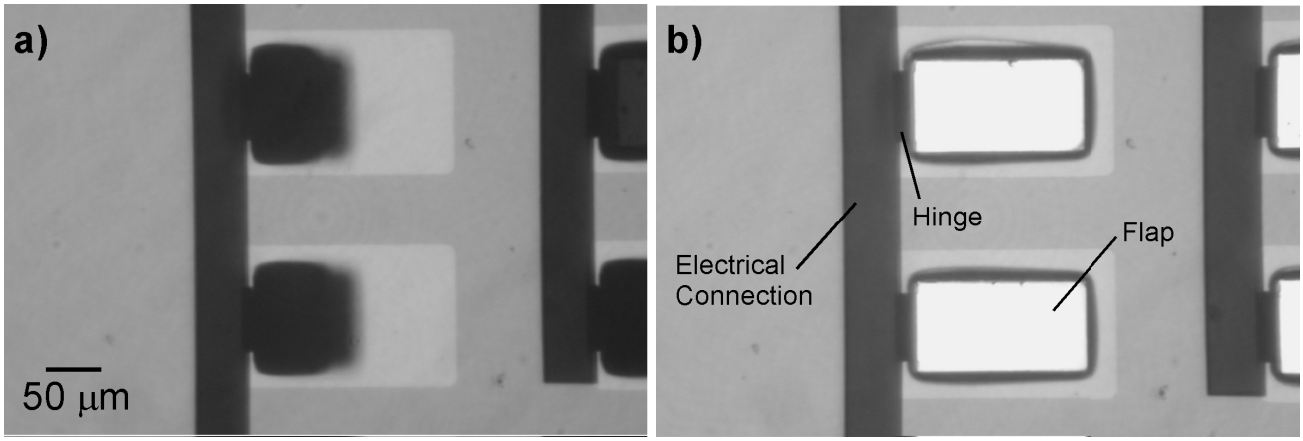

Figure 4. a) Actuated and b) flat samples with a PPy:Au ratio of 9:1 and a hinge length of 10 μm operated in a 0.1 M NaDBS electrolyte solution.

As a check on the results obtained from the overhead views, and to examine the shape of the bilayer, the actuators were imaged from a shallow angle (Figure 5). Snell's law was used to correct the images based on the fact that the light path was bent at the air/electrolyte interface. The index of refraction of the 0.1 M NaDBS solution was measured to be 1.337 at 20 °C using an Abbe refractometer (American Optical Corp., Model 10450).

Imaging samples at an angle worked well for the relatively large bulk micromachined valves (Figure 6a), but was more challenging for the smaller microvial lids. For the latter, the images were too blurry to see the edges of the hinges (Figure 6b). Four issues that degraded the quality of images taken at an angle at high magnification were shallow depth of focus, poor lighting, vibrations, and cloudiness. The depth of focus was increased by closing the aperture, but this cut down on the available light. Lighting was substantially improved by adding a reflector at the back of the sample to scatter more light onto it (Figure 5b). Vibrations also increasingly disturbed the image quality with higher magnification, even though the measurements were performed on an optical table. Finally, images through water are always more blurry than through air, and the light path in the water was much longer for the oblique views than for the overhead views. The solution to these imaging problems was the addition of large rigid pads on the ends of the bilayers, allowing the bending angle to be much more easily determined (see Figure 6c, which has enough depth of focus to image one hinge).

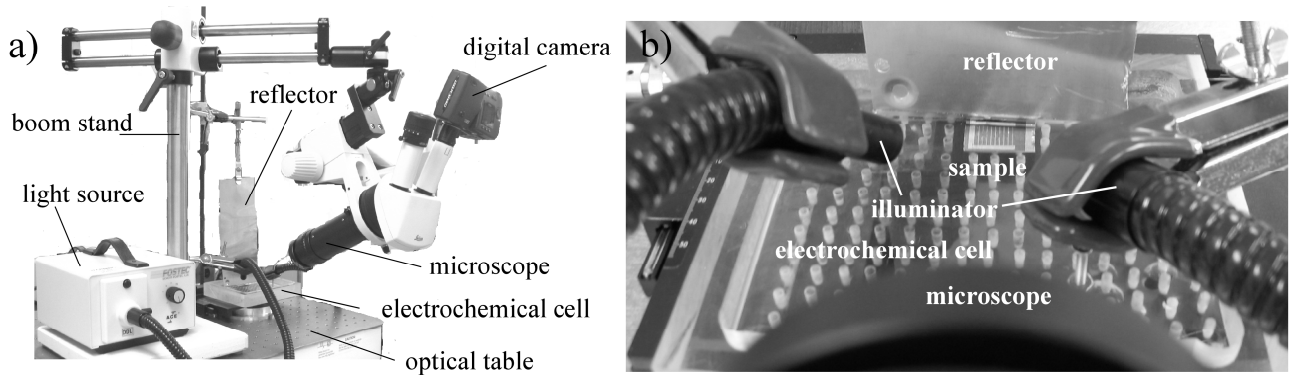

Figure 5. a) Overall view of the setup used for bending angle oblique view measurements and b) a closer view from the perspective of the microscope.

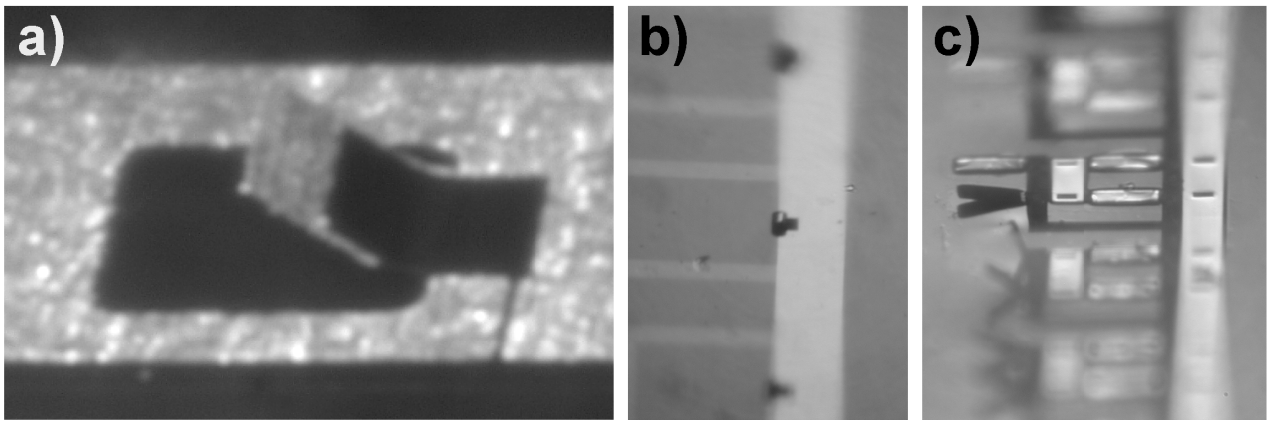

Figure 6. Side angle view of a) a bulk micromachined Ti microvalve actuator with a flap 325 x 325 μm^2 and a hinge length of 90 μm and b) a surface micromachined, microvial-size bilayer without a lid and with a width of 50 μm and a length of 100 μm, and c) a bilayer 40 μm wide and 10 μm long with a lid 60 μm wide and 150 μm long.

2.4 Force: Setup & Methods

Isometric forces exerted by the hinges were measured with a force transducer (Aurora Scientific 406A, maximum force 0.5 mN, sensitivity 0.01 μN). This force transducer interfaces to the outside world through a glass tube 1 mm in diameter that protrudes from the head (rectangular box in Figure 7). A tungsten wire approximately 15 mm in length and 180 μm in diameter was sharpened electrochemically and then affixed into the tube using paraffin wax. This needle allowed accurate placement on the tiny flaps, and the rigid pads allowed accurate and consistent placement of the force transducer needle a known distance from the end of the bilayer. With the aid of a microscope, the transducer head was lowered to place the needle onto the center of a closed flap (bent 180°) until the force transducer registered an increase in signal; then it was raised slightly to be just above the flap. The sample, upon reduction, moved until the back side of the flap made contact with the needle, which did not allow further motion (isometric measurement). The output of the force transducer was input to the potentiostat, and thereby the force data correlated with the potential and current.

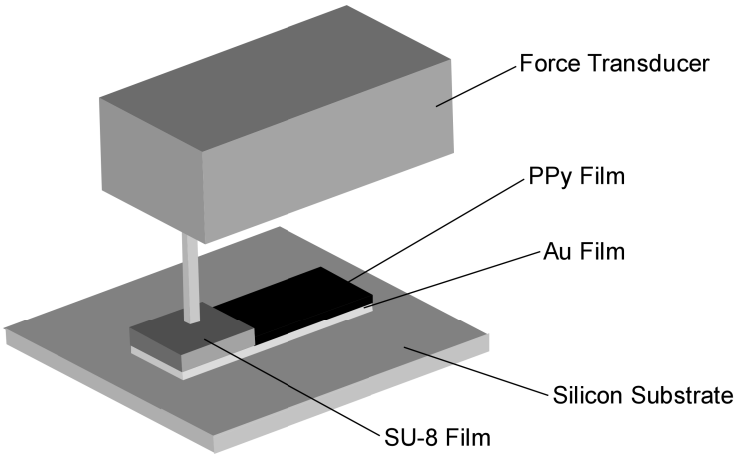

Figure 7. Schematic diagram of the force transducer needle in contact with a flap for hinge force measurement. This diagram shows a flap measured from the front side. The force measurements in this paper, however, were made on the back side of closed flaps attempting to open.

3 RESULTS AND DISCUSSION

3.1 Bending Angle

As a reality check, bending angles were recorded for different hinge lengths. As they should, the bending angles increased linearly with hinge length L up to 180° (Figure 8), after which the flaps touched the substrate and no further bending was possible. The radius of curvature was calculated from the slope of this curve ($L/2\pi$ * bending angle in radians), and for this sample it was 9 μm. The ability of the hinges to bend 180° with a hinge length of just 20 μm is consistent with previously fabricated surface micromachined samples [13].

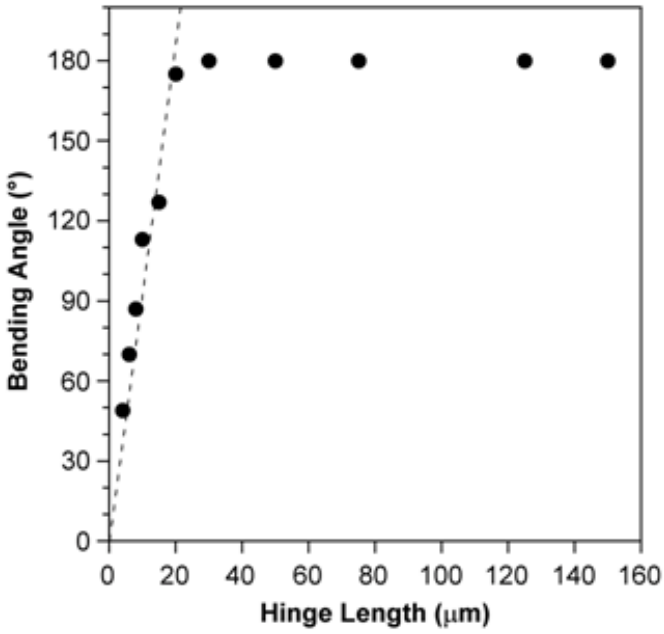

Figure 8. Bending angle as a function of hinge length for a thickness ratio of 5:1 (5200 Å of PPy and 1000 Å of Au) cycled in 0.1 M NaDBS. The behavior was linear until the hinges became so long that they bent 180° and the lids touched the substrate.

3.2 Force

Figure 9 shows a plot of the force from a single bilayer actuator vs. time; the current is superimposed. The time delay between the current and force responses is the time that the lid traveled before making contact with the transducer needle.

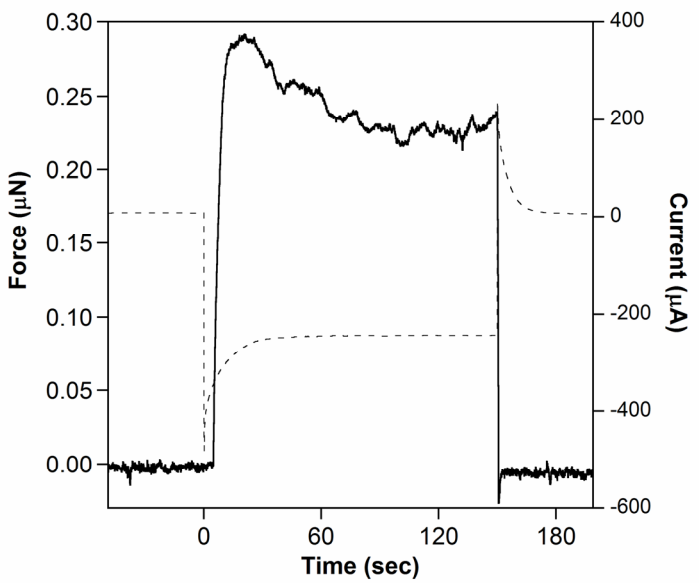

Figure 9. Plot of force and current vs. time. A voltage of –1 V vs. Ag/AgCl was applied at t=0, and the lid hit the needle at 5 seconds. This plot is for a hinge length of 75 μm and a thickness ratio of 5:1.

Bilayer output force is expected to decrease linearly with increasing hinge length (equation (2)). In Figure 10 the normalized force is plotted for different hinge lengths on samples with two different thickness ratios. Since hinges with different lengths had different widths, the force was normalized to the value it would have had for a width of 60 μm. Clearly, the error bars are too large to come to any conclusions about whether the expected relationship is obeyed.

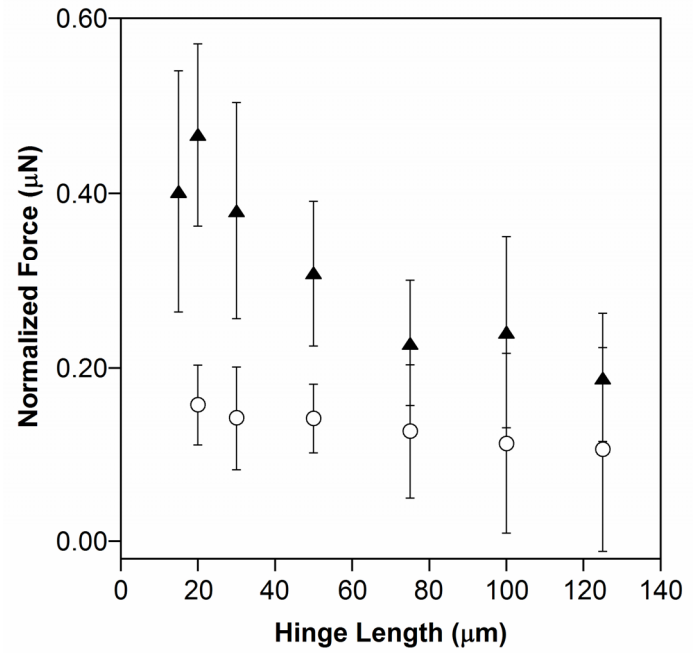

Figure 10. Actuator output force as a function of hinge length for two different PPy:Au thickness ratios. Data correspond to samples with 10:1 (triangles) and 5:1 (circles) thickness ratios.

The force transducer designed to measure forces on the μN scale, is very sensitive to vibrations and environmental factors. The largest environmental factors were temperature and humidity changes resulting from lighting sources and

movement of individuals near the device. Vibrations were detected even when the experiments were performed on an optical table. To reduce the noise, the measurements in Figure 10 were taken at night, which helped significantly. However, the noise is still too high. In future samples, hinge width may be increased, while holding the hinge length the same, to increase the overall force. The influence of force transducer needle placement will need further investigation, as well, because this has a sizable impact on the reproducibility of the force measurements.

4 CONCLUSIONS

Initial characterization of PPy bilayers has taken place on surface micromachined bilayers. Challenges in measurement of bending angle and force have been identified and will be addressed in future work. To make a more accurate model, the known non-linearities will also be investigated.

5 ACKNOWLEDGEMENTS

We would like to acknowledge the funding provided by MIPS (Maryland Industrial Partnerships) and NIH (National Institute of Health) through IBT (Infinite Biomedical Technologies). We would also like to thank Tom Loughran, Nolan Ballew and Dr. Y Martin Lo.

REFERENCES

[1] E. Smela, "Conjugated polymer actuators for biomedical applications," *Adv. Mat.*, vol. 15 (6), pp. 481-494, 2003.

[2] M. Urdaneta, Y. Liu, P. Abshire, and E. Smela, "Integrating conjugated polymer microactuators with CMOS sensing circuitry for studying living cells," Proc. SPIE's 12th Annual Int'l. Symposium on Smart Structures and Materials, EAPAD, San Diego, California, USA, March 6-10 2005.

[3] M. Benslimane, P. Gravesen, K. West, S. Skaarup, and P. S. Larsen, "Performance of polymer based actuators: the three-layer model," Proc. SPIE-Int. Soc. Opt. Eng.: Smart Structures and Materials, vol. 3669, Newport Beach, CA, 1-5 March 1999, pp. 87-97.

[4] E. Smela, M. Kallenbach, and J. Holdenried, "Electrochemically driven polypyrrole bilayers for moving and positioning bulk micromachined silicon plates," *JMEMS*, vol. 8 (4), pp. 373-383, 1999.

[5] L. Bay, N. Mogensen, S. Skaarup, P. Sommer-Larsen, M. Jorgensen, and K. West, "Polypyrrole doped with alkyl benzenesulfonates," *Macromol.*, vol. 35 (25), pp. 9345-9351, 2002.

[6] K. Naoi, Y. Oura, M. Maeda, and S. Nakamura, "Electrochemistry of surfactant-doped polypyrrole film(I) -- formation of columnar structure by electropolymerization," *J. Electrochem. Soc.*, vol. 142 (2), pp. 417, 1995.

[7] J. C. Hooker, I. Johanssen, and E. Smela, "Monitoring volume expansion in PPy(DBS) with AFM: effects of DBS isomers," Risø National Laboratory, Condensed Matter Physics and Chemistry, Roskilde, Denmark, Annual Report 1 Jan - 31 Dec 1999.

[8] S. Timoshenko, "Analysis of bi-metal thermostats," *J. Opt. Soc. Am.*, vol. 11 pp. 233-256, 1925.

[9] H. D. Espinosa and B. C. Prorok, "Size effects on the mechanical behavior of gold thin films," Proc. ASME 2001 International Mechanical Engineering Congress and Exposition, New York, NY, November 11-16 2001.

[10] E. Smela, "Microfabrication of PPy microactuators and other conjugated polymer devices," *J. Micromech. Microeng.* vol. 9 (1), pp. 1, 1999.

[11] G. T. A. Kovacs, *Micromachined Transducers Sourcebook*. Boston: WCB McGraw-Hill, 1998.

[12] Y. Liu, L. Oh, S. Fanning, B. Shapiro, and E. Smela, "Fabrication of folding microstructures actuated by polypyrrole/gold bilayer," Proc. Transducers '03: The 12th International Conference on Solid State Sensors, Actuators and Microsystems, vol. 1, Boston, MA, USA, June 8-12 2003, pp. 786-789.

[13] E. Smela, O. Inganäs, and I. Lundström, "Controlled folding of micrometer-size structures," *Science*, vol. 268 (5218), pp. 1735-1738, 1995.

[14] M. Pyo, C. C. Bohn, E. Smela, J. R. Reynolds, and A. B. Brennan, "Direct strain measurement of polypyrrole actuators controlled by the polymer/gold interface," *Chem. Mater.*, vol. 15 (4), pp. 916-922, 2003.

[15] Y. Liu, Q. Gan, S. Baig, and E. Smela, "Improving adhesion of polypyrrole to Au for long-term actuation," Proc. SPIE's 12th Annual Int'l. Symposium on Smart Structures and Materials, EAPAD, San Diego, CA, March 7-10 2005.

References

1. "Leaky Faucet?," The Medical Reporter (2005) http://medicalreporter.health.org/tmr0199/urinaryincontinence.html.

2. T. Wagner, "Economic costs of urinary incontinence in 1995," Urology, 51**,** 355-361 (1998).

3. L. H. Oh, "Development of micro-valves actuated by polypyrrole/gold bilayers," Mechanical Engineering, University of Maryland, College Park, MD (2003).

4. E.-L. Kupila and J. Kankare, "Electropolymerization of pyrrole: effects of pH and anions on the conductivity and growth kinetics of polypyrrole," Synth. Met., 55-57 (2-3)**,** 1402-1405 (1993).

5. M. R. Gandhi, P. Murray, G. M. Spinks, and G. G. Wallace, "Mechanism of electromechanical actuation in polypyrrole," Synth. Met., 73 (3)**,** 247-256 (1995).

6. Q. Pei and O. Inganäs, "Electrochemical applications of the bending beam method. 2. Electroshrinking and slow relaxation in polypyrrole," J. Phys. Chem., 97**,** 6034-6041 (1993).

7. J. S. Go and S. Shoji, "A disposable, dead volume-free and leak-free in-plane PDMS microvalve," Sens. Act. A, A114 (2-3)**,** 438-444 (2004).

8. N.-T. Nguyen, T.-Q. Truong, K.-K. Wong, S.-S. Ho, and C. L.-N. Low, "Micro check valves for integration into polymeric microfluidic devices," Journal of Micromechanics and Microengineering, 14 (1)**,** 69-75 (2004).

9. D. J. Beebe, J. S. Moore, J. M. Bauer, Q. Yu, R. H. Liu, C. Devadoss, and B.-H. Jo, "Functional hydrogel structures for autonomous flow control inside microfluidic channels," Nature, 404 (April 6)**,** 588-590 (2000).

10. L. Bay, N. Mogensen, S. Skaarup, P. Sommer-Larsen, M. Jorgensen, and K. West, "Polypyrrole doped with alkyl benzenesulfonates," Macromolecules, 35 (25)**,** 9345-9351 (2002).

11. H. D. Espinosa and B. C. Prorok, "Size effects on the mechanical behavior of gold thin films," ASME 2001 International Mechanical Engineering Congress and Exposition, New York, NY (November 11-16, 2001).

12. T. F. Otero and J. M. Sansinena, "Artificial muscles: influence of electrolyte concentration on bilayer movement," Third ICIM/ESSSM, Lyon, France, (SPIE), vol. 2779, p. 365-370 (3-5 June, 1996).

13. E. Smela, O. Ingansis, and I. Lundstrom, "Controlled folding of micrometer-size structures," Science, 268 (5218)**,** 1735-1738 (1995).

14. J. D. Madden, S. R. Lafontaine, and I. W. Hunter, "Fabrication by electrodeposition: building 3D structures and polymer actuators," MHS'95. Proceedings of the Sixth International Symposium on Micro Machine and Human Science, Nagoya, Japan, (IEEE), p. 77-81 (1995).

15. E. Smela, O. Inganäs, and I. Lundström, "Differential adhesion method for microstructure release; an alternative to the sacrificial layer," Transducers '95/Eurosensors IX, Stockholm, Sweden, vol. 1, p. 218-219 (1995).

16. E. W. H. Jager, E. Smela, and O. Inganäs, "Microfabricating conjugated polymer actuators," Science, 290**,** 1540-1545 (2000).

17. K. R. Williams and R. S. Miller, "Etch rates for micromachining processing," J. Microelectromech. Syst., 5**,** 256-269 (1996).

18. C. O'Mahony, M. Hill, P. J. Hughes, and W. A. Lane, "Titanium as a micromechanical material," J. Micromech. Microeng., 12**,** 438–443 (2002).

19. T. N. Pomsin-Sirirak, Y. C. Tai, H. Nassef, and C. M. Ho, "Titanium-alloy MEMS wing technology for a micro aerial vehicle application," Sens. Act. A, 89 (1-2)**,** 95-103 (2001).

20. P.-F. Chauvy, C. Madore, and D. Landolt, "Electrochemical micromachining of titanium through a patterned oxide film," Electrochem. Sol. State Lett., 2 (3)**,** 123-125 (1999).

21. M. F. Aimi, M. P. Rao, N. C. Macdonald, A. S. Zuruzi, and D. P. Bothman, "High-aspect-ratio bulk micromachining of titanium," Nature Materials, 3**,** 103-106 (2004).

22. E. Smela, M. Kallenbach, and J. Holdenried, "Electrochemically driven polypyrrole bilayers for moving and positioning bulk micromachined silicon plates," J. Microelectromech. Syst., 8 (4)**,** 373-383 (1999).

23. P. Arquint, "Integrated blood gas sensor for pO_2, pCO_2 and pH based on silicon technology," PhD Thesis Thesis, Institute of Microtechnology, Faculty of Sciences, University of Neuchatel, Neuchatel (1994).

24. S. Shimoda and E. Smela, "The effect of pH on polymerization and volume change in PPy(DBS)," Electrochim. Acta, 44 (2-3), 219-238 (1998).

25. S. Timoshenko, "Analysis of bi-metal thermostats," J. Opt. Soc. Am., 11, 233-256 (1925).

26. H. D. Espinosa and B. C. Prorok, "Size effects on the mechanical behavior of gold thin films," Journal of Materials Science, 38 (20), 4125-4128 (2003).

27. K. Gieck and R. Gieck, Engineering Formulas, (McGraw-Hill, Inc., Germering, Germany, 1997) Z11.

28. "Overview - Silicone Elastomer, for Thermal Management," MatWeb: Material Property Data (2005) http://www.matweb.com/search/SpecificMaterial.asp?bassnum=O5245.

29. "Micropol Isoplas P501 Crosslinkable Polyethylene," MatWeb: Material Property Data (2005) http://www.matweb.com/search/SpecificMaterial.asp?bassnum=PMICRO23.

30. "Kapton: Summary of Properties," DuPont (2005) http://www.dupont.com/kapton/general/H-38492-2.pdf.

31. H. Okuzaki and K. Funasaka, "Electromechanical properties of a humido-sensitive conducting polymer film," Macromol., 33 (22), 8307 -8311 (2000).

32. E. Smela, "Microfabrication of PPy microactuators and other conjugated polymer devices," J. Micromech. Microeng., 9, 1-18 (1999).

33. "Human Urine," (2005) http://www.4qc.com/products/urinalysis/dipper.html.

34. D. B. Hibbert and A. M. James, Dictionary of Electrochemistry, (Macmillan Press, London, England, 1984)

35. W. Takashima, S. Pandey, and K. Kaneto, "Cyclic voltammetric and electromechanical characteristics of freestanding polypyrrole films in diluted media," Thin Solid Films, 438-439, 339-345 (2003).

36. S. Maw and E. Smela, "Effects of monomer and electrolyte concentrations on actuation of PPy(DBS) bilayers," (in preparation) (2004).

37. J. P. Ibe, P. P. Bey, Jr., S. L. Brandow, R. A. Brizzolara, N. A. Burnham, D. P. DiLella, K. P. Lee, C. R. K. Marrian, and R. J. Colton, "On the electrochemical etching of tips for scanning tunneling microscopy," J. Vac. Sci. Technol. A, Boston, MA, vol. 8, p. 3570-3575 (1990).